2011

Hydrodynamic Characterization of 3D Fluidized Beds Using Noninvasive Techniques

Joshua Drake
Iowa State University

Hydrodynamic characterization of 3D fluidized beds using noninvasive techniques

by

Joshua Bryon Drake

A dissertation submitted to the graduate faculty

in partial fulfillment of the requirements for the degree of

DOCTOR OF PHILOSOPHY

Major: Mechanical Engineering

Program of Study Committee:

Theodore J. Heindel, Major Professor

Hui Hu

Ron M. Nelson

Michael G. Olsen

Shankar Subramaniam

Iowa State University

Ames, Iowa

2011

TABLE OF CONTENTS

LIST OF FIGURES

LIST OF TABLES

NOMENCLATURE

Conceptual Notation

2D	two-dimensional
3D	three-dimensional
BASF	Badische Anilin und Soda-Fabrik
CARPT	computer automated radioactive particle tracking
CCD	charged coupled device
CFD	computational fluid dynamics
CFB	circulating fluidized bed
CNDE	center for nondestructive evaluation
CO	carbon monoxide
COR	center of rotation
CsI	cesium iodide
CT	computed tomography
DAQ	data acquisition
DSB	double strength billet
FCC	fluid catalytic cracking
FFB	fixed fluidized bed
F-T	Fischer-Tropsch
H_2	hydrogen molecule
ID	internal diameter
LDV	laser Doppler velocimetry

LIPA	laser induced photochemical anemometry
MITI	Ministry of International Trade and Industry
NCC	normalized cross-correlation
NPT	national pipe thread
OD	outer diameter
OOI	object of interest
PIV	particle image velocimetry
PSD	particle size distribution
PTV	particle tracking velocimetry
RMS	root mean square
ROI	region of interest
UNF	unified fine
XFloVis	X-ray flow visualization
XRIP	X-ray image processor

English Formulaic Notation

C	normalized cross-correlation coefficient
C_{max}	maximum normalized cross-correlation coefficient
D_c	reactor diameter
$d_{particle}$	particle diameter
d_{sv}	surface to volume particle diameter
f_d	Doppler shift frequency
g	gravitational constant

H_0	static bed height
H_g	operating bed height
I	transmitted X-ray intensity
I_{ave}	averaged light and dark calibration image
I_b	bulk XCT intensity
I_{dark}	dark calibration image
I_g	gas XCT intensity
I_{image}	uncalibrated image
I_{light}	light calibration image
I_{new}	new calibrated image
I_p	particle XCT intensity
I_o	incident X-ray intensity
J	phase coupling factor
m_{bed}	bed mass
Q_{mf}	minimum fluidization air flow rate
$Q_{mf,0}$	minimum fluidization air flow rate without side-air injection
Q_s	side-air injection flow rate
T	object thickness
U	superficial velocity
U_g	superficial gas velocity
U_l	superficial liquid velocity
U_{mf}	minimum fluidization velocity
$U_{mf,0}$	minimum fluidization velocity without side-air injection

U_{mb}	minimum bubbling velocity
U_{trans}	transition velocity
v	velocity
v_g	gas velocity
v_l	liquid velocity
V_{bed}	bed volume
XCT	X-ray computed tomography
XPTV	X-ray particle tracking velocimetry

Greek Formulaic Notation

ε	volumetric mass fraction
ε_g	volumetric gas mass fraction
$\varepsilon_{g,b}$	volumetric bulk bed mass fraction
$\varepsilon_{g,r}$	annular volumetric gas mass fraction
ε_l	volumetric liquid mass fraction
λ	wavelength
μ	X-ray attenuation coefficient
μ_b	bulk bed X-ray attenuation coefficient
μ_g	gas X-ray attenuation coefficient
μ_p	particle X-ray attenuation coefficient
ρ	density
ρ_b	bulk density
ρ_p	particle density

ρ_g	gas density
ρ_l	liquid density
θ	incident angle

ABSTRACT

Fluidized beds are useful processing systems that are employed by many industries for their relatively unique operating properties. Low pressure drops, uniform temperature distributions, and high heat/mass transfer rates occur through the action of vertical gas injection into a column of solid particles. Although these properties give fluidized beds great advantages over other processing systems, the hydrodynamic characterization of fluidized beds is important for the efficient processing of many consumer products. However, fluidized bed hydrodynamics are difficult to visualize and quantify because most fluidized beds are opaque. Traditionally, the monitoring of local fluidized bed hydrodynamics has been done with intrusive probes that disturb local structure and the collection of data over large areas is time consuming. X-ray computed tomography (CT), as a noninvasive technique, can quantify local time-average phase fractions in highly dynamic multiphase systems without disturbing local structure.

Using X-ray visualization techniques, methods have been developed in this study to: 1) test the repeatability of calculating local time-average gas holdup values using X-ray CTs; 2) find the fluidization uniformity of a non-reactive cold-flow fluidized bed; 3) compare local time-average gas holdup values in various bed materials, diameters, and operating conditions; and 4) compare annular hydrodynamic structures within the beds. Tests for the first two objectives were completed using a 15.2 cm ID reactor, while varying between two bed materials (crushed walnut shell and glass beads) of the same size and two gas flow rates. The third objective used a 10.2 cm and 15.2 cm ID reactor, varied between three bed materials (ground corncob, crushed walnut shell, and glass beads) of the same size, and over four and five relative superficial gas velocities and side-air injection gas flow rates

respectively. The fourth objectives mirrored the third, however, did not use side-air injection.

Observations show that local time-average gas holdup values can be calculated through the use of multiple X-ray CTs. The method of calculation is shown to be highly repeatable over the various flow rates, bed materials used, and ambient environmental conditions. Axisymmetric fluidization uniformity of the bed is also confirmed using the same method, while some differences are observed with varying materials and flow rates. Uniformity is observed to increase with bed height and increased gas flow rates, due to increased dispersion of gas into the bed and mixing rates respectively. Local time-average gas holdup is observed to differ somewhat between reactors. However, the overall results show that the hydrodynamic structures, i.e. aeration jets, bubble coalescence zones, bubble rise zones, particle shearing zones, and the side-air injection plume, within the fluidized beds for each reactor are very similar. These structures coupled with axisymmetric fluidization uniformity indicate that gas flow and material circulation tend to be annular in shape. Moreover, changes in the shape, size, number, and location occur with changes in superficial gas velocity, bed diameter, and bed material density. It is also suspected that the aeration scheme of the bed and the bed material properties i.e. shape factor, coefficients of restitution, and porosity play a role in the development of these structures. The aeration jets are similar in length in all beds regardless of material density or bed diameter. They also tend to decrease in height and become increasingly wall leaning as superficial gas velocity increases. The coalescence of bubbles tends to occur in regular locations near the reactor wall just above the aeration jets within all beds regardless of material density, bed diameter, and gas flow rates. The rise paths of bubbles through all beds emanate from the coalescence zones

with relatively small widths and increasing in width as bed height increases. Particle shear zones occur in differing size, shape, number outside of all other hydrodynamic structures while migrating around the bed with changing material density, bed diameter, and superficial gas velocity. The diffusion of gas into the fluidized bed from the side-air injection plume in each bed is similar, due to advection dominance within the plume. Gas dispersion does not seem to occur by similar means between materials though, because crushed corncob and ground walnut shell are natural systems and have a higher porosity and lower density than glass beads. The natural materials also have non-uniform shape factors causing behavior differences with the fluidization gas. The time-average bed height between bed diameters is different for each material density and gas flow rate, where the height in the 10.2 cm diameter reactor is observed to be greater on average in all tests than in the 15.2 cm reactor, due to wall effects. Lastly, the techniques used for analysis in this study are valuable to computational fluid dynamicists for direct comparison to simulation and models of fluidized beds.

CHAPTER 1 INTRODUCTION

Equation Chapter 1 Section 1

1.1 Motivation

Fluidized beds are key components in the manufacture of various intermediate and end-user products (Dudukovic, Larachi et al. 1999), such as gaseous and liquid fuels, commodity chemicals, and pharmaceuticals (Zhu and Cheng 2006). In recent decades, fluidized beds have become the standard technology for small scale power generation (less than 25 MW) in Europe, North America, and China, among other countries (Oka 2004), where these plants either combust, pyrolyse, or gasify solids such as coal, biomass, and waste. Furthermore, concerns regarding global climate change due to increased carbon outputs from power generation, specifically the burning of fossil fuels, have become motivators in developed countries for changes in generation technology. This has increased the popularity of fluidized bed gasifiers to process biomass and coal into both transportation fuels and electrical generation (Cui and Grace 2007) due to their ability to greatly reduce the production of greenhouse gases and/or by-products. As developing nations increase their need for power generation and turn to more economical and efficient means to do so, fluidized bed reactors will most likely be the processor of choice. These facts pose a need to improve our knowledge of the basic science behind fluidized beds and are the primary motivator of this study.

Some of the most daunting problems facing fluidized bed reactors in terms of process efficiencies are: 1) the need for large gas throughputs requiring large reactor diameters and

heights; 2) the addition of heat exchange systems for highly exothermic processes; 3) the location of feedstock and recirculated material injection ports; and 4) the need for injection of gas horizontally through reactor walls. When reduced to their most basic form, all of these problems are hydrodynamically dependent and related to the bubbling of gas through the bed material and around submerged and fixed structures in the bed, the bed geometry, and properties of the fluidizing gas and bed material. The hydrodynamic characterization of a fluidized bed requires a deep understanding of these dependencies, particularly in the design process when mistakes can become extremely expensive. In fact, system failures have been reported in commercial reactors designed from laboratory or pilot scale models due to hydrodynamic changes over reactor scale-up (Squires, Kwauk et al. 1985; Krambeck, Avidan et al. 1987). Therefore, the main focus of this study is the understanding of fluidized bed hydrodynamics.

With the patent of the first fluidized bed gasifier in Germany in 1922 (Winkler 1922) the understanding of internal hydrodynamic bed structures has been slowly accumulating, yet is still somewhat lacking. This is largely due to the optical thickness of the reactor and bed material, limiting the methods for obtaining empirical data of bed hydrodynamics. Therefore, advances in scaling and efficiency improvements are challenging. Invasive probes such as anemometers have been used to monitor local bed hydrodynamics (Boerefijn, Poletto et al. 1999); however, these techniques are ill-suited because of their destructive nature to local bed hydrodynamics and bubbling behavior (Kaza 2008). Consequently, noninvasive techniques such as X-ray radiography/stereography in conjunction with particle tracking algorithms (Seeger, Kertzscher et al. 2003) and computed tomography imaging (Franka and Heindel 2009) have proven to be effective candidates for providing adequate

qualitative and quantitative data regarding internal bed hydrodynamics. Moreover, the data gleaned from these techniques is highly useful in the field of computational fluid dynamics (CFD) for model validation. Therefore, the final motivation of this study is to validate both the X-ray visualization techniques for acquiring useful hydrodynamic data from fluidized beds and empirical correlations used to model fluidized bed systems.

1.2 Objectives

The first objective of this study is to use X-ray CT imaging to obtain empirical data of time-average internal hydrodynamic structures in axisymmetric 3D fluidized beds. The second objective is to validate the calculation of local time-average gas holdup using X-ray CTs. The third objective is to show the fluidization uniformity of axisymmetric 3D fluidized beds without side-air injection using X-ray CTs. The forth objective is compare annular hydrodynamic structures within axisymmetric 3D fluidized beds and develop techniques to make direct comparisons of local time-average gas holdup data with 2D and 3D CFD models. To show how scaling affects internal bed hydrodynamic structures, a 3D axisymmetric 10.2 cm and 15.2 cm ID non-reactive cold-flow fluidized reactor will be used. Three different bed materials (crushed corncob, ground walnut shell, and glass beads) tested in each reactor will show how varying material density affects bed hydrodynamics. Software will be developed to analyze all aspects of this project. The following tasks outline how the objectives are reached:

1. Determine the minimum fluidization velocity of both reactors and three bed materials without side-air injection.

2. Determine and compare minimum fluidization velocities in each reactor for each bed material while varying the side-air injection flow rate.
3. Obtain X-ray CTs for each bed and material over a range of superficial gas velocities and side-air injection flow rates.
4. Quantify and compare the local time-average gas holdup from the X-ray CTs previously acquired using in-house developed software.

1.3 Outline

Chapter 2 presents a review of the literature describing multiphase flows, concepts of fluidization, bed materials, fluidized beds and the vessels that contain them, techniques of multiphase flow visualization, and multiphase flow modeling concepts and computational fluid dynamics. Chapter 3 provides an overview of the experimental setup and details of the experimental procedures. Chapters 4, 5, and 6 present papers that have been submitted for publication with selected journals and written by the author and Dr. Theodore Heindel. Although, these papers repeat much of what is discussed in chapters 2 and 3, they summarize the results of this study. The first focuses on the repeatability of the gas holdup calculation and uniformity of fluidization in axisymmetric 3D fluidized beds. The second presents comparisons of gas holdup in axisymmetric 3D fluidized beds of varying diameter, bed material density, and operating conditions. The third discusses the comparison of annular hydrodynamic structures within axisymmetric 3D fluidized beds. Lastly, chapter 7 details the overall conclusions of these studies and outlines recommendations for further study.

CHAPTER 2 LITERATURE REVIEW

Equation Chapter 2 Section 1

This chapter provides an overview of the main topics needed for a good understanding of the concepts and ideas employed in this research. An overview of multiphase flows is given in section 2.1. The hydrodynamics within a dynamic fluidized bed are described in section 2.2, emphasizing the major generalizations of fluidization: fluidization regimes, gas holdup, and minimum fluidization velocity. Section 2.3 explains the bed materials used in a fluidized bed reactor, focusing on the classification of the materials and their size distributions. Fluidized beds, the vessels that contain them and their uses are discussed in section 2.4. The different techniques employed in measuring the various properties of multiphase flows are summarized in section 2.5.

2.1 Multiphase Flows

A multiphase flow is defined as a system of materials each in a different chemical state (gas, liquid, or solid) that interact with one another (Crowe and Michaelides 2006). Each chemical state within the system occupies a volume fraction of space, the sum of which is unity. The system itself is defined by two different general phase groups (the particle and continuous phases) that are made up of the materials in different states. Bubbles (gas), drops (liquid), or particles (solid) within the system are defined as the particulate phase and the continuous phase (gas or liquid) is defined as the medium in which the particulate phase is contained (Loth, Tryggvason et al. 2006). A multiphase flow is characterized by the interaction of the different phases.

Characterization of a multiphase flow can be completed by either experimental or numerical methods. Experimental methods are used to empirically determine what dominant physical phenomena describe phase interactions, known as phase coupling. Numerical methods use a variety of approaches that develop mathematical models of the phase coupling to simulate a particular multiphase flow system over time. Modeling phase interactions within a system is highly desirable to industry because of the cost to benefit ratio between designing a physical experiment and developing a numerical experiment that would be simulated on a computer.

A multiphase flow can be categorized into two groups, a dense or dispersed flow. Dispersed flows are dominated by particle-fluid interactions where the continuous fluid affects the particle motion and vice-versa. A dense flow is dominated by particle-particle interaction and is described by a high frequency of particle contact or collisions. A nearly settled bed is an example where particles have a high contact frequency principally affecting the fluid dynamic forces (lift and drag) of the system. In more energetic systems, collisions between particles occur more frequently affecting the particles themselves by rebounding, breaking up, or coalescing.

Both flow types are modeled using phase coupling where the transfer of mass, momentum, and energy influence the behavior the phases by various parameters. Phase coupling is described as one-way, two-way, three-way or four-way. One-way coupling occurs when the flow of one phase affects the other without reverse effects. If a mutual effect occurs between phases, then the flow is considered two-way coupled. In more complicated cases, i.e., when particle disturbance of the continuous fluid locally affects

another particle's motion, e.g. wakes, or particle collisions affect particle motion three- and four-way coupling are used.

2.2 Fluidization

This section discusses the hydrodynamic principles of fluidized beds and the major generalizations of fluidization. The point of this section is to relate the major characteristics of fluidization to important empirical relations. Fluidization is the act of passing a dilute phase (fluid or gas) vertically through a dense phase (solid granular material) until the system achieves fluid like properties. Gas as a fluidizing medium will be the focus of this particular study. Fluidization occurs due to the counterbalance of gravity with the drag force of individual particles. When fluidization transpires, the friction between particles generally is small enough that the constituent components behave much like a fluid. The quality of fluidization is affected by the size and distribution of the dense phase, the gas to solid ratio, the geometry of the fluidization vessel, gas inlet arrangements, the type of solids used, and whether the solids are free-flowing or liable to agglomerate (Kunii and Levenspiel 1991). This section contains three subsections, all of which detail the major generalizations of fluidization: 1) fluidization regimes, 2) bubbling and gas holdup, 3) minimum fluidization velocity.

2.2.1 Fluidization Regimes

The velocity at which the continuous phase travels vertically through the particulate phase is important to the characteristic behavior of the bed. It is common to generalize this with the term superficial gas velocity because the velocity of the rising gas can vary

throughout the bed. The superficial gas velocity, U_g, is the volumetric gas flow rate through the bed divided by the bed cross-sectional area (Krishna, Van Baten et al. 1998). At sufficiently low U_g, the gas merely percolates through the voids between bed particles and is called a fixed bed. However, as U_g increases, the system transitions to an incipiently fluidized bed. Here gravity is counterbalanced with the drag between individual particles and the rising gas, known as the state of minimum fluidization. At this point the superficial gas velocity is known as the minimum fluidization velocity, U_{mf} (Brown 1997). As U_g increases further, particle motion increases, leading to two types of behaviors: 1) homogeneous and 2) heterogeneous fluidization. Smooth or homogeneous fluidization occurs for small density differences between the gas and solid particles. Here the bed expands smoothly with a well-defined upper surface with the superficial gas velocity known as the transition velocity, U_{trans} (Krishna, Van Baten et al. 1998). U_{trans} generally occurs over a small range of superficial gas velocities, depending on material particle sizes (Singh and Roy 2005). The opposite is true for bubbling or heterogeneous fluidization, which produces channels, jets, and rising voids or bubbles within the bed. The superficial gas velocity at this point is known as the minimum bubbling velocity, U_{mb}. At sufficiently high U_g, elutriation occurs when particles, exceeding their terminal velocity, can be ejected from the bed. There are two types of behavior that occur at this point, slugging and lean phase fluidization, both of which are used in pneumatic transport.

2.2.2 Bubbling and Gas Holdup

Bubbles are defined as large, rising voids resulting from flow instabilities that occur due to flow around the bed material (Brown 1997); however, during gas-solid fluidization,

these voids are not considered conventional bubbles (Kunii and Levenspiel 1991). They exhibit similar behavior as real bubbles in a liquid, but are supported by inertial forces, not surface tension. Bubbles form in different ways depending on the type of aerator used to pass gas into the bed. A perforated plate is used in this study and when $U_g > U_{mf}$, the gas that passes through a perforated plate will begin to from jets that have a length dependent on U_g and the gas and solid properties. Instabilities at the end of these jets form voids that grow larger, when large enough these voids 'detach' from the jet and slowly rise as small, spherical bubbles.

As bubbles rise, they coalesce with neighboring bubble streams that tends to occur towards the bed center (Geldart 1973). The action of coalescence generally forms large, spherically-capped bubbles that rise relatively quickly; much like those observed in viscous fluids with negligible surface tension (Kunii and Levenspiel 1991). While rising, the large bubbles form closed laminar wakes with large wake angles (Clift, Grace et al. 1978) and are surrounded by a cloud region that consists of relatively large amounts of interstitial gas and small amounts of bed material. The interstitial gas fluidizing the bed rises at a higher rate than that within the bubbles. Moreover, the interstitial gas is exchanged with the gas of larger bubbles by passing through from bottom to top, helping to feed and stabilize them.

Particle circulation zones just above the aeration zone force newly formed bubbles towards the bed walls as they rise, see Fig. 2.1. When the bubbles have risen sufficiently high, they begin to interact with another, larger particle circulation zone just above the smaller. Both these zones in tandem force the bubbles towards the bed center, where the majority of bubble movement takes place. As bubbles begin to form and rise in the bed, the bed material becomes entrained in bubble wakes and flows upward, while particles outside

these wakes flow downward (Brown 1997). A fluidized bed is thus known for having excellent mixing characteristics (Lim, Zhu et al. 1995), heat transfer properties (Grace 2006), and an increased fluidization quality (Singh and Roy 2005) due to an increased transfer of energy between phases.

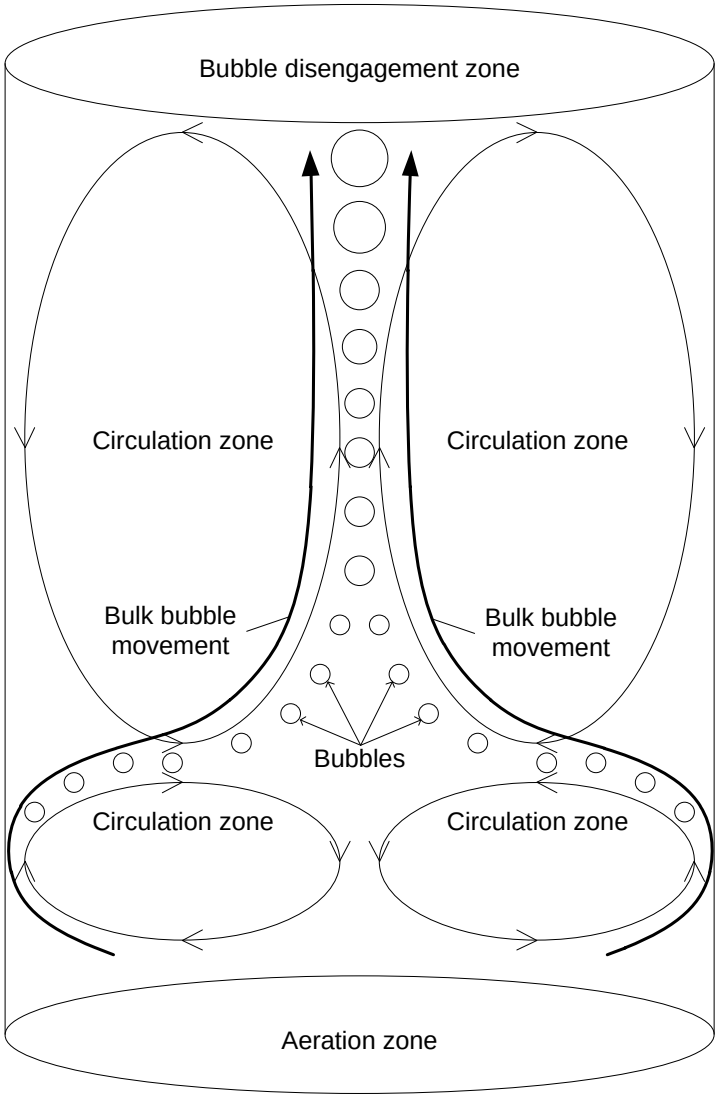

Figure 2.1: A schematic of the circulation zones within a dynamic fluidized bed.

Bubble dynamics within the bed are determined by the physical properties of the particulate phase and reactor geometries (Singh and Roy 2005). In fact, bubbles tend to rise

faster in larger diameter reactors (Pannek and Mleczko 1997), because large scale mixing patterns have the effect of accelerating bubble swarms caused by eddies (Ellenberger and Krishna 1994). Furthermore, the point of transition to a bubbling bed is very sensitive to particle size and distribution in the bed, gas density, and system pressure (Krishna, Van Baten et al. 1998; Grace 2006). A decrease of gas or particle density will decrease the range over which U_{trans} occurs (Ellenberger and Krishna 1994). As particle size increases from fine to coarse, the range of U_g that defines U_{trans} decreases to a point where $U_{mf} = U_{mb}$ (Schouten, Vander Stappen et al. 1996).

The first successful bubble model was developed by Davidson and Harrison (1963). He postulated that: 1) the bubble is solid free and circular, 2) the bubble pushes the particulate phase aside, and 3) the interstitial gas is incompressible and viscous, satisfying Darcy's Law. Collins (1965) and Stewart (1968) posed similar postulates but chose kidney shaped bubbles with indented bases. Jackson (1963) used a spherical bubble but postulated that the volumetric amount of the particulate phase varied.

2.2.3 Minimum Fluidization Velocity

The minimum fluidization velocity, U_{mf}, is the superficial gas velocity at which the bed begins to fluidize. This superficial gas velocity is a function of the bed material particle geometry and density, gas density and viscosity, and reactor geometry. Various correlations given in the literature have been used to calculate U_{mf} (Grace 2006). However, because the before mentioned parameters can only be found empirically, U_{mf} is generally established experimentally (Davidson and Harrison 1963). The process for determining U_{mf} is explained in detail in section 3.3.1. Using this method, it has been shown that as bed diameter

increases, U_{mf} decreases (Hilal, Ghannam et al. 2001; Wu, Yu et al. 2007); an increase in particle size or density will increase U_{mf} (Geldart 1973); and an increase in gas density or viscosity will decrease U_{mf} (Grace 2006).

2.3 Bed Materials

This section overviews the type of material that can be used as the particulate phase of a fluidized bed. Two subsections discuss: 1) material classification requirements and 2) material size distributions. The classification of particle types into groups came about because of confusion by researchers regarding how to apply conclusions made for particular powders in one system to another. As was shown, the characteristics displayed by one powder may not be representative of others in the same system (Geldart 1973).

2.3.1 Material Classification

In 1973, a seminal paper discussing how to generalize particulate materials for fluidized beds was written by Geldart (1973). This paper provided four standard particle classifications shown in Fig. 2.2. Particle types are divided into four groups by comparing the difference of the particle density with that of the fluidizing medium ($\rho_{particle}$- ρ_{gas}) as a function of particle diameter. According to Geldart (1973), the four categories are: A) aeratable, B) sand-like, C) cohesive, and D) spoutable.

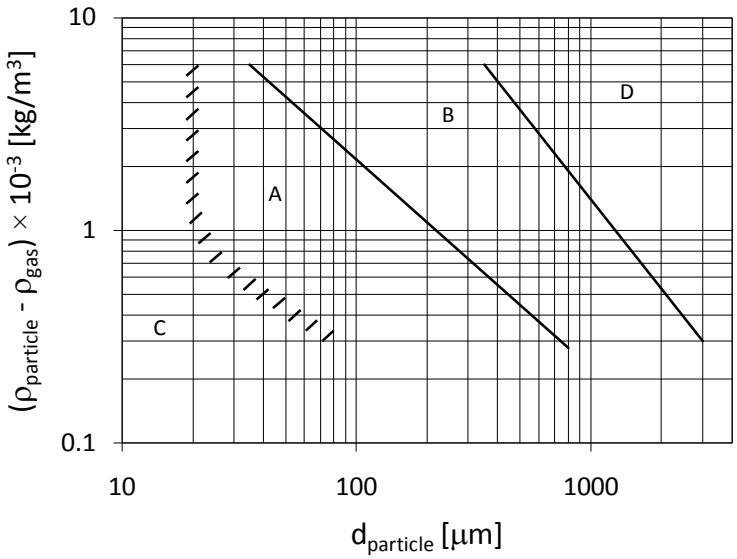

Figure 2.2: The Geldart particle classification chart (Geldart 1973).

Group A particles are fine powders (20 μm < $d_{particle}$ < 100 μm, $\rho_{particle}$ < 1400 kg/m^3), such as cracking catalysts. These materials display a long U_{trans}, meaning these beds reveal large expansions before the onset of bubbling. Bed circulation is extensive with this group and collapses slowly when the gas flow is suddenly shut off. Much the opposite, group B particles are relatively large particle powders (40 μm < $d_{particle}$ < 500 μm, 1400 kg/m^3 < $\rho_{particle}$ < 4000 kg/m^3), much like refractory sand. Particulate beds of this material type have little to no U_{trans} and typically will transition straight to bubbling from insipient fluidization. Therefore, these beds have little expansion and a rapid collapse when the gas flow is suddenly shut-off. Moreover, particulate circulation is extensive during bubbling only.

Group C particles are powders much finer than group A (20 μm < $d_{particle}$ < 40 μm, $\rho_{particle}$ << 1400 kg/m^3), much like concrete or flour. They exhibit strong cohesive bonds most likely due to electrostatic charge, which the continuous phase typically cannot break. Beds composed of these particles are very hard to fluidize normally, where continuous phase

either slugs in small diameter beds or channels in larger beds. Therefore, less conventional methods must be employed in tandem with the conventional aeration, such as, inserted mechanical stirring rods or vibrators attached to the reactor to break up channels, or the addition of sub-micron particles to induce agglomeration. Lastly, group D particles are typically large aggregates when compared to all other groups ($d_{particle} > 500$ μm, $\rho_{particle} < 4000$ kg/m^3), examples being gravel or coffee beans. Mixing in these beds is relatively poor where spouting is common and bubble formation is generally not observed.

2.3.2 Size Distribution

The size distribution of the particulate phase is very important to fluidized bed hydrodynamics. If there is a large size distribution, the smaller particles will fall into the spaces between larger particles and become fluidized in these spaces before the larger particles do. This phenomenon gives an intermediate fluidization point which may be much lower in terms of U_g than U_{mf} when the bed is fully fluidized. In fact, it has been suggested that when analyzing U_{mf} for wide size distributions, a range of U_g is more appropriate than a single point (Zhao and Zheng 2007). On this note, it is often hard to obtain a mono- or bi-modal size distribution of any type of particulate unless it is of a large aggregate. Therefore, it is common to use a specific particle size range for fluidization. A common technique for attaining a particular size distribution is by sieving, a mechanical method of separating unwanted particulate sizes from wanted by agitating the material through a series specific sized mesh.

The effect that particle size distribution (PSD) has on fluidization is well studied for Geldart type B and D materials. Incipient fluidization velocities have been shown to be

comparable between a Gaussian distribution of types B and D to a narrow reference PSD (Gauthier, Zerguerras et al. 1999). However, when compared to a wide reference PSD and a binary mixture, large amounts of segregation occurred, where the segregated ranges fluidized at different superficial velocities. Sahoo et al. (2005) developed a correlation describing the mixing and segregation behavior for these types. Observations were made of their mixing at various heights within a fluidized bed reactor as different mixed ratios were injected through the side of the reactor. It was found that as the injection height increased, mixing and segregation decreased within the bed. Gao et al. (2009) showed interesting results of mixing and segregation of Geldart type B and D using experimental and computational fluid dynamic methods within a turbulent fluidized bed. It was observed that a binary mixture at low U_g segregate, while at moderate U_g they mix well; however, at high U_g, segregation tends to occur again where the fine particles become entrained and move to the upper regions of the bed.

2.4 Fluidized Beds

This section discusses the important features of fluidized beds and their behaviors. Fluidized beds are vital components to many industrial processes, including the production of biofuels, pharmaceuticals, and numerous petroleum and chemical products. Many noticeable behaviors can be observed of a fluidized bed, such as: light objects float; the upper surface stays horizontal when tipped; waves can be generated on the surface; and sound propagates through the bed (Brown 1997). Fluidized beds have certain properties that give rise to various advantages over other processing systems. The smooth, liquid-like flow of particles allows continuous automatically controlled operations with easy handling. The rapid mixing

of solids leads to close to isothermal conditions throughout the bed; hence the operation can be controlled simply and reliably (Kunii and Levenspiel 1991). The well-mixed solids represents a large thermal flywheel that resists rapid temperature changes, responds slowly to abrupt changes in operating conditions, and gives a large margin of safety in avoiding temperature runaways for highly exothermic reactions. The circulation of solids between two fluidized beds makes it possible to remove (or add) the vast quantities of heat produced (or needed) in large beds. A fluidized bed is suitable for large-scale operations. Heat and mass transfer rates between gas and particles are high when compared with other modes of contacting (Grace 2006). The rate of heat transfer between a fluidized bed and an immersed object is high; hence heat exchangers within fluidized beds require relatively small surface areas.

Fluidized beds also retain some disadvantages. For bubbling beds of fine particles, the difficult-to-describe flow of gas, with its large deviations from plug flow, represents inefficient contacting. This becomes especially serious when high conversion of gaseous reactant or high selectivity of a reaction intermediate is required (Kunii and Levenspiel 1991). The rapid mixing of solids in the bed leads to non-uniform residence times of solids in the reactor and for the continuous treatment of solids; this gives a non-uniform product and poorer performance, especially at high conversion levels. For catalytic reactions, movements of porous catalyst particles, which continually capture and release reactant gas molecules, contribute to the back-mixing of gaseous reactant, thereby reducing yield and performance (Kunii and Levenspiel 1991). Friable solids are pulverized and entrained by the gas and must be replaced and the erosion of pipes and vessels from abrasion by particles can be serious. Lastly, for non-catalytic operations at high temperature, the agglomeration and

sintering of fine particles can require a lowering in temperature of operations, thereby reducing the reaction rate considerably.

Two subsections follow: 1) a brief overview of fluidized beds and the types of fluidized bed reactors; 2) the history and applications of fluidized bed reactors in particular the reaction types.

2.4.1 Reactor Overview

Fluidized beds can be grouped into two different operation types, based on the process involved and the vessel which contains it: 1) the fixed fluidized bed (FFB), also known as a dense phase or conventional fluidized bed; and 2) the circulating fluidized bed (CFB), also known as a dilute phase fluidized bed. See Figure 2.3 for a generalized FFB reactor design. The difference between the two is that in a FFB, the bed material does not leave the reactor, while it is entrained out of the reactor in a CFB and cycled back through various means. Each operation type can be arranged in one of three fluid-particulate system configurations: gas-solid, liquid-solid, or gas-liquid-solid. The focus of this research is with nonreactive cold flow FFB reactors using the gas-solid configuration. A detailed review of the CFB reactors has been written by Grace (2006) and Dudukovic et al. (1999).

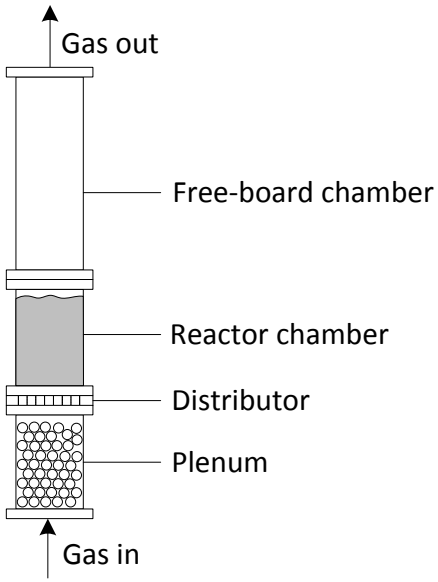

Figure 2.3: Diagram of a FFB reactor.

A nonreactive cold flow FFB reactor is a vessel in which a system of granular material is fluidized at conditions in all regimes but slugging and pneumatic transport. The general FFB reactor consists of 4 major components: 1) a plenum chamber or windbox, 2) the distributor, 3) the reactor chamber, and 4) the free-board chamber (Figure 2.3). Although, many different configurations and geometries have been studied, these components are common to all fluidized bed reactors.

Gas is injected into the reactor through either a plenum with a porous or perforated plate distributor, a straight-hole drilled pipe oriented in various directions, a straight vertical pipe grid, a single or grid nozzle system, or a bubble cap (Brown 2003). This study employs the plenum with plate aeration method for fluidization gas injection. The plenum with plate aeration design generally consists of a small chamber, topped with either a porous or perforated plate. The plenum theoretically distributes the gas uniformly across the bottom of the plate, while the plate holds bed material above it in these systems. However, with all

others, the bed material fills the region were the gas phase enters the system through the various pipe, nozzle, or cap injectors, called the aeration zone, of the reaction chamber.

After the gas phase passes out of the injector or through the aeration plate, it then travels to the reactor chamber. Once in the reactor chamber, the gas then begins fluidizing the particulate bed contained within. As the bed material is fluidized, depending on the superficial gas velocity, bubbles will begin to form and rise, entraining bed material in their wakes. As the bubbles erupt from the top of the bed, bed particles will be ejected from the bed into the free-board chamber. This chamber is used to keep the bed material from passing out of the reactor.

2.4.2 History and Applications

Fluidized bed applications can be divided into four types: 1) gas catalytic reactions, 2) gas-phase reactions, 3) gas-solid reactions, and 4) physical processes. The first type describes a reaction taking place on a catalyst surface with the continuous phase, such as the Fischer-Tropsch (F-T) process. The second type uses a solid, such as refractory sand, to supply heat for a reaction or to transport heat out of the system. An example would be the thermal cracking process. The third type is a reaction where both gas and solids are the reactants. Gasification is an example of this reaction type. The fourth type does not have a reaction that occurs but describes a physical process, for example, particle drying. The reactants and products from the first and second reaction types are both contained in the continuous phase. In the third reaction type the reactants are both solid and gaseous while the products contain either 1) only a gas phase or 2) a combination of both gas and solids, such as ash.

The FFB reactor was the first to be realized for industrial applications, and used to gasify coal by the German engineer Fritz Winkler in the early 1920's. Winkler (1922) patented this gasification technology in 1922 and the first large scale industrial unit was built in Leuna, Germany in 1926 (Yates and Simons 1994). Little advancement in the technology took place between the Winkler patent (1922) and 1942 when the Fluidized Catalytic Cracking (FCC) process of kerosene by the Standard Oil Company was developed. The Standard Oil Company built the first industrial FCC unit in Baton Rouge, Louisiana for this process (Yates and Simons 1994). Their improvement led to a great interest in fluidized bed reactors because of their ability to convert large amounts of petroleum into usable energy efficiently and relatively cleanly. The study of these reactors soon blossomed, first concentrating on the fluidization characteristics of the fine particles used in the FCC process, then moving on to more coarse materials. Soon after more uses were realized such as the roasting of sulfide ore in 1947, the drying of dolomite particles in 1948 and the introduction of the Fischer-Tropsch plant in the 1950's for the conversion of natural gas to gasoline.

The large interest in this technology soon demanded a deeper understanding of the mechanics and hydrodynamics of the reactors for modeling purposes. Toomey and Johnstone (1952) proposed the first generalization, defining the minimum fluidization velocity, stating that all excess gas in the bed acts much like bubbles in a column of water. They noticed that the mixing of the bed material was due to an entrainment of particles in the wakes of upward moving bubbles, giving the bed excellent heat transfer properties. They also found that gas by-pass limited the gas-solid reactions in the bed because of the large amounts of gas within bubbles that were devoid of bed material. These empirical studies eventually led to the proposal of the first theory of bubble motion in 1961 by Davidson

(1961) and is reviewed in section 2.2. The second major generalization for fluidized beds came from Geldart (1973), where bed material types were characterized by the difference in particle and fluid density and mean particle size as explained in section 2.3.

2.4.2.1 Gas Catalytic Reactions

This section discusses two processes: 1) the FCC process and 2) the Fischer-Tropsch process. The FCC process uses a CFB reactor and involves the use of a bed of hot solid catalysts to crack long chains of hydrocarbons into smaller more useful products. The general feedstock is crude oil which, when cracked, produces gasoline, kerosene, diesel, and light olefins. The mix of catalyst and feedstock enter the reactor through the bottom where the feedstock vaporizes, then is cracked. The smaller products in the form of a gas rise, leaving the reactor through a flue vent. As the process continues the catalyst becomes deactivated by rejected carbon attaching to the surface, rendering it useless. The catalyst is circulated out of the reactor to a regenerator where the carbon first passes through steam stripping to remove any absorbed products, then moves to a furnace to burn off the rejected carbon. The hot catalyst is then cycled back into the feedstock and injected into the reactor again. FFB reactors were originally used for this process but limitations in solids handling and transportation, heat input and removal, gas-solid contacting, and process capacity forced a change to the CFB reactor (Jahnig, Campbell et al. 1980).

The FCC process is the largest application of fluidized bed technology in the world with over 350 units and is considered the heart of the crude oil refinery (Grace 2006). This process was the second to be implemented industrially by the Standard Oil Company in 1942 (Yates and Simons 1994); however, the first catalytic cracking unit was used in 1916 with

aluminum chloride as the catalyst (Grace 2006). This catalyst proved to be too expensive and was abandoned until the 1930's. In 1931, Houdry developed an inexpensive catalyst from natural clay called Fuller's Earth containing aluminosilicate and joined with the Vacuum Oil Company to develop an FFC unit using his new catalyst.

The F-T process uses solid catalysts to synthesize CO and H_2 into long chains of liquid hydrocarbons through the use of high temperatures (150 to 300 °C) and high pressures (10 to 17 bar). Typically, natural gas or the product of coal or biomass gasification, called synthesis gas, 'syngas', or producer gas, are used as feedstocks to produce products such as synthetic lubrication oils or fuels. Unlike the FCC process, the catalyst does not become deactivated and does not need to be cycled and recovered; therefore, FFB reactors are generally used.

The F-T process was developed by two German chemists Franz Fischer and Hans Tropsch in the 1920's. The first attempt to use a fluidized bed with the F-T process occurred in Brownsville, TX in 1951 (Steynberg and Dry 2004); however, the production efficiencies of this attempt were very low and it was abandoned. The original feedstocks for the F-T process were coal but moved to natural gas because of the ease and efficiency of conversion to light hydrocarbon liquids (Kunii and Levenspiel 1991). A successful operation was built in Sasolburg, South Africa in the mid-1950's for South African Synthetic Oil Limited (Sasol) by Kellogg. Kellogg built the plant originally with CFB reactors to crack the coal before the F-T conversion took place; however, it was discovered that a FFB reactor was more efficient and less costly (Grace 2006).

2.4.2.2 Gas-Phase Reactions

Two processes are discussed in this section: the thermal cracking process and the coking process. The thermal cracking process is similar to the FCC process in that rejected carbon accumulates on bed material surfaces, called coking. However, the bed material is not a catalyst, acting only as a heat carrier at temperatures ranging from 700 to 750 °C, which cracks crude or heavier oil feedstocks into lighter hydrocarbons. Because of particulate coking, thermal cracking is generally completed using two reactors: either two FFB reactors, two CFB reactors, or a combination of the two. One reactor completes the reaction process, while the other regenerates the bed material by combustion of the rejected surface carbon. This generates the heat for the cracking process as bed material is exchanged from reactor to reactor. Moreover, catalysts can be added to the bed material to combine the FCC process with the thermal cracking process, enriching the reaction efficiency of certain products (Gartside 1989; Deng, Wei et al. 2002).

Luigi and Fujinagata developed an early thermal cracking process in the 1950's using sand particles to carry heat that cycled between two reactors and drove the reaction (Kunii and Levenspiel 1991). Badische Anilin und Soda-Fabrik (BASF) of Germany, and the Ministry of International Trade and Industry (MITI) of Japan, in the 1960's implemented pilot plants using the thermal cracking process to produce light olefins from crude (Grace 2006). The conversion rates from these plants were relatively low because of gas backmixing and long residence times of the feedstocks. This problem was addressed by Stone and Webster in the 1970's with a new reactor design, called the QC reactor, which lowered the contact time between the feedstock and the inert bed material (Gartside 1989).

During the coking process heavy residual petroleum feedstocks are converted into lighter hydrocarbons in the form of gas. Although this process is much like the thermal cracking process, the difference is that the by-product of the reaction, coke, is used as the bed material. Moreover, carbon-carbon bonds are broken with this process, whereas, the breaking of carbon-hydrogen bonds occurs during the thermal cracking process. Here, coke forms from rejected carbon during the reaction in a CFB reactor operating at temperatures ranging from 480 to 550 °C. Generally, the feedstock enters through a side port injector while steam enters from the bottom of the reactor to fluidize the bed and strip any products absorbed by the coke. As the reaction proceeds, coke accumulates within the bed. During bed circulation, some coke is combusted in a furnace transferring heat to other particles that are cycled back into the bed that supply heat for the coking reaction. The two largest industrial coking units in the world are located in Alberta, Canada, where heavy bitumen from oil-sand is cracked to produce naphtha and gas oils (Grace 2006).

2.4.2.3 Gas-Solid Reactions

This section discusses three processes: 1) coal combustion and gasification, 2) pyrolysis and gasification of biomass, and 3) roasting and calcination. Generally, a CFB reactor operating at a temperature range between 750 to 900 °C is used during the coal combustion process with a bed of inert material, such as sand, and is fluidized by oxygen-enriched air. Coal particles are injected by a side port auger that devolitize into gases that are burned; eventually it decomposes into char that is burned and produces ash. The heat produced from this process is transferred out of the reactor by heat exchange rods that cycle

water that is converted to steam to run turbine generators. An advantage for combusting coal this way is the capture of many pollutants that would otherwise be released.

Combustion of coal with fluidized beds was not an interest for research until the late-1950's when the National Coal Board in Great Britain instituted studies to increase coal consumption (Oka and Anthony 2004). In fact, fluidized bed coal combustion did not become a large part of the energy sector until the mid-1970's when the first oil crisis hit. As of 1990, 120 fixed fluidized bed combustion reactors and 112 circulating fluidized bed combustion reactors were in operation, with upwards of 54 companies that produced these reactors (Basu 2006).

The process of coal gasification is generally performed in a CFB reactor operating in a temperature range of 800 to 900 °C, although it originally was completed in a FFB reactor. The bed consists completely of coal particles which are augured in through a side port and fluidized with a combined stream of oxygen-enriched air and steam. The process produces a relatively clean syngas that, when burned in a gas-turbine-steam-turbine binary cycle, generates power at higher efficiencies than the coal combustion process. Moreover, the relatively clean producer gas is also a feedstock for the F-T process and can be used as a gaseous fuel or synthesized to raw chemicals.

Fritz Winkler (1922) showed that coal gasification was possible in the early 1920's with the Winkler gasifier (Grace 2006). By the 1950's, the cost of converting natural gas had become so competitive with coal gasification for the same products that most of all Winkler units had been shut down (Kunii and Levenspiel 1991). However, the oil crisis in the mid-1970's gave way to a renewed interest in coal gasification and new reactor designs began to appear.

During the process of biomass gasification, feedstocks such as agricultural and wood processing residues, grass, and short rotation woody crops are converted into gaseous fuels. This process generally takes place inside a CFB reactor where an air-steam stream is combined with the feedstock prior to entering the reactor. The reaction of the feedstock at high temperatures, generally above 700 °C, with a controlled amount of oxygen and steam in an inert bed material, separates the chemical energy from the solid biomass. First, any moisture is removed from the biomass particles, which are then pyrolyzed in the absence of oxygen to produce oils, char, tar, and gases. The pyrolysis oil, also called bio-oil, can be used as transportation fuels, while pyrolysis gases can be used for power generation. Biomass gasification is a relatively new process and still in its infancy in terms of technologies. However, China has built two biomass gasification and power generation (BGPG) pilot plants that produce a combined 2.5 MW of power using CFB reactors (Wu, Huang et al. 2002).

Roasting and calcination within fluidized beds is generally applied to minerals and metals. Roasting usually takes place in a FFB reactor, operating in the bubbling regime and fluidized by hot air. Calcination is usually performed in a CFB reactor where combustion of natural gas or fuel oil is used to heat the bed and fluidized by air. The first commercialized CFB calciner was built by Lurgi in the late-1960's (Reh 1971; Reh 1986).

2.4.2.4 Physical Processes

Three applications will be discussed in this section: 1) drying, 2) heat exchange, and 3) coating. During the drying process, mass in the form of steam is removed from the particulate bed by a hot air stream, which proceeds in two stages. First, surface moisture is

removed during a constant rate stage and second, moisture from inside the particle is removed during a reduced rate stage. The first stage is fast, demanding large amounts of air flow, while the second is slow. This process generally uses FFB reactors that cycle wet particles in through an inlet near the top of the reactor and removes dry particles by an outlet near the top of the dynamic bed. The use of a fluidized bed as a heat exchanger is similar to this because of the circulation of chilled water through pipes inserted in the bed that is converted to steam. The high heat transfer rates and large heat capacities of specific bed materials make this method an efficient way to exchange heat.

Coating particles within a fluidized bed has become increasingly popular in recent decades. The pharmaceutical industry has used this process with FFB spouting reactors to apply a thin layer of gels to medications for smooth ingestion. The coating is generally applied through a feed sprayer located in the center of the reactor above the bed. As the bed is fluidized with hot air, the sprays gently covers the bed as heavier sprayed particles fall to the bottom and are augured or conveyed out of the reactor.

2.5 Multiphase Flow Measurement Techniques

This section describes the various techniques that can be found in the literature to observe multiphase flows. Multiphase flow measurement is largely empirical with experiments covering a limited range of operating conditions and physical properties. The measurements of interest applied to fluidized beds encompass the following: void fraction and solids concentration, bubble size distribution and rise velocity, and liquid and solid phase velocities. These measurements help to corroborate existing correlations and verify models, and for interpreting, understanding, and predicting reactor performance. Noninvasive

measurement techniques are covered in depth by Chaouki et al. (1997), and will be briefly overviewed here.

This section is split into four subsections, the first of which focuses on gas holdup and solids concentration measurements, in particular the global and local measurement techniques involved. The second subsection covers bubble size and velocity measurements, and the third subsection covers measurements of liquid and solid phase velocities. The fourth subsection covers X-ray visualization techniques, focusing on radiography, stereography, and tomography.

2.5.1 Gas Holdup and Solids Concentration Measurement

Measurements of gas holdup and solids concentration are categorized as either global or local. Global measurements are averages of phase fraction within 2D or 3D spaces. Local measurements are point measurements within a volume. The acquisition of data for both measurements can be invasive or non-invasive. An invasive measurement technique is the collection of data by a probe in direct contact with the flow, which presents problems with the reliability of data by hydrodynamic disruption (Geldart and Kelsey 1972). These techniques are generally used for local measurements, while global techniques generally use non-invasive methods. Global techniques use radiological methods of detecting the attenuation of electromagnetic radiation; therefore, detection equipment is not in direct contact with the flow to acquire data. However, there are exceptions to both global and local measurements, which will be described in the following subsections.

2.5.1.1 Global Measurement Techniques

Gas holdup or volumetric gas fraction, ε_g, can be inferred in many ways depending on the multiphase system being studied. Some (Clark and Flemmer 1985; Zhou and Egiebor 1993; Inga and Morsi 1999) have used the static, H_0, and operating, H_g, liquid or slurry heights with gas-liquid or gas-liquid-solid systems to define ε_g:

$$\varepsilon_g = \frac{H_g - H_0}{H_g} \tag{2.1}$$

Precise measurements of H_g can be problematic because of bubble disengagement or large changes in the free surface of the liquid or slurry. Invasive techniques have used hot film anemometry (Deckwer, Lousi et al. 1980) and floats, as is frequently employed in industry due to the size and opaque nature of the reactors (Kumar, Dudukovic et al. 1996). Clark (1987) developed a non-invasive method using neutron attenuation to detect the free surface of a liquid in a variety of opaque bubble columns, which can also be used for opaque fluidized bed systems. Moreover, H_g could be measured using the attenuation detection techniques of other bands within the electromagnetic spectrum, such as X-ray or γ-ray. However, if the reactor is transparent, H_g can be inferred visually. All techniques result in an average where observations are made over a period of time.

Another method for estimating average gas holdup in gas-liquid systems uses the difference in hydrostatic head over the difference in height, described by Hills (1976) and Merchuk and Stein (1981). A measure of the pressure (dP) and height (dh) differences are used to calculate gas holdup:

$$\frac{dP}{dh} = -\rho_l g\left(1-\varepsilon_g\right) \tag{2.2}$$

where ρ_L is the liquid density. The acquisition of pressure is made through taps over a range of locations along the height of the reactor with various types of pressure probes or meters. Consequently, this method is invasive because the flow can be disturbed due to the taps. This technique can also be used with gas-solid and gas-liquid-solid systems, however, it is not recommended because of tap clogging issues from fine particles. Moreover, the use of Eqn. (2.2) is not valid if the liquid flow rate is non-negligible, where an account of the wall shear stress, τ_ω, reactor diameter, D_c, and liquid flow rate, U_l, must be made. The following equation derived by Merchuk and Stein (1981) gives the appropriate solution for the average gas holdup in this case:

$$\varepsilon_g = \left(1 + \frac{dP}{dh}\frac{1}{\rho_l g}\right) + \frac{U_l^2}{g}\frac{1}{\left(1-\varepsilon_g\right)^2}\frac{d\varepsilon}{dz} + \frac{4\tau_\omega}{\rho_l D_c g} \tag{2.3}$$

where the wall shear stress can be found through correlations or tables using the friction factor.

The hydrostatic head method has been widely used to study average gas holdup in the relatively recent past. Gas velocity, system pressure, and catalyst loading effects on gas holdup of H_2, N_2, CO, and CH_4 in an organic mixture were studied by Inga and Morsi (1999) in a slurry bubble column reactor. Using this method Godbole (1983) studied the effects of gas velocity and solids presence on gas holdup structure, gas-liquid interfacial area, and volumetric mass transfer coefficients in a large diameter bubble column. Tang and Heindel (2006) estimated the gas holdup in a cocurrent gas-liquid-solid bubble column using a variant of Eqn. (2.3).

Three-phase systems are extremely difficult to monitor and collect data from, in fact, only one method was found in the literature to effectively obtain global system gas holdup.

This technique is known as the bed expansion technique, where differences in bed heights at steady and fixed states are used. Assuming the bed mass is constant, then bed expansion is completely due to the introduction of gas to the system; therefore, the following analysis would calculate the average gas holdup:

$$\varepsilon_g = \frac{\text{Steady state bed volume-Fixed state bed volume}}{\text{Steady state bed volume}} = \frac{H_g - H_0}{H_g} \tag{2.4}$$

Other forms of three-phase monitoring have become more effective over the recent past such as radiation attenuation; however, these methods are expensive and have safety concerns.

X-rays, γ-rays, β-rays, and neutron beams have been used a great deal to monitor multiphase flows in the past three decades, of which X-rays and γ-rays are the most common. These methods entail the use of an emitting source/detector pair. The source emits either a collimated or cone beam directed at a detector facing the source, between which the object of interest (OOI) is observed. A radioactive isotope is employed for γ-ray emission, while X-ray discharge originates from a high voltage source and is explained in greater detail in section 2.4.5. Average system gas holdup analysis using images that are produced using this technique are explained further in section 3.6.1.2, while a detailed description of the gas holdup calculation is given in section 3.7.2. Although, these sections are organized around the study explained in this thesis and deal with the X-ray spectrum, it is applicable to γ-rays, β-rays, and neutron beam attenuation as well. The only difference in application between each is the way each ray is produced.

As was alluded to earlier, three-phase monitoring using radiation attenuation techniques is somewhat problematic because individual phase holdup is nearly impossible to quantify. Although the bed expansion method can give a rather good estimate of ε_g, neither

the liquid nor solid holdups are measureable with this method. However, if each of these phases were to attenuate different electromagnetic energies differently, then an estimate of each phase holdup could be attained. This process, known as the dual energy X-ray computed tomography, can be accomplished with the use of two different γ-ray emitting isotopes with sufficiently different discharge energies or with an X-ray method as was used by Bukur (1996).

Lastly, the method of dynamic gas disengagement can be very effective in estimating average gas holdup by quickly shutting inlet gas valves to the reactor. Disengagement of large and small gas bubbles is then observed and/or the mass of the gas phase is measured as is define by Sriram and Mann (1977). Generally, this technique is used with gas-liquid systems; however, it can be used with gas-solid and gas-liquid-solid systems with moderate solids loading.

2.5.1.2 Local Measurement Techniques

Local gas holdup and solid concentration measurements are generally accomplished using invasive techniques. Various types of probes usually measuring different properties of impedance (Lanneau 1960; Park, Kang et al. 1969; Ozkaynak and Chen 1978; Richtberg, Richter et al. 2005) or optical parameters (Yasui and Johanson 1958; Whitehead and Young 1967; Okhi and Shirai 1976; De Lasa, Lee et al. 1984; Dencs 1996; Matsuda 2008) are inserted into the multiphase flow at different locations. While the use of impedance or optical methods far outweigh the use of others, there are techniques to monitor local phase holdups entailing the use of electrochemical probes (Nakoryakov, Kashinisky et al. 1984), hot wire and film anemometry (Delhaye 1969), and micro thermocouples (Delhaye, Semeria et al.

1973). These techniques are generally the least expensive and safest of all techniques; however, the interpretation of data from the probes can be difficult (Geldart and Kelsey 1972).

The change in conductivity and permittivity of the separate phases in a multiphase flow can be exploited through the use of impedance monitoring. Changes in the flow structure change the conductivity, resistivity, or capacitive effects at the measurement location. While special probes are used for gas-liquid and gas-solid systems, this technique is not capable of monitoring gas-liquid-solid systems. Resistivity probes are more effective in gas-solid systems to measure solid concentrations, while in aqueous systems conductivity probes are generally used; however, dewetting of a conductivity probe becomes a problem with signal response (Yates and Simons 1994). This implies that probe design, placement, and orientation within the multiphase flows are crucial (Groen, Mudde et al. 1995). Local gas holdup or solid concentrations are implied through these measurements using a ratio of the time integrated probe phase submersion over the total time.

Optical probes use the difference in index of refraction for each phase to imply either local gas holdup or solid concentration. This happens at the interface between the probe tip and the multiphase flow, which is generally only used in transparent systems at low void fractions and moderate temperatures. The amount of time that the probe is in a single phase over the total monitoring time gives the local phase holdup or concentration, as with impedance probes. Probe/phase contacting is another downfall of this technique, where if a bubble with a diameter smaller than the probe interacts with the probe, detection is not made.

2.5.2 Bubble Size and Velocity Measurement

Few methods are used to measure bubble size and velocity because acquiring data generally involves optical visualization. This is problematic because of the opaque nature of both the reactor and most multiphase systems. Capturing images of bubbles can take place either invasively or non-invasively, where invasive techniques may use parallel plates installed in the reactor. Non-invasive techniques may utilize both optical (transparent reactors) and radiation attenuation (opaque or transparent reactors) techniques. The images generally are digitized and analyzed with the use of computers, which can be fairly complicated and is discussed further in Chapter 3.

Two point resistivity and optical probes are an invasive means of observing bubble velocities, where two needles or optical fibers are separated by a fixed vertical distance. These probes give a binary output depending on the contacting phase and determine the time delay of the initial to final contacting time of the measured phase between each probe tip. The phase velocity can be calculated using the delay time between the known needle or fiber separation. The bubble chord length is then calculated using the velocity and mean residence time between the probe ends for the gas phase. Cheremisinoff (1986) expressed that close probe separation results in significant variations in measured values of time and will even fail to detect bubbles smaller than the separation distance. The piercing of bubbles off center (Steinemann and Buchholz 1984) and passage of non-spherical bubbles through the probe (Zun and Saje 1982) will produce inaccurate measurements as well.

Another invasive method that exclusively measures bubble velocities is the use of the ultrasound Doppler technique. Ultrasound waves are produced and detected by probes that are inserted into the system at a specific initial location and moved to at least three different

locations to get a viable spatial distribution in different directions. The wave's frequency is shifted proportionally by the bubble velocity when reflected off the bubble interface. Spectral analysis of the resulting data will give a bubble velocity component distribution over the three measurement locations. Unfortunately, this technique will only work with low holdup distributions and temperatures below 150 °C.

Isokinetic sampling probes have been used to measure bubble sizes. In this process, a small diameter probe is used with a flared capillary tube at one end which is bent at a 90° angle. This is an invasive technique, where the probe is placed into the multiphase flow through the side of the reactor with the open end facing the direction of the gas flow. As bubbles rise, some will be captured by the probe and uniformly accelerated by a pump to form a slug within the tube. The intensity of light passing through a transparent section is measured as the bubble passes. Binary variations of the light intensity are recorded, implying different phase types. Using the time and tube cross-sectional area, the bubble volume is estimated.

The global gas holdup measurement technique of dynamic gas disengagement can also be used to measure bubble sizes and velocities (Krishna, Van Baten et al. 1998). By observing changes in the height of the multiphase free surface after gas shut off, the holdup structure of exiting bubbles can be calculated. This assumes that large bubbles exit first followed by the small bubbles and that there is no interaction between the two.

2.5.3 Liquid and Solid Velocities Measurement

There are many ways to monitor the velocity of liquid or solid phases in a multiphase flow system. The Pitot tube is arguably the most widely used device to monitor fluid

velocities in industry, commonly used to help pilots observe relative aircraft speeds. It is an invasive device inserted in the reactor facing the direction of the gas or liquid flow, similar to the isokinetic sampling probe. Dynamic pressure changes are measured away from the reactor walls, while static pressure changes are measured at the walls. Single phase velocities are calculated with these pressure measurements using:

$$\Delta P = \frac{1}{2}\rho v^2 \tag{2.5}$$

were ΔP is the change in pressure for the phase being observed, ρ is the phase density, and v is the phase velocity. However, with the addition of another phase, the calculations become more complex (Euzen, Trambouze et al. 1993):

$$\Delta P = \frac{1}{2}\left(\varepsilon_g \rho_g v_g^2 + J\varepsilon_l \rho_l v_l^2\right) \tag{2.6}$$

were subscripts g and l represent the gas and liquid phases respectively, ε is the phase holdup, and J is the phase coupling factor. This is similar to turbine flow meters, vane probes, and flywheel anemometers where phase velocity calculations increase in complexity with the addition of multiple phases. These devices measure the rotational speed of either the turbine or flywheel to infer phase velocities as the particular phase passes over then. Unfortunately, these devices are only appropriate for flows with low liquid flow rates and dilute concentrations of another phase.

Another widely accepted technique for monitoring phase velocities is hot wire anemometry; however, signal interpretation is somewhat difficult (Delhaye 1969; Resch and Leutheusser 1972; Michiyoshi and Serizawa 1986). According to Kumar et al. (1996), even with these disadvantages, hot wire anemometry is the most convenient and least expensive of

all phase velocity monitoring techniques. Phase velocities are inferred by the degree of convective heat loss through changes in the wire's resistance as the respective phase moves past the wire, which is a function of the multiphase flow velocity and individual phase properties. There are two ways to conduct monitoring, constant and variable resistance modes. The constant mode measures voltage changes, while the variable mode monitors current changes, both changes are due to heat flux changes.

Laser Doppler Velocimetry (LDV), an accurate and reliable phase velocity measurement method, uses two laser beams that intersect within a multiphase flow. This intersection creates an ellipsoidal measurement volume through which small particles seeded in the flow pass. As they move through the monitoring volume, they create variations in the intensity of fringe patterns observed by optical detectors. Particle velocities are calculated using:

$$U=\frac{f_d\lambda}{2\sin\left(\frac{\theta}{2}\right)} \tag{2.7}$$

where f_d is the Doppler shift frequency, θ is the incident angle of the lasers, and λ is the laser wavelength. The passage of bubbles through the ellipsoidal volume must be accounted for in this process because of light scattering, reflection, and refraction; therefore, intensity changes due to bubbles are greatly different than those due to particles. This method requires that the system be relatively transparent to the lasers and particles; therefore, solids loading must be relatively small. Equipment is expensive for this method, which is probably its greatest disadvantage.

Another velocimetry technique also measures the velocity of particles in a seeded flow, particle image velocimetry (PIV). Similar to LDV, PIV uses a sheet of laser light

shown through a section of the flow. As the particles move with the flow, they pass through the laser sheet while images are captured of their position. These images are then digitally analyzed with computers where the individual particles are identified in successive images. These positions are then used to define instantaneous velocities of the particles and average velocity of the flow is inferred from this, where the assumption that the particles move at the same rate as the flow. Particle concentrations must be small for this to work and not affect fluid rheology; furthermore, the flow must be relatively transparent, much like LDV. However, bubbles do not present the same problems as LDV, because of the image processing technique used to identify particles; i.e. bubbles and particles would be identified differently.

Laser induced photochemical anemometry (LIPA), again uses lasers, however, not to illuminate a particle seeded flow, but to induce a reaction within photoexcitable chemicals. As the laser light falls on the flow, these chemicals fluoresce. Sequential images are then acquired and analyzed much the same as PIV; similarly, unlike LVD, there are no scattering, refraction, or reflection problems from bubbles. Solid velocities can be measured in dense flows unlike PIV, yet this is a light specific method because of the chemical reaction needs and is relatively expensive.

Lastly, computer automated radioactive particle tracking (CARPT), measures radioactive particles in a seeded flow, like PIV. However, visual images are not captured and analyzed; detectors record the radiation signal from radioactive particle seeded in the flow to infer particle positions, which are tracked for long periods of time. This is similar to PIV in that the instantaneous positions are analyzed to infer the flow field. The particles used are designed with sizes and densities to match properties of the phase being monitored.

Moreover, this method monitors the radiation signal from a particle where radiation energy can be detected through opaque materials. Additionally, this is a method that can be used to monitor all solid and liquid flows, but design and concentration must be attended to in detail.

2.5.4 X-ray Visualization Techniques

Monitoring opaque multiphase flows using X-ray visualization has proven to be a useful tool in providing good qualitative and quantitative data of dynamic behavior. Successful measurements of time averaged gas holdup (Grohse 1955; Romero and Smith 1965; Rowe, Santoro et al. 1978; Yates and Cheesman 1992; Kantzas, Wright et al. 2001; Ford, Heindel et al. 2008; Franka and Heindel 2009), liquid holdup (Toye, Marchot et al. 1998), solid concentrations (Grassler and Wirth 2000), and phase velocities through particle tracking (Kantzas, Wright et al. 2001; Seeger, Kertzscher et al. 2003; Lee and Kim 2005; Drake, Franka et al. 2008) have been completed using this non-invasive technique. The greatest disadvantages of this technique are that the equipment is expensive and emission of X-rays raises a safety issue that is also expensive to address.

X-rays are produced by ionizing a target metal through bombardment of electrons, called a target source. As the X-rays leave the source, their energy is attenuated while passing through objects in the environment in which they travel. As either the density or thickness of these objects increase, attenuation increases. To quantify the attenuation, an X-ray detector captures images on a screen that fluoresces proportional to the amount of X-ray energy incident with it. If the target source is a flat plate, a cone beam is generated and a 2D projection of a 3D object is recorded by the detector, similar to an image created by a shadow. One type of detector, called an image intensifier, collects the X-ray photons that fall

onto it and converts them to electrons. The electrons are focused (intensified) onto a small region in which a CCD camera is used to capture an image. Another type of detector, known as a syntillator, converts incident X-rays into light through the fluorescing properties of a CsI phosphor screen in which an image is captured. The greater the intensity of the X-rays falling on the screen, the brighter the screen fluoresces. These images can be captured and used in multiple ways, which is the subject of the following three subsections: radiography, stereography, and tomography.

2.5.4.1 Radiography

Single 2D X-ray images, or radiographs, originally were captured with the use of film and analyzed by hand (Grohse 1955). However, since the introduction of the CCD and computer, film has been replaced by digital imprinting and analysis (Heindel, Gray et al. 2008). Generally, X-ray radiographic investigations of process reactors center on the hydrodynamic behavior of fluidized beds; however, it has been applied to bubble and slurry columns. This is also a relevant time dependent tracking technique for single 2D planes and can be extrapolated to 3D position measurements when two source/detector pairs are used in sync at varying acquisition angles, known as stereography.

The first reported use of this method was by Grohse (1955), who measured density variations in a bed of silicon powder as a function of U_g. Although, the results of this study were largely qualitative, it proved that X-ray radiography could potentially be a powerful tool in studying the properties of multiphase flows. A decade later Romero and Smith (1965) showed quantitative results of density distributions and bubble characteristics within a fluidized bed by using flash X-ray radiography coupled with a video cine camera. As

analysis tools improved, Rowe et al. (1978), using the same system, quantitatively showed gas holdup values within a fluidized bed. Gas holdup was calculated by measuring the volume of bubbles that were outlined with a hand-held cursor on a digitizer table where radiographic images where projected. In the following years, the semi-automated acquisition and processing system designed by Yates and Cheesman (1992) using a single source/detector pair fully integrated with a computer was used to measure void fractions. Images were captured and uploaded to the computer where they were digitized and stored for later processing; furthermore, the system could capture time series images for movie playback. The computer doubled as a processing unit as well that could digitally enhance images or remove noise and add artifacts due to the nature of x-ray attenuation. Recently, Heindel et al. (2008) reported the design of a fully automated and computer integrated system that is describe in more detail throughout chapter 3. Lastly, Hulme and Kantzas (2004) used X-ray radiography to monitor bubble size and velocities through a fluidized bed containing 150 – 250 μm diameter glass beads. The identification of bubbles in radiographs was made by a simple thresholding technique that separated the bubble from the background. They found that a large bubble wake structure could be a false indicator of small bubbles when using global thresholding. Therefore, all bubbles were identified by local thresholding using erosion and logic. After calculating the centroid of each bubble, they were able to track them in successive images to find instantaneous bubble velocity. All data compared well with various correlations and models.

2.5.4.2 Stereography

Image stereography, a subset of radiography, is the process of capturing images from two independent directions. Stereography is not constrained to just X-ray detection and can be used with any type of equipment that captures images. Stereography is commonly used in the medical field (Sherlock and Aitken 1980; Moll, Douek et al. 1998); however, recently it has become a useful technique in the study of multiphase flows (Kantzas, Wright et al. 2001; Seeger, Affeld et al. 2001; Striegel 2005; Drake, Franka et al. 2008). This method is generally used to determine the correct 3D position of an object in space relative to a reference point (Sherlock and Aitken 1980; Adamczyk and Rimai 1988; Cowen and Monismith 1997; Kertzscher, Seeger et al. 2004), or extrapolate 3D volumes with center of mass tracking (Cheng and Burkhardt 2003). If the OOI is dynamic, time-lapse images of the behavior is acquired to determine volume changes or displacement between frames. The detector's capture time must be synchronized during acquisition to receive the correct object position and/or volume change in both images if the OOI is in a dynamic state. A more detailed description of these issues is addressed in section 3.5.

The first reported use of X-ray stereography was in the medical field (Mori, Fujimi et al. 1968). A single source/detector pair was used in this study; however, the pair was shifted around a common axis to obtain the needed images. It was demonstrated that a sense of a 3D structure could be obtained with only a 5mm degree of separation between image acquisition points; however, to receive the desired stereograms for 3D reconstruction, separation must be $\geq$ 20mm. A 3D extrapolation of gastrointestinal mucus membranes was constructed with the use of Buscopan as the radio opaque tracer. Few in the field improved the method developed by Mori et al. (1968) outside of including a second synchronized source/detector pair and

installation of more shielding until Sherlock and Aitken (1980). These researchers traced a marker inside of live mammalian subjects within an RMS error of 0.25 mm and the use of X-ray stereography for 3D particle tracking was born.

The use of stereography to reconstruct 3D velocity fields within a multiphase flow has increased in recent decades but is still somewhat limited in results. Guezennec et. al. (1994) referenced many prior works in an effort to find the most efficient algorithms to automate the tracking of particles in turbulent flows. Kertzscher et. al. (2004) and Seeger et. al. (2001) have been perfecting an automated XPTV method for multiphase flows. In fact, Seeger et al. (2001) was the first to report the use of X-ray stereography to trace radio opaque particles within a process reactor containing a multiphase flow. An X-ray phase contrasting technique to visualize flows with large particle size disparities at great concentrations was implemented by Im et. al. (2007). Kim and Lee (2003; 2004) used diffraction at the edges of particles to enhance detection at the microscale when quantifying velocity fields for a blood cell tracking method. An artificial neural network has also been suggested to automate the tracking of large concentrations of particles by XPTV with the intent of reconstructing 3D velocity fields (Lee and Cha 2003; Lee, Cha et al. 2004).

2.5.4.3 Tomography

X-ray computed tomography is the process of examining the attenuated X-rays that have passed through an object to recover an estimate of its internal structure. The spatial, temporal, and density resolutions of X-ray CTscanners are key to defining internal structures of the OOI. Spatial, temporal, and density resolutions are measured by the minimum distance at which two high contrast point projections can be separated, the frequency which

images can be obtained, and the smallest difference of mass attenuation coefficients the system can distinguish, respectively (Chaouki, Larachi et al. 1997).

X-rays energetic enough to pass through the OOI and incident on a syntillation unit will cause the unit to fluoresce. The amount of fluorescence is directly proportional to the incident X-ray energy and, therefore, a good approximation of the density of the material through which the X-ray passed. This fluorescing image, and by extension the attenuation, is recorded by a CCD element (or similar device). The image is processed and stored for later reconstruction into a digital 3D computed tomographic image. These images are then reconstructed by parsing the object into many individual images taken around the object with a fixed axis of rotation and remodeling them together into a coherent 3D digital image. Consequently, if the system is dynamic, i.e. a bubbling fluidized bed, then the reconstructed image is time averaged. This is generally completed by acquiring images at integral degrees completely around a user defined axis through the OOI.

There are many algorithms used for reconstruction depending on the acquisition method and beam type produced from the source. However, the most dependable and accurate method is filtered back projection (Kak and Slaney 1988; Kini 1994). The quality of a X-ray CT depends on the quality of data generated by the scanner. Sources of X-ray CT inaccuracy are the intrinsic statistical variations due to the finite number of photons measured by the detector and the particular form of instrumentation and processing used (ASTM 1997). Statistical noise manifests as random variations superimposed on the X-ray CT, limiting the contrast discrimination. This can be reduced by increasing the signal through increased exposure time, X-ray output, or source and detector size.

Pseudo physical features or artifacts within an X-ray CT are large sources of error when making quantitative calculations, i.e. gas holdup, from X-ray CTs. Artifacts come from two distinct sources, beam hardening and interface density changes (ASTM 1997). Beam hardening is a false radial gradient in the density that causes abnormally low values at the interior center of a uniform object and high values at the edges. Average radiation energy increases as it propagates through an object because the low energy photons are preferentially absorbed. Interface density changes or edge artifacts come from sharp changes in signal level resulting in streaks in the X-ray CT due to mathematical relations in the reconstruction algorithm. System design and post processing practices can drastically reduce these sources of error.

2.6 Summary

The fluidization of materials is a relatively mature technology in the process industries; however, a clear understanding of the complexities of these dynamic systems still is not fully understood. Much progress has been made giving a clearer picture of dynamics through experimentation and modeling. Furthermore, experimental techniques for monitoring multiphase flows are becoming more efficient and less invasive due to technological improvements, which help to validate developed modeling methods. The same influences imparted on experimental techniques also improve modeling through increased computing power and storage. For all the techniques described and reviewed in this chapter to monitor multiphase flows, X-ray attenuation seems to be the most appropriate accounting for cost, safety, and versatility. Although the expense is high and obvious safety issues are a large concern, the ability to glean quality, low error, quantitative and qualitative data more

than outweighs those disadvantages. In the following chapters, this will be impressed upon the reader in greater detail.

CHAPTER 3 EXPERIMENTAL METHODS AND SETUP

Equation Chapter 3 Section 1

This chapter details the setup and calibration of various experimental equipment and procedures for data acquisition and analysis of the research described in this document. Section 3.1 describes the design of a 10.2 cm and a 15.2 cm diameter fluidized bed reactor and the air flow control system. Section 3.2 discusses how the bed materials are selected, prepared, and measured for use in each reactor. Section 3.3 explains the experimental methodology, pressure measurement, and test conditions for the measurement of minimum fluidization velocities in each reactor. Section 3.4 details the equipment and parameters for the X-ray Flow Visualization Facility used to acquire X-ray data for this research. Sections 3.5 and 3.6 describe the procedures for acquiring radiographic and X-ray computed tomographic data, respectively, in addition to calibration methods of those systems for proper imaging. Section 3.7 discusses the gas holdup calculation methodology. Section 3.8 explains the particle tracking methodology and test conditions. Lastly, section 3.9 describes the X-ray Image Processing application functionality developed for analysis of this research.

3.1 System Design

This section describes the fluidization equipment used in this study, focusing on the design of the fluidized bed reactors and air flow control system used for fluidization. First, the nonreactive cold-flow fluidized bed reactors will be described in detail including of their components. Second, a discussion of the air flow control system used for fluidization will describe how air is filtered, flow rates are controlled, and air is used.

3.1.1 Fluidized Bed Reactors

The nonreactive cold-flow fluidized bed reactors used in this study (Fig. 3.1) are designed for side-air injection. Each reactor is made of four main components: the plenum, aeration plate, reactor chamber, and free-board chamber. The reactors are 10.2 cm and 15.2 cm ID hollow axisymmetric columns with 0.6 cm thick walls capable of enduring 620.5 kPa while allowing X-rays to pass through with little to no attenuation affects. They are manufactured from transparent polyacrylic material with 1.27 cm flanges attached to both ends of each columnar section; each component is held together with eight 5.1 cm long, 0.64 cm diameter nylon bolts, and sealed with rubber gaskets cut so as not to interfere with the gas flow through the system.

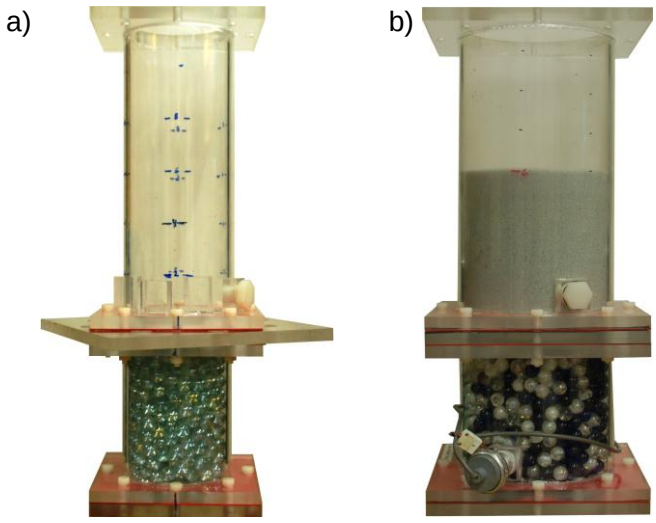

Figure 3.1: Images of the (a) 10.2 cm and (b) 15.2 cm fluidized bed reactor without the freeboard chamber.

Figure 3.2 shows a schematic of each fluidized bed reactor. The plenum, reactor chamber, and free-board chamber are held together by two 16.5 × 16.5 × 1.27 cm flanges attached to the top and bottom of each chamber. Each reactor has 3.18 × 3.18 × 1.2 cm

bosses attached to the outside of the reactor chamber and located above the bottom flange. The 15.2 cm ID reactor has two bosses placed 180° apart, while the 10.2 cm ID reactor has four bosses spaced 90° apart. These bosses are used for fitting new attachments without compromising structural integrity. Each reactor has one boss bored with a 1.91 cm UNF tapped hole located 1.27 cm above the reactor chamber bottom. This hole is fitted with a 1.91 cm UNF nylon Swagelok fitting and O-ring during side-air injection and plugged with a 1.91 cm UNF nylon bolt when side-air injection is not used.

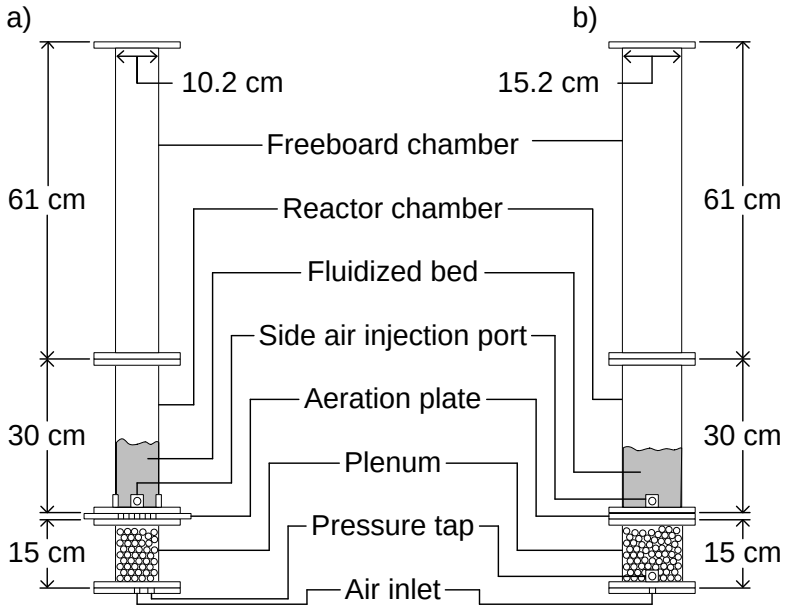

Figure 3.2: Schematic of the (a) 10.2 cm and (b) 15.2 cm fluidized bed reactor.

Between each reactor component is a rubber gasket (Fig. 3.3) to seal the transition from flange to flange. Each gasket has the proper ID hole cut out of its center for the appropriate reactor to ensure even flow of gas between each component. Figure 3.4a shows the aeration plate for the 10.2 cm ID reactor. It is composed of a 1.2 cm thick transparent polyacrylic plate that has 62 uniformly distributed 1 mm diameter holes over a polar grid originating at the plate center, giving it an open area ratio of 0.6 %. The aeration plate for the

15.2 cm ID reactor is shown in Fig. 3.4b. It is a 1.5 mm thick stainless steel plate with 131 uniformly distributed 1 mm diameter holes over a polar grid, giving it an open aera ratio of 0.57 %. A 1.2 cm thick mount held between the plenum and reactor chamber flanges is used to hold the aeration plate in place. The mount has a 15.2 cm diameter hole bored in its middle with a 3.9 mm lip routed out around the hole to contain the aeration plate. To keep bed material from clogging the aeration holes. A 45 mesh screen with openings of 0.04 cm is attached with silicone caulking to the gasket immediately above the respective aeration plate.

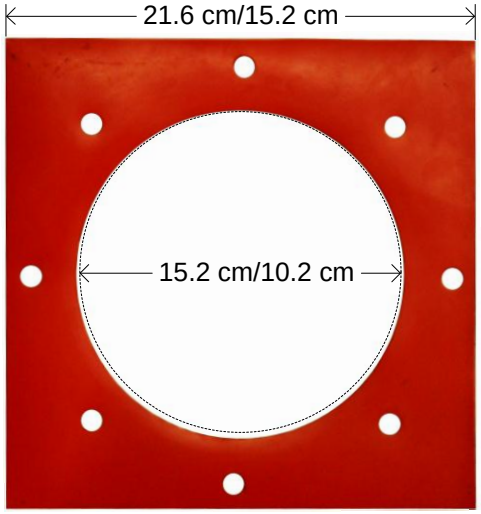

Figure 3.3: Rubber gasket used to seal the fluidized bed reactors.

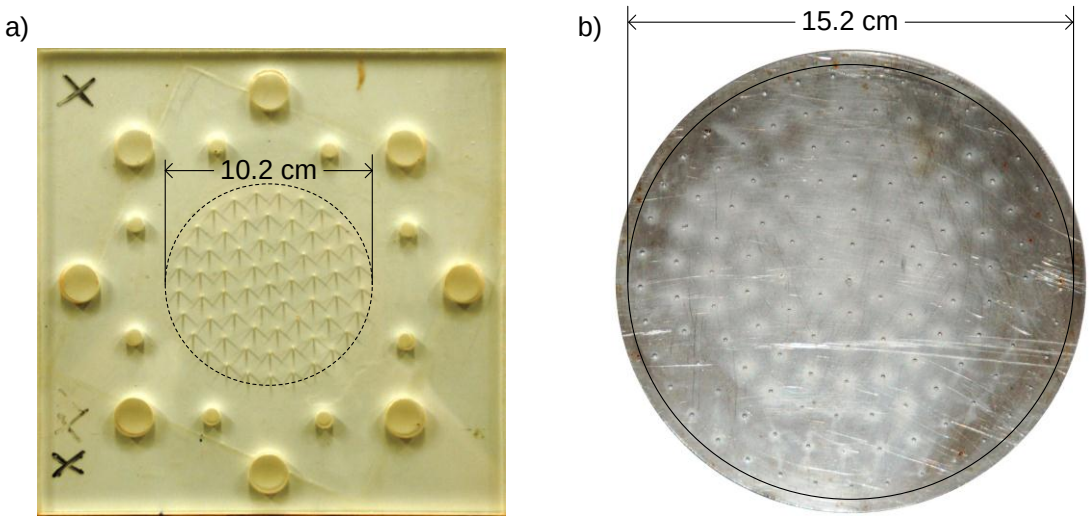

Figure 3.4: Aeration plates used in the (a) 10.2 cm and (b) 15.2 cm fluidized bed reactors.

The 15.2 cm tall plenum for each reactor contains enough 1.27 cm diameter glass marbles to fill it ~1 cm below the aeration plate and are used to provide a uniform pressure distribution of air across the underside of each aeration plate. Each reactor plenum holds a pressure transducer to read pressure for minimum fluidization calculations, which are explained in section 3.3. The transducer is located on the bottom and side of the plenum for the 10.2 cm and 15.2 cm ID reactor, respectively. The air enters the system through a 1.97 cm UNF tapped fitting located in the center of a 1.2 cm thick plate attached to the bottom of each plenum. After flowing through the bed of marbles, the air then passes through the aeration plate into the reactor chamber. With the proper superficial gas velocity, the air will fluidize the bed material contained within. The free-board chamber is included above the reactor chamber to prevent elutriation and to hold any highly excited material due to bubble eruption.

3.1.2 Air Flow Control System

The air flow control system shown in Fig. 3.5 uses compressed air regulated to 620.5 kPa for fluidization and side-air injection. The compressed air is routed through two Wilkerson filters then two main lines: 1) the fluidization line (1.27 cm OD polypropylene tubing) and 2) the side-air injection line (0.95 cm OD polypropylene tubing). Both lines are controlled by a separate stainless steel 0-827.4 kPa pressure regulator valve with filter. Each of these lines separate into one additional high and low flow line each after the regulator. Each of these four lines also contain a gas flow meter with resolutions of ± 2% of full scale: the high flow fluidization line has a 0-1000 Lpm Aalborg GFM671S flow meter; the low flow fluidization line has a 0-200 Lpm Aalborg GFM571 flow meter; the high flow side-air injection line has a 0-100 Lpm Aalborg GFM471 flow meter; and the low flow side-air injection line has a 0-30 Lpm Aalborg GFM371S flow meter. In line before each meter is a ball valve used to activate its respective meter, and air flow through any meter can be adjusted by changing the meter's respective pressure regulator.

The fluidization line contains a 0-1000 Aalborg SMV40 SVF2-A stepper motor control valve between the pressure regulator and the high/low flow separation. It is used to automate control of the fluidization air flow rate by adjusting a needle valve open and closed at varying speeds dependent on voltage resolutions of 125 mV. A National Instruments virtual instrument developed in LabView uses a PID control to regulate the air flow rate by monitoring the 1000 Lpm flow meter and make adjustments to the position of the needle valve as needed.

1) Power
2) Injection system control
3) Fluidization pressure regulator
4) Injector pressure regulator
5) Stepper motor valve
6) 1000 Lpm flow meter
7) 200 Lpm flow meter
8) 100 Lpm flow meter
9) 30 Lpm flow meter

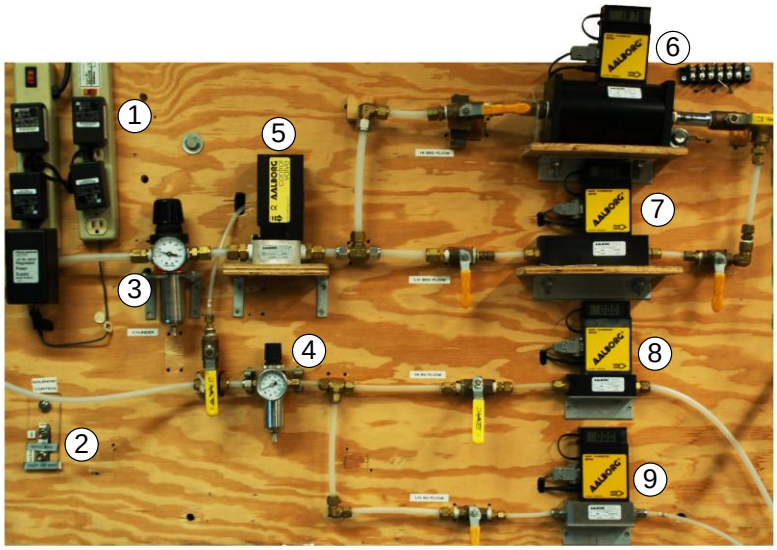

Figure 3.5: Image of the gas control system.

3.2 Bed Material

The fluidization behavior and internal hydrodynamic structure of various bed materials within each reactor are very important to this research. This section will focus on the process of material selection, preparation, and measurement.

3.2.1 Material Selection Criteria

Each of the three bed materials used for this study were based on four criteria: fluidization behavior, size range, density, and aspect ratio. To achieve similar fluidization behavior between different bed materials, Geldart type B particles were used. Low density particles are desirable because of the nature of X-rays, explained in detail in section 2.5. Moreover, uniformly shaped particles are desirable because they fluidize most like conventional fluidized bed systems. The particles were chosen to have 500-600 μm normally distributed diameters because of their availability and representation to materials commonly

used in industrial fluidized bed systems. Furthermore, lower density materials are attractive for visualization of their fluidization behavior.

Glass beads shown in Fig. 3.6a and Fig. 3.6b were chosen as a baseline material because they are well characterized, have a fairly uniform shape, and have similar properties to refractory sand as is commonly used in industrial fluidized bed systems. This material is used as a benchmark for the fluidization behavior of various materials within both fluidized bed reactors. However, glass beads have a fairly high density, ~2600 kg/m^3, and may be problematic with the X-ray imaging techniques used in this study. Consequently, ground walnut shell and crushed corncob (Fig. 3.6c through Fig. 3.6f) have densities of ~1300 kg/m^3 and ~1000 kg/m^3 respectively, and were chosen as comparative bed materials to the glass beads in terms of fluidization behavior and development of hydrodynamic structures. As shown in Fig. 3.6d and Fig. 3.6f, the aspect ratios of the ground walnut shell and crushed corncob are not uniform, yet when compared with the Geldart classification chart (Fig. 3.7) all three materials fall within the Geldart type B classification. As shown in Fig. 3.6, the glass beads are well classified while ground walnut shell and crushed corncob have a range of sizes and shape factors yet still fall within the type B classification.

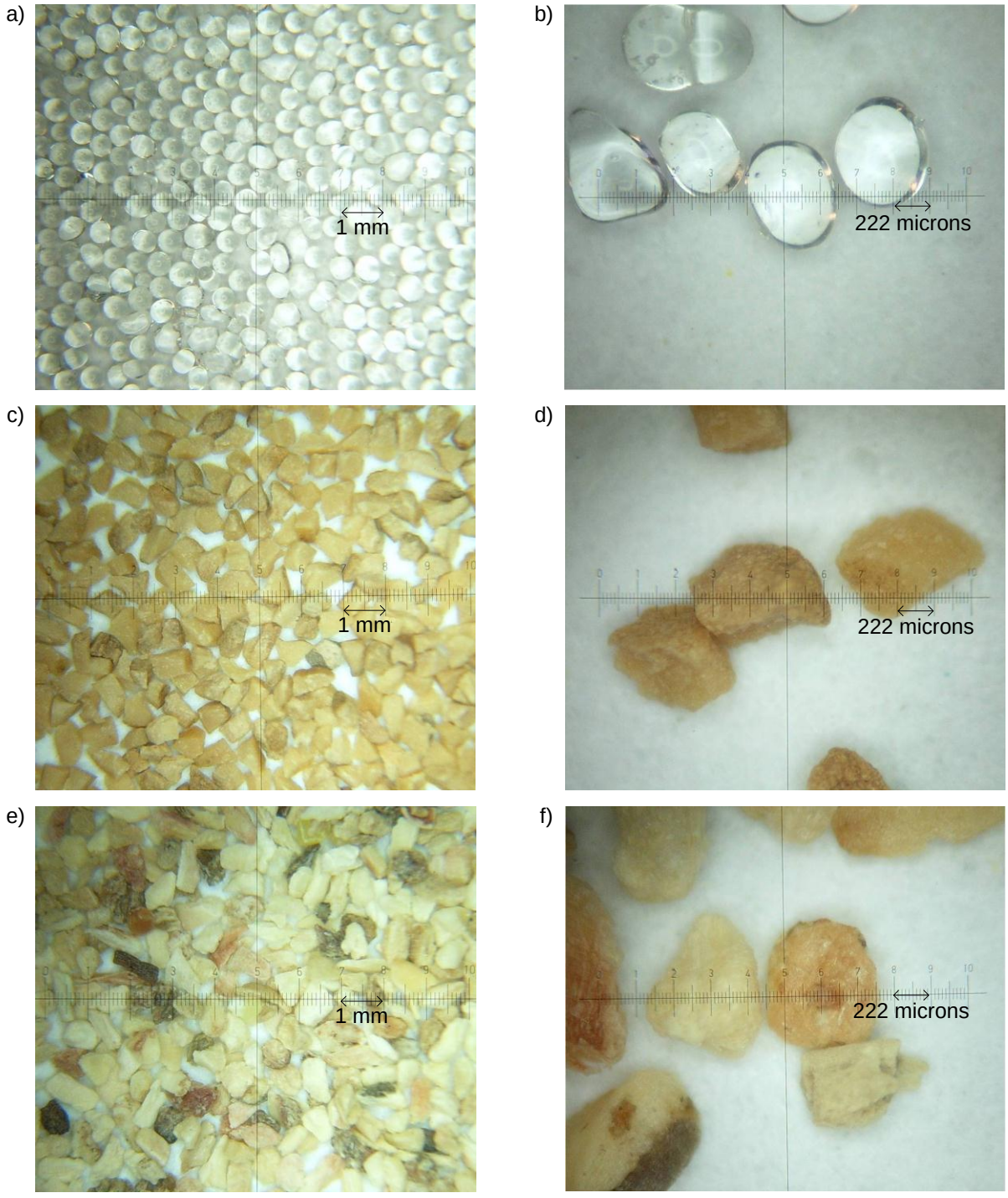

Figure 3.6: Images of the bed materials used in this study: (a) glass beads magnified 10×, (b) glass beads magnified 45×, (c) ground walnut shell magnified 10×, (d) ground walnut shell magnified 45×, (e) crushed corncob magnified 10×, and (f) crushed corncob magnified 45×.

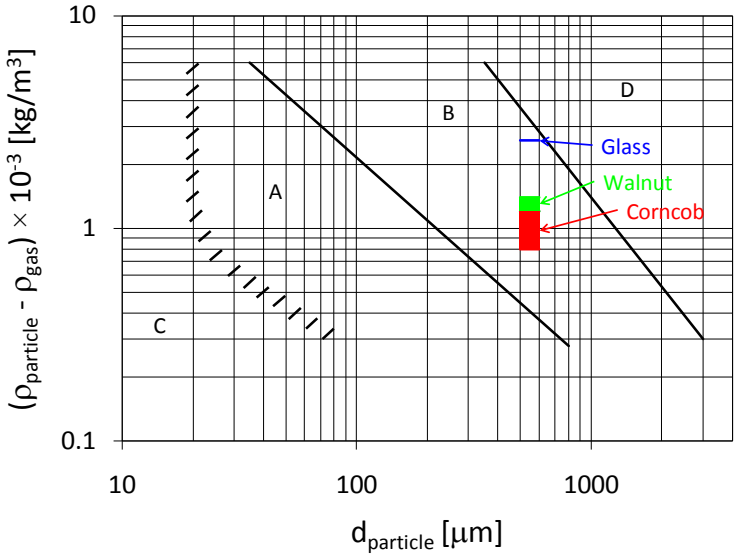

Figure 3.7: Geldart particle classification chart (Geldart 1973).

3.2.2 Material Preparation

Each bed material was prepared with the use of a sieve shaker to attain the desired 500-600 μm size range. This particle size range was assumed to follow a Normal distribution. The particles were sieved multiple times to assure the desired size range. To ensure that the glass beads were free of any dirt or other particulate matter, they were placed in a 200 μm sieve screen and cleaned with running water. The glass beads were then dried with the use of the 15.2 cm ID reactor and air. The ground walnut shell and crushed corncob, being biomass, could not be cleaned this way because water absorption would change their size and density. However, these materials were placed in the 15.2 cm ID reactor and fluidized at a sufficiently high enough superficial gas velocity to elutriate any fines that originate from bed operation.

3.2.3 Material Measurement

To measure the bed weight and bulk density, each material was placed into either reactor at a height of 1 reactor ID, slightly fluidized to remove packing effects, removed from the reactor, and weighed with a Fisher XL–3000 scale. The bulk density, ρ_b, for each bed was calculated by

$$\rho_b = \frac{m_{bed}}{V_{bed}} \tag{3.1}$$

where m_{bed} and V_{bed} are the bed mass and volume, respectively. The bulk void fraction for each bed is calculated from

$$\varepsilon_{g,b} = 1 - \frac{\rho_b}{\rho_p} \tag{3.2}$$

where ρ_p is the particle density as provided by the manufacturer. For the crushed corncob and ground walnut shell, the average of the values shown in Table 3.1 was used for ρ_p. Table 3.1 provides a summary of all bed material properties.

Table 3.1: Material properties

		10.2 cm FB			15.2 cm FB		
		Corncob	**Walnut Shell**	**Glass Beads**	**Corncob**	**Walnut Shell**	**Glass Beads**
D_p	[μm]	500-600	500-600	500-600	500-600	500-600	500-600
ρ_b	[kg/m^3]	392	579	1481	395	567	1496
m_{bed}	[g]	323	477	1220	1098	1576	4158
ρ_p	[kg/m^3]	800-1200	1200-1400	2600	800-1200	1200-1400	2600
$\varepsilon_{g,b}$	[-]	0.61	0.55	0.43	0.61	0.56	0.42

3.3 Minimum Fluidization Velocity

Minimum fluidization is one of the most important properties characterizing the hydrodynamics of bed material in a fluidized bed. The minimum fluidization velocities of

each material used in this research was the basis for determining the particular flow rates studied. This section discusses the methodology in determining the minimum fluidization velocity; how pressure measurements are made; and the relationship between various test conditions and the minimum fluidization velocity for each material in both reactors.

3.3.1 Methodology

Minimum fluidization velocity is generally determined experimentally because many of the calculable parameters can only be estimated (Davidson and Harrison 1963). According to Davidson and Harrison (1963), Felipe and Rocha (2007), and Hilal et al. (2001), bed packing effects cause a hysteresis affect in the bed when a piece-wise increase of superficial gas velocity is used to find the minimum fluidization velocity. Consequently, pressure drop across the bed is usually measured as the gas flow rate is decreased from fully fluidized to completely unfluidized. Minimum fluidization is identified by the transition from a fixed bed to a bubbling bed. The difference is that a fixed bed is identified by a linearly increasing pressure drop with increasing superficial gas velocity, whereas in a bubbling bed the pressure drop is constant with increasing superficial velocity. Therefore, the superficial gas velocity associated with the transition from linearly increasing to constant pressure drop with increasing superficial gas velocity is the minimum fluidization velocity.

3.3.2 Pressure Measurement

The minimum fluidization velocity was found for each bed material in both reactors in the same manor. The material was fluidized at a volumetric air flow rate slightly higher than the minimum fluidization point (200 Lpm and 300 Lpm for the 10.2 cm and 15.2 cm ID

reactor, respectively). After coming to quasi-steady state flow rate, the pressure and flow rate were acquired over a 5 second interval, averaged, and recorded using a National Instruments DAQ system. The air flow was then decreased by 5 Lpm and once a quasi-steady state was reached again, this process was repeated until the flow rate was 0 Lpm, at which time the test was completed. Ten tests were performed for each material in each reactor to acquire a good statistical average.

The aeration plate and marbles in the plenum create a pressure drop within the reactor. This was determined using the prior process without bed material present. Again, ten tests were performed for each reactor to get a good statistical average. This data was then subtracted from the full bed pressure drop data and plotted against the superficial gas velocity in the bed. As schematically shown in Fig. 3.8, minimum fluidization is defined as the point where the bed pressure drop becomes constant with increasing superficial gas velocity.

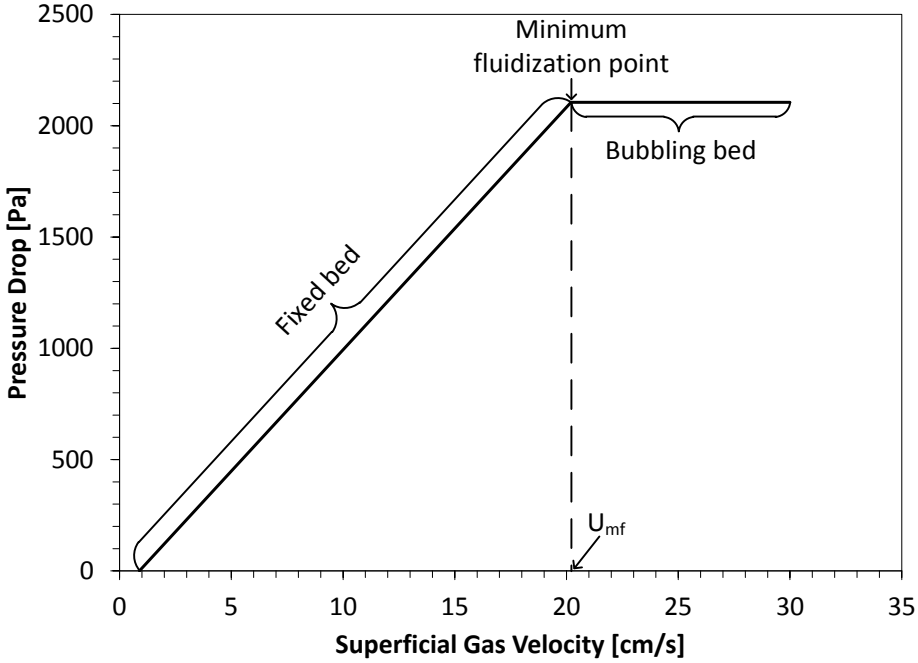

Figure 3.8: Minimum fluidization velocity identified by plotting the pressure drop as a function of superficial gas velocity.

3.3.3 Test Conditions

Each bed material was fluidized over 4 different superficial gas velocities for each reactor: U_g = 1.25, 1.5, 1.75, and $2U_{mf}$. In conjunction with these flow conditions, 5 side-air flow rates were tested as well: Q_s = 0, 0.05, 0.1, 0.15, $0.2Q_{mf}$, where Q_{mf} refers to the volumetric flow rate at U_{mf}.

3.4 X-ray Flow Visualization (XFloViz) Facility

This section discusses the X-ray image acquisition equipment and settings used in this study. The X-ray source used is a liquid cooled LORAD LPX200 portable X-ray system (Fig. 3.9). The source produces X-rays by electron bombardment of a beryllium window in the source head that emitted a conical beam 60° wide in the horizontal direction and 40° wide in the vertical direction. The conical beam is collimated by a lead shield surrounding each source. The voltage and current are adjusted from 10 to 200 keV and 0.1 to 10.0 mA, respectively, for a maximum power output of 900 W. Depending on the attenuation characteristics of the OOI being visualized, a combination of metallic filters is used to reduce low energy radiation. Moreover, the power settings must be adjusted with both the voltage and current for the best contrast resolution of the image, which is also dependent on the OOI's attenuation characteristics. For example, higher density materials require a higher power setting.

1) Slew ring
2) CsI phosphor screen/CCD
3) Intensifier/CCD
4) 15.24 cm fluidized bed
5) Lead shutters
6) X-ray sources
7) Test stand

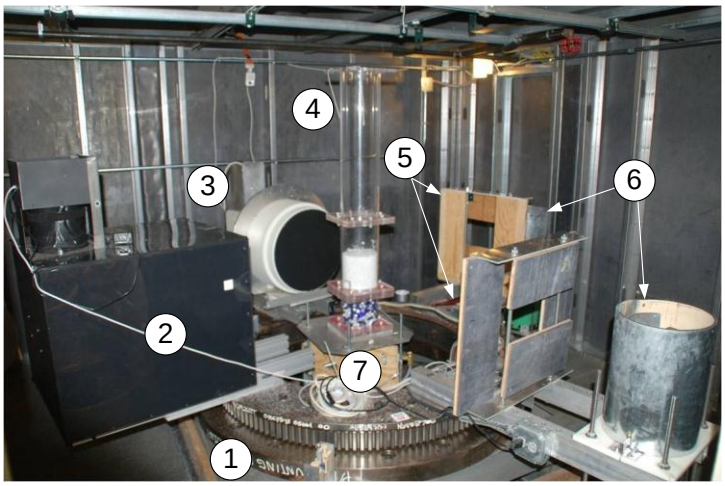

Figure 3.9: Image of the X-ray equipment.

The system has two different types of detectors: 1) two intensifier/CCD pairs or 2) a single CsI phosphorous screen/CCD pair. Only the CsI phosphorous screen/CCD pair was used in this study for X-ray CT image acquisition because it has a higher spatial resolution than the intensifiers. The CCD/detector pair consists of a 44×44 cm CsI scintillating screen producing an image that is captured by a 50 mm Nikon lens attached to an Apogee Alta U9 camera with a thermoelectrically cooled 3072×2048 active pixel CCD matrix. The CCD has a method of combining pixels together into "effective pixel" clusters affecting image resolution called binning, which ranges from 1×1, 1×2, 1×3, 2×2, 2×3, 2×4, 3×3, 4×4, 5×5, 6×6, 7×7, and 8×8. The binning used in this study was 4×4. The CCD thermoelectric cooler can be set to various temperatures and exposure times can be changed to reduce noise in the image.

The detector/CCD pair sits opposite an X-ray source on adjustable rails and can be moved towards or away from the source. This action magnifies the image of the OOI when acquiring data; therefore, moving the detector towards the OOI reduces magnification and moving it away increases magnification. Each source/detector pair is attached to a 1 m ID

slew ring that can completely rotate around the OOI with the aid of a stepper motor controlled by a computer. The OOI sits on a test stand in the center of the slew ring and is adjusted vertically via a 910 kg lift system. The vertical range of the lift is 2.75 m; however, this capability is not used in this study.

Figure 3.10 shows that all equipment in the facility sits inside a lead lined imaging room located 3.7 m above the lab floor that is accessible by a series of catwalks and stairs. The lift system is located under the imaging room and is also enclosed with lead lined walls. To ensure safe operation of this system, all entrances to the imaging facility have emergency shutoff controls and are regularly tested for radiation leakage by Iowa State University's Department of Environmental Health and Safety. Additional details of the facility have been reviewed by Hubers (2005) and Striegel (2005)

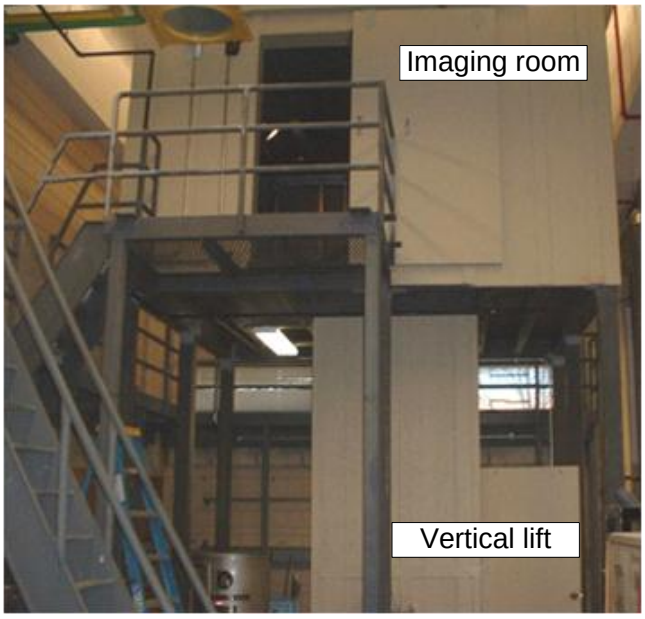

Figure 3.10: Exterior view of the imaging room and lift enclosure.

3.4.1 Parameters

X-ray parameters are adjusted to optimize image contrast, X-ray penetration, and image resolution, while minimizing image noise. These parameters are dependent on the OOI being imaged and the method of visualization. The voltage and current of the X-ray sources control the image contrast and penetration respectively. Image resolution is adjusted by changing the CCD binning options and image noise is minimized by applying various calibrations to the CCD system.

3.5 Radiography

An X-ray radiograph is the basis of all X-ray visualization techniques used in this study. This section outlines the procedures and calibration methods for proper acquisition of radiographs with the particular equipment describe in section 3.4.

3.5.1 Procedure

To begin taking radiographic images, the X-ray source being used must first be pre-warmed. To avoid burning an image into the detectors, the lead shutters covering each X-ray source are shut prior to the pre-warm. During the pre-warm, the X-ray source is automatically ramped up to 900 W slowly by the control box and the CCD is cooled to a temperature chosen by the operator. The pre-warm takes place over a predetermined time that is dependent on the last time the source was used. Once the pre-warm and CCD cooling is finished, the X-ray source is powered down, the lead shutters are opened, and the OOI is placed on the stand in the imaging room. Next, the X-ray source is powered on again and the

X-ray power settings are adjusted for the best image contrast resolution. The camera bin settings are then adjusted depending on the picture size needed for analysis.

Finding the X-ray source power settings appropriate for the OOI is very important for capturing quality data and is typically accomplished through trial and error. The detector's phosphorous screen can become saturated if the incident X-rays are too energetic leading to a loss in image resolution and decreases both the quantitative and qualitative data. Saturation occurs when the intensity of most pixels in the center of a radiograph reach the maximum allowed value for a 16-bit spatial resolution of 65535. Conversely, a loss of resolution can also occur if the X-ray power is too small. Hence, attention to detail is required for high quality images. Using custom software called X-ray Image Processor (XRIP), an image of the OOI is acquired and analyzed to begin the pre-calibration process. This process determines if the power settings should be readjusted; if metallic filters should be used with the X-ray source; and whether the detector should be moved towards or away from the OOI. Once these steps are finalized, the OOI is taken out of the imaging region, and the system is ready for calibration.

After completing the calibrations, the scintillation screen must be cleared of ghost images from prior image acquisitions. A ghost image is an image that has been retained in the screen by the action of shadowing. What occurs is that areas of the screen that receive more X-ray energy fluoresce more and tend to retain that energy over long periods of time. To account for ghosting, the detector must be pre-exposed with the chosen power settings for ~15 minutes; this assures that all portions of the screen fluoresce homogeneously. After calibrations are acquired, the OOI is placed back in the imaging region atop the test stand and imaging can begin. For this study, each fluidized bed reactor is centered in the imaging

region on the test stand; the test stand height is adjusted so that the top of the aeration plate is at the bottom of the images; and the reactor is clamped down and leveled vertically.

3.5.2 Pixel Normalization Calibration

CCDs are manufactured with specific tolerances, which allow for differences in each CCD matrix. These differences permit a non-uniform signal response across the matrix when acquiring images. To account for the non-uniformity, linear pixel normalization is applied by XRIP to each image acquired after calibration. This is done by using the intensity values of a dark (I_{dark}), light (I_{light}), averaged (I_{ave}) dark and light, and an uncalibrated (I_{image}) radiographic image to give a new calibrated (I_{new}) image, using the following equation:

$$I_{new} = I_{image} + \left(I_{image} - I_{dark}\right)\left(\frac{I_{ave}}{I_{light} - I_{dark}}\right) \tag{3.3}$$

where I is the local pixel intensity value for the appropriate image indicated by each subscript. Striegel (2005) describes this algorithm in more detail.

The acquisition of the light and dark calibration images is done prior to the capture of any test images. Moreover, the imaging region must be free of any obstructions so that the signal response across the entire CCD matrix can be analyzed using the entire spectrum of the X-ray band incident on the intensifier. First, the dark image is acquired when the X-ray source is powered off. Next, the light image is acquired when the X-ray source power is high enough to nearly saturate the detector.

3.6 X-ray Computed Tomography

The purpose for obtaining and reconstructing X-ray CT images in this study is for qualitative and quantitative analysis of time-average gas holdup in each bed material and reactor. This section discusses the procedures and calibration methods for proper acquisition of X-ray CTs with the particular equipment describe in section 3.4. Unlike radiographs, X-ray CT images must be calibrated and, if needed, corrected before being written to disk for storage.

3.6.1 Procedure

The procedure of acquiring an X-ray CT is more involved than for radiographs because instead of just analyzing the radiographs, these images are convolved into 3D volumes from the original 2D images. More preparation and calibration steps are required due to the higher sensitivity of the detector and how the images are both pre- and post-processed. This section discusses how to prepare for and acquire the files used for X-ray CT reconstruction and the reconstruction process of X-ray CTs.

3.6.1.1 X-ray CT Preparation and Acquisition

The start-up and preparation procedure for taking an X-ray CT is virtually the same as for acquiring a radiograph and is described in section 3.5.1; however, because of the increased complexity of X-ray CT acquisition more calibration steps are required. After calibrations are completed, the OOI is setup in the imaging room and an X-ray CT is started. Unlike radiograph acquisition, X-ray CT acquisition and calibration is not controlled by XRIP, this application is called PS_CT and was developed by Iowa State University's Center

for Nondestructive Evaluation (CNDE). "Instructive use of PS_CT is discussed in detail by Strigel (2005). The settings for X-ray CT acquisition are summarized in Table 3.2.

Table 3.2: X-ray CT experimental parameters

		10.2 cm FB			15.2 cm FB		
		Corncob	Walnut Shell	Glass Beads	Corncob	Walnut Shell	Glass Beads
Voltage	**[keV]**	130	130	150	139	144	160
Current	**[mA]**	3.2	3.2	3.5	3.9	2.8	4.5
Filters	**[-]**	1 Al, 1Cu	1 Al, 1Cu	1 Al, 2Cu	1 Al, 1Cu	1 Al, 1Cu	1 Al, 2Cu
Binning	**[-]**	4×4	4×4	4×4	4×4	4×4	4×4
Detector Distance	**[-]**	172	172	172	172	172	172

3.6.1.2 X-ray CT Reconstruction

X-ray CTs are mathematical reconstructions of individual ray-sums taken at specified angular locations completely around the OOI. These ray-sums are horizontal lines of pixel intensity values captured by the CCD matrix. As the detector traverses around the OOI and captures images, the ray-sums are digitized and stored in files called sinograms. A single sinogram holds the ray-sum data for 10 slices of which each slice is the ray-sum data for a single horizontal plane through the OOI. For example, for the top 10 slices of the X-ray CT with data acquired at every degree for a total of 360°, the sinogram file would hold 3600 ray-sums. However, only the ray-sums that make a complete horizontal slice are put together; therefore, all ray-sum acquisitions for row one of the CCD matrix are stored together in the same image. A representation of how these ray-sums are stored is shown in Fig. 3.11. Figure 3.12 shows the compilation of two slices within the sinogram files at slice 0 (top of X-ray CT) and 250 (middle of X-ray CT) top and bottom images respectively. It can be seen that the OOI is curved in an 'S' shape; however, all 360 ray-sums for a single slice are stored together, making it appear distorted. Meaning that the 'S' curve just indicates that the OOI

was not perfectly centered in the imaging region. Moreover, the number of slices gives the height in pixels of a reconstructed X-ray CT, which is adjusted by the CCD binning options.

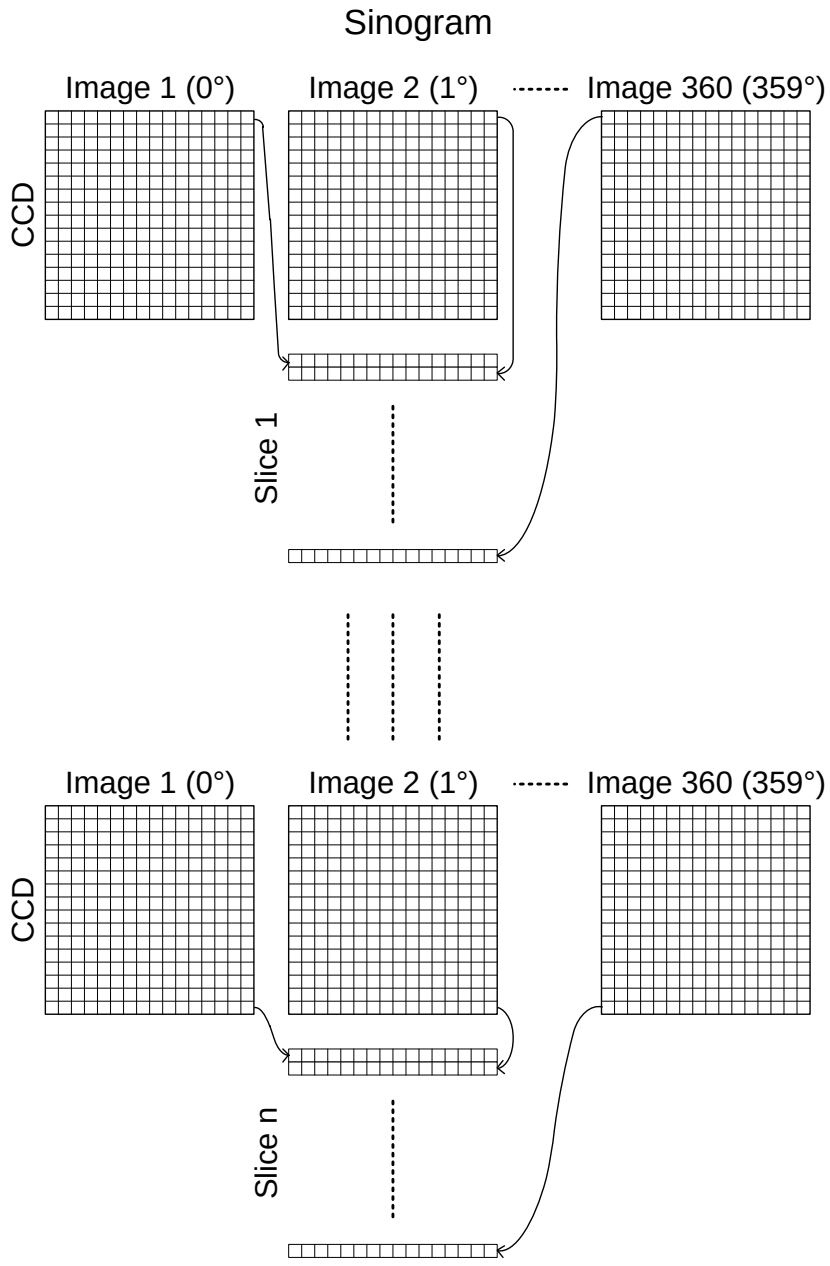

Figure 3.11: Diagram of ray-sum storage in sinogram files.

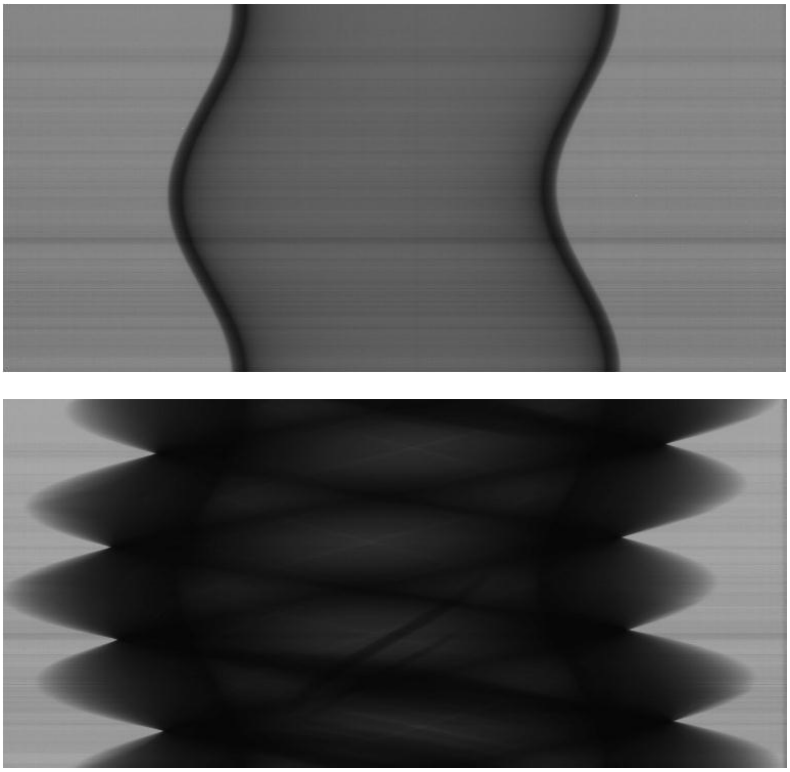

Figure 3.12: Images of sinogram slices at slice 0 (top) and 250 (bottom).

Other artifacts are found in Fig. 3.12 but are difficult to visualize in 8-bit gray scale when printed, such as, dark horizontal banding from top to bottom and light vertical banding at the left and right edges of the image in both the 0 and 250 slice. Note that the dark banding occurs at the same locations and over the same amount of area in both slices. This shows that during image capture at these angular locations the source voltage and current from the control box fluctuated. Although, the power settings should remain constant, the system is not ideal. These fluctuations can be accounted for after image acquisition through a normalization algorithm. It was found that these artifacts did not reduce the quality of reconstructed X-ray CTs and, therefore, normalization was not implemented.

The vertical light banding arises from the detector's scintillation screen. The screen is circular and attached to the inside face of a cubic enclosure; therefore, the camera captures

the corners of the inside square face at different intensities because this area is not covered by the circular screen. The light from these corners is reflected off the inside walls of the detector due to the florescence of the screen. The light banding cannot be accounted for when reconstructing the X-ray CT and, again, these artifacts did not reduce the quality of reconstructed X-ray CTs.

Before the sinograms can be used to reconstruct an X-ray CT, the center of rotation (COR) of the X-ray CT must be found. Although this seems redundant, it is important because the detector alignment can vary slightly depending on its radial location from the center of the imaging region. If the rails on which the detector sits are not perfectly aligned with the X-ray source or the rails are not perfectly level, then the X-ray CT's COR will be askew with respect to the axis of rotation of the system. This creates a double image within the reconstructed X-ray CT because the ray-sum assemblage will overlap slightly making it impossible for quantitative analysis. Finding the COR of an X-ray CT is done with the use of an application developed by CNDE called Recon 2-D. Using this application, a process of iteratively reconstructing both the top and bottom slices with various COR values will eventually yield a clear image. The COR value for both the top and bottom slices is then used for a full reconstruction of the X-ray CT.

X-ray CTs are reconstructed via filtered back-projection by interpolation within the frequency domain and a weighing function. This method essentially takes a ray-sum, as pictured in Fig. 3.13a, and stretches the ends while compressing the center to form a pie-piece shape like that shown in Fig. 3.13b. This is repeated for all ray-sums and compiled together into a single slice (Fig. 3.13c). Then all the slices are stacked on top of one another until an entire 3D X-ray CT is formed. Because this method is calculation intensive, all

sinograms are transferred to the CNDE computation center. A network of 64 CPU nodes performs the calculations in parallel, asynchronously and is transferred back to the XFloVis facility upon completion.

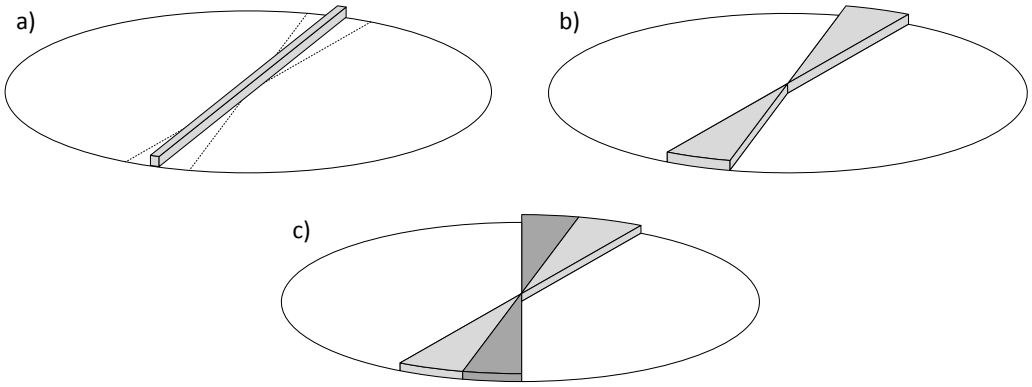

Figure 3.13: Diagram of how an X-ray CT is reconstructed. A ray-sum (a) is stretched on the ends and compressed in the center to make pie shaped pieces (b) that are put together to form larger pie pieces (c) until an entire slice is compiled.

3.6.2 Calibrations for X-ray CT Imaging

X-ray CT reconstructions are particularly disposed to inaccuracies in the reconstructed data due to the mathematical functions involved. The convolution functions used to transform the pixel intensity values from signal space to frequency space cause artifacts to be generated. These artifacts are due to beam hardening and interface density changes. Beam hardening is caused by the average radiation energy increasing as the X-rays propagate through an object because the low energy photons are preferentially absorbed (ASTM 1997). It results in a false radial density gradient that causes abnormally low values in the center of a uniform object and high values at the edges. Interface density changes or edge artifacts come from sharp changes in signal level resulting in streaks in the X-ray CT due to mathematical relations in the reconstruction algorithm. This section will discuss the

four major calibration methods used to reconstruct a proper X-ray CT generated in the XFloViz facility: 1) pixel, 2) normalization, 3) beam hardening, and 4) aspect ratio correction.

3.6.2.1 Pixel Normalization

The pixel normalization process discussed here is virtually the same as that in section 3.5.2.2; the only difference is that this calibration is applied to the images as they are taken and stored to disk.

3.6.2.2 Beam Hardening

During reconstruction of X-ray CTs, an artifact called beam hardening is often present and must be removed for accurate density information (Ramakrishna, Muralidhar et al. 2006). Beam hardening is an effect of the polyenergetic nature of X-rays; the linear X-ray attenuation coefficient, μ, for low energy X-rays is typically much larger than μ for high energy X-rays in most materials (Ramakrishna, Muralidhar et al. 2006). Therefore, the lower energy X-rays are preferentially attenuated in high density materials, causing portions of the X-ray CT to have false signals of lower density.

The result of beam hardening is shown in Fig. 3.14, where brighter regions represent lower density and darker regions represent higher density, although the actual object is of uniform density. A corrected image in Fig. 3.14b, shows a much more uniform intensity profile. The correction is applied to all sinogram data before the image is reconstructed, which paves the way for possible quantitative results of density variation supplied by X-ray

CT analysis of the OOI. Another benefit is that it can make the surfaces of the OOI more easily identifiable.

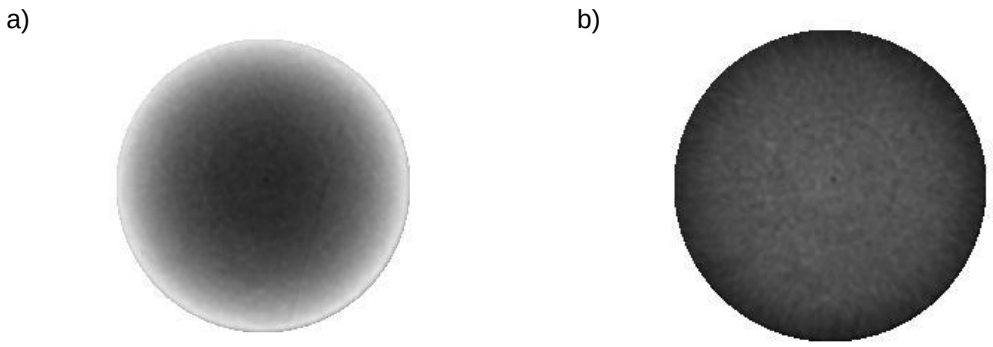

Figure 3.14: X-ray CT images of a uniform static glass bead bed inside of the 15.2 cm fluidized bed. Image (a) has not been corrected for beam hardening and (b) has been.

Beam hardening corrections are completed in two steps: first, by filtering low energy X-rays emitted from the source with two 0.6 mm thick copper plates and one 1.5 mm thick aluminum plate placed over the X-ray source window; and second, by analyzing the X-ray attenuation of the same material at varying thicknesses, which yields a fifth-order polynomial curve fit. For this study, a beam hardening correction is applied only to the glass beads because beam hardening in the ground walnut shell and crushed corncob is assumed to be negligible.

The second correction method applies an "effective μ" calibration to the raw X-ray CT data. The Beer-Lambert law,

$$I=I_0e^{-\mu T} \tag{3.4}$$

governs the transmission of X-ray energy through a material where the intensity of the transmitted X-ray energy incident on the detector, I, is a function of the X-ray intensity incident on the OOI, I_0, the linear attenuation coefficient, μ, and the thickness of the object,

T. The linear attenuation coefficient is a product of the mass attenuation coefficient and density; therefore, for a material with an assumed constant density, the attenuation coefficient is only a function of density. Assuming air has negligible attenuation, I_0 may also be thought of as the intensity of the X-ray energy that does not pass through the object.

Rearranging Eq. (3.4) gives,

$$\ln\left(I/I_0\right)=-\mu T \tag{3.5}$$

and by plotting $\ln(I/I_0)$ verses T, a linear line implies the absence of beam-hardening. A tangent line at small T, S(T), can be created using the actual $\ln(I/I_0)$ versus T data. This resembles the linear attenuation coefficient in an ideal scenario without beam hardening. The actual $\ln(I/I_0)$ versus T data are then fit to a fifth-order polynomial to produce a curve P(T). The subtraction of the curve-fit from the tangent line yields the effective μ correction factor, F(T),

$$F\left(T\right)=S\left(T\right)-P\left(T\right) \tag{3.6}$$

The correction factor can be plotted against $\ln(I/I_0)$ to produce another fifth-order polynomial curve fit, F(T). The F(T) curve-fit is then applied to the raw X-ray CT data to remove beam hardening effects. Since the correction factor is dependent on the tangent line S(T), identification of the best tangent line is an iterative process.

The "effective μ" calculation for the glass bead bed material was completed by analyzing the X-ray attenuation characteristics through given thicknesses of DSB soda-lime plate glass. A glass wedge of 24, 10.2 cm wide plates of varying lengths are stacked making an array of 12 glass thicknesses (Fig. 3.15), which gives good attenuation information regarding both the small and large thicknesses.

Figure 3.15: Images of the glass plate wedge used to find beam hardening parameter for the glass bead bed.

A radiograph of the wedge using the same power settings as the X-ray CTs of the glass bead fluidized bed is taken and analyzed with XRIP to find the average intensity value for the varying thicknesses of the wedge and air surrounding the wedge. These values are then used to determine the correction factor, F(T), that is applied to the X-ray CT sinograms using SAS Beam Hardening, an application developed by CNDE.

3.6.2.3 Aspect Ratio Correction

The CCD matrix used in this study to acquire X-ray CTs has 3072×2048 active pixels. Reconstructed X-ray CTs using the algorithm provided by CNDE returns cubic volume files. This algorithm does not take the non-uniform dimensionality of the CCD matrix into account. Therefore, the reconstructed X-ray CTs appear compressed in the horizontal x- and y-directions. For this study, all data were acquired at 4×4 binning utilizing 768×512 active pixels, yet when reconstructed, the X-ray CTs were 512×512. When correcting for this, all qualitative images were either vertically shrunk by 66.7% or horizontally stretched 150% using XRIP. A sample aspect ratio correction is shown in Fig. 3.16.

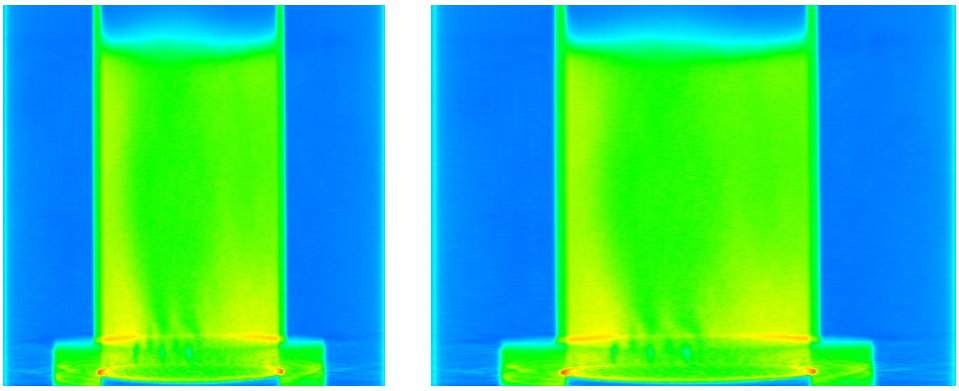

Figure 3.16: Images of an uncorrected (left) X-ray CT aspect ratio and corrected (right) X-ray CT aspect ratio with false color applied.

3.7 Gas Holdup

The determination of gas holdup (gas void fraction) is a major component of this research. This section will describe the methodology for determining the gas holdup for each experiment using X-ray CT data acquired in the X-ray Flow Visualization Facility.

3.7.1 Gas Holdup Derivation

Local gas holdup, ε_g, is determined from (Hammer, Johansen et al. 2006):

$$\varepsilon_g = \frac{\mu - \mu_p}{\mu_g - \mu_p} = \frac{I - I_p}{I_g - I_p} \tag{3.7}$$

were the local X-ray attenuation is μ for a dynamic bed, μ_p for a solid particle, and μ_g for the gas. This assumes that the local X-ray attenuation is proportional to the X-ray CT intensity values for the dynamic bed (I), particle (I_p), and gas (I_g). Unfortunately, the intensity of a single solid particle cannot be found through X-ray techniques because of resolution issues. However, by solving for I_p in the bulk phase gas holdup:

$$\varepsilon_{g,b} = \frac{\mu_b - \mu_p}{\mu_g - \mu_p} = \frac{I_b - I_p}{I_g - I_p} \tag{3.8}$$

and substituting it into Eq. (3.7), ε_g can be determined:

$$\varepsilon_g = \frac{I - I_b\left(I_g - I\right)\varepsilon_{g,b}}{I_g - I_b} \tag{3.9}$$

where I_b is the intensity of a fixed bulk bed. Assuming the static bulk bed is homogeneous, the bulk phase gas holdup of a fixed bed is constant and known,

$$\varepsilon_{g,b} = 1 - \frac{\rho_b}{\rho_p} \tag{3.10}$$

where ρ_b is the bulk density, and ρ_p is the particle density.

3.7.2 Calculation of Gas Holdup from X-ray CTs

Finding local time-average gas holdup from an X-ray CT of a single dynamic bed experiment requires three different X-ray CT files: 1) the X-ray CT of the dynamic bed (flow), 2) an X-ray CT of a static bed of the same material (bulk), and 3) an X-ray CT of an empty bed (gas). These files are used in Eq. (3.9) to generate a new 3D file that contains the local time-average gas holdup. Note that all values in Eq. (3.9), except for $\varepsilon_{g,b}$, have unique time-average values at every voxel (3D pixel), which are 450 μm on a side, within the imaging domain. The ε_g calculation error is estimated to be approximately ±2%.

The newly generated 3D ε_g maps can be sliced into planes as shown in Fig. 3.17, where x- and y-slices are vertical, cutting the reactor axially, and z-slices are horizontal, cutting the reactor radially. This slicing process takes place within a ROI that is inscribed within the 3D ε_g file. The ROI for all 3D ε_g files analyzed in this study encapsulate only the space containing the fluidized bed, this excludes the reactor walls and aeration plate.

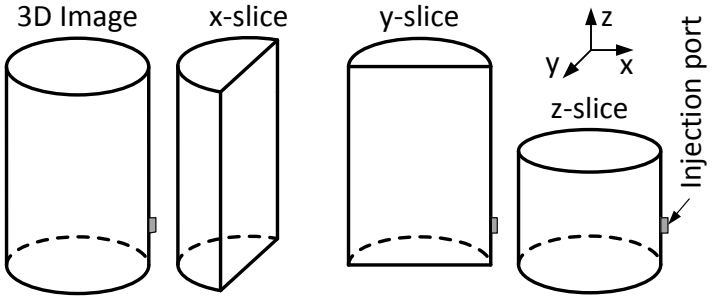

Figure 3.17: CT imaging planes.

3.7.3 Calculating Average Annular Gas Holdup from X-ray CTs

2D surface maps of the averaged local time-average annular gas holdup values, $\varepsilon_{g,r}$, are calculated by averaging all voxels in each annuli at all heights within the bed. Defining which voxels fall within particular annuli is determined by rounding the length of the ray connecting the center of the voxel of interest to the ROI center (bed center) to the nearest integer. Once, a 2D matrix of $\varepsilon_{g,r}$ values is created defining both the height and radii of each value within the bed, the data is smoothed both in the vertical and horizontal directions at each height and radii to reduce noise. All points in the 2D surface map represent the average ε_g value of an annulus at a particular height and radius. This is completed by inscribing concentric circles on each z-slice of the 3D ε_g maps centered on the reactor center and extending to the reactor walls, see Fig. 3.18. In Fig. 3.18, a schematic of the reactor walls enclosing the perforated aeration plate of the 15.2 cm reactor is shown. The aeration plate for the 10.2 cm reactor has fewer concentric aeration circles. Note how the perforations tend to fall on certain annuli, allowing well-defined averages for the aeration jets in the $\varepsilon_{g,r}$ surface maps.

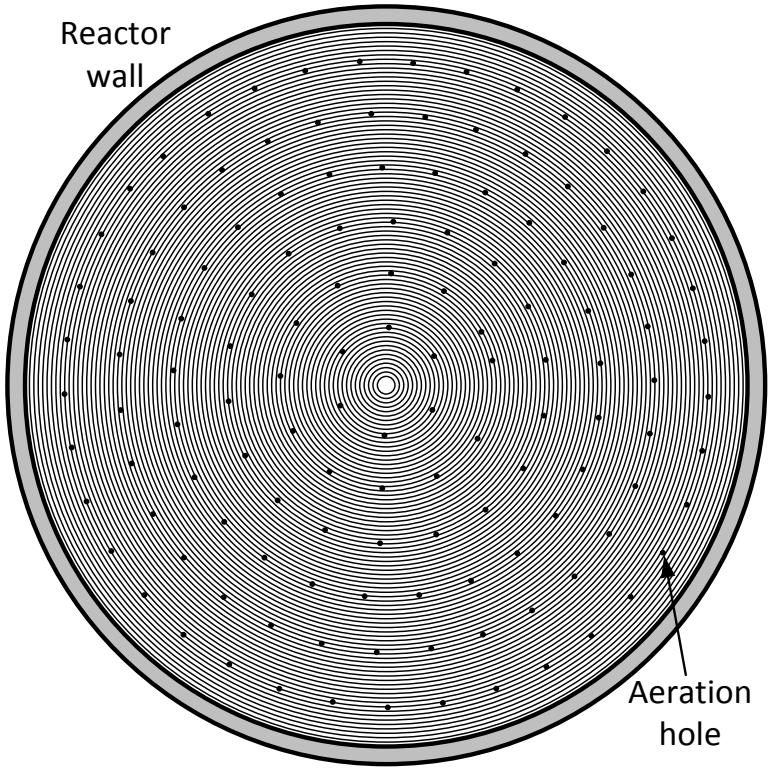

Figure 3.18: Schematic of annuli inscribed inside of the 15.2 cm reactor.

3.7.4 Test Conditions

The chosen test conditions for this study mirror those of the minimum fluidization tests. Each bed material is fluidized over four different superficial gas velocities for each reactor: U_g = 1.25, 1.5, 1.75, and $2U_{mf}$. In conjunction, 5 side-air flow rates were tested at each U_g: Q_s = 0, 0.05, 0.1, 0.15, $0.2Q_{mf}$. Note that all data obtained with the 10.2 cm fluidized bed reactor were generated by Fanka (2008).

CHAPTER 4 THE REPEATABILITY AND UNIFORMITY OF 3D FLUIDIZED BEDS[1]

Equation Chapter 4 Section 1

4.1 Abstract

Hydrodynamic characterization of fluidized beds is vital to many industrial processes, including the production of biofuels, pharmaceuticals, and numerous petroleum products. Local time-average phase fractions can be quantified in these multiphase three-dimensional systems using X-ray computed tomography (CT). This paper describes repeatability and uniformity measurements in a 3D 15.2 cm diameter cold flow fluidized bed using CT imaging to quantify gas holdup. Two different bed materials and a range of superficial gas velocities are investigated. Five tests over different days are completed to show repeatability for each test condition. Highly repeatable local time-average gas holdup is recorded at various locations within the bed for each material over all flow conditions. Uniformity is determined by analyzing the local time-average gas holdup at 12 azimuthal locations for both materials and various flow conditions. Uniform axi-symmetric fluidization is observed for each material and U_g when the bed height is greater than h = 0.25D, where the effects of individual aeration holes dissipate.

4.2 Introduction

Fluidization is the act of passing a gas vertically through a bed of solid granular material at velocities great enough so that the bed will achieve fluid-like properties. To

[1] Drake, J. B. and T. J. Heindel (2011). "The repeatability and uniformity of 3D fluidized beds." Powder Technology **213**(1-3): 148-154.

achieve fluidization, the particle drag force must counterbalance the gravity force; the fluid velocity at which this first occurs is defined as the minimum fluidization velocity (Krishna, Van Baten et al. 1998). At this point, the bulk bed behaves much like a fluid. Fluidized beds reveal many fluid-like characteristics, such as: light objects float; the upper surface stays horizontal when tipped; waves can be generated on the surface; sound propagates through the bed; and the viscosity of a fluidized bed has been likened to that of motor oil (Brown 1997).

A fluidized bed reactor is the vessel in which a particulate bed can be fluidized. These reactors experience low pressure drops, have uniform temperature distributions, can attain excellent gas-solid contacting for high heat and/or mass transfer rates, can accommodate a wide range of particle properties, and have the capability of handling limited liquid quantities (Grace 2006). Fluidized bed reactors are key components in the manufacture of various intermediate and end-user consumer products (Dudukovic, Larachi et al. 1999), such as gaseous and liquid fuels, commodity chemicals, and pharmaceuticals (Zhu and Cheng 2006). Moreover, fluidized bed reactors are quickly becoming the standard technology for small scale power generation (less than 25 MW) that is widely used in Europe, North America, and China among other countries (Oka 2004) for processes such as coal, biomass, and waste combustion, pyrolysis, and gasification. Furthermore, concerns about global climate change due to increasing carbon outputs from power generation, specifically the burning of fossil fuels, have also increased the popularity of fluidized bed gasifiers to process biomass into both transportation fuels and electricity generation (Cui and Grace 2007).

Although fluidized beds are used in industry, an understanding of the internal hydrodynamic bed structures is still somewhat lacking. This creates problems when scaling

up from laboratory to industrial scales. The optical thickness of the reactor and bed material limits the methods for obtaining empirical data of internal bed structures; therefore, advances in scaling and efficiency improvements are challenging. Invasive probes such as anemometers have been used to monitor local bed properties (Boerefijn, Poletto et al. 1999), but these techniques are ill-suited because of their destructive nature to the bed hydrodynamics or bubbling behavior (Kaza 2008). Consequently, noninvasive techniques such as X-ray radiography/stereography in conjunction with particle tracking algorithms (Seeger, Kertzscher et al. 2003) or computed tomography (CT) imaging (Franka, Heindel et al. 2007) are good candidates for providing adequate qualitative and quantitative data.

Monitoring opaque multiphase flows using X-ray visualization has proven to be a useful tool in providing good qualitative and quantitative data of fluidized bed behavior. Successful measurements of time-average gas holdup have been made using these techniques (Grohse 1955; Romero and Smith 1965; Rowe, Santoro et al. 1978; Yates and Cheesman 1992; Kantzas, Wright et al. 2001; Franka and Heindel 2009). This study compares the repeatability and uniformity of the local time-average gas holdup in a 3D 15.2 cm diameter cold flow fluidized bed using X-ray CT imaging. Two different bed materials (glass beads and crushed walnut shell) are investigated over a range of superficial gas velocities and results are compared at various bed heights.

4.3 Experimental Setup

4.3.1 Fluidized Bed Reactor

The fluidized bed reactor used in this study is shown in Fig. 4.1 and is a 3D cold flow reactor modified for side-air injection, although side-air injection was not a part of this study.

The reactor is made of four main components: a plenum, aeration plate, reactor chamber, and freeboard chamber. The reactor is a 15.2 cm ID column manufactured from 0.6 cm thick transparent acrylic material and held together by flanges attached to each section. Nylon bolts are used to fasten the flanges, which are sealed with rubber gaskets. The side-air injection port is located 1.27 cm above the aeration plate and plugged with a nylon bolt in this study.

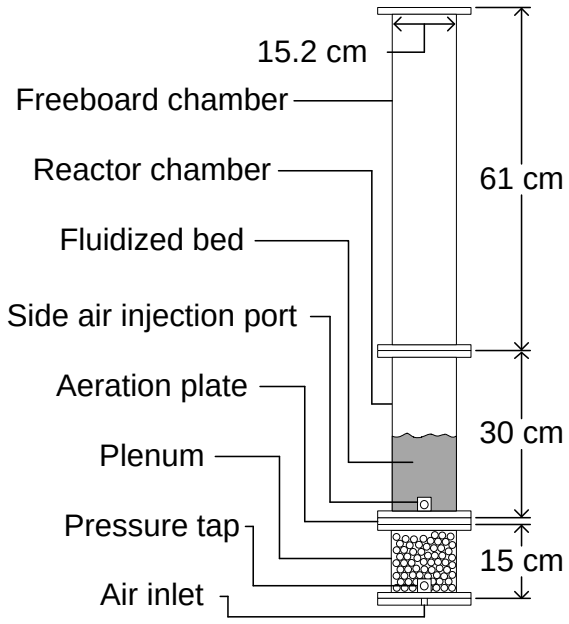

Figure 4.1: Schematic of the 15.2 cm fluidized bed reactor.

The aeration plate is a 1.5 mm thick stainless steel plate with 131 uniformly distributed 1 mm diameter holes over a polar grid originating at the plate center, giving it an open area ratio of 0.57%. A 1.2 cm thick mount held between the plenum and reactor chamber flanges is used to hold the aeration plate in place. The aeration plate is covered with a #45 mesh screen to prevent bed material from clogging the aeration holes.

The plenum contains enough 1.3 cm diameter marbles to fill it ~1 cm below the aeration plate, providing an arduous path through which air can pass, ensuring a uniform pressure distribution across the underside of the aeration plate. The reactor plenum holds a pressure transducer to record pressure for minimum fluidization calculations. This transducer has an error of ±0.25% of full scale, or ±86 Pa. The gas phase enters the system through a fitting located in the bottom of the plenum. After flowing through the bed of marbles, the gas phase then passes through the aeration plate into the reactor chamber. With the proper superficial gas velocity, the gas phase will then fluidized the bed material contained within. A freeboard chamber is included above the reactor chamber to hold any highly excited material due to bubble eruption in the reactor, preventing elutriation of the material.

Fluidization gas (air) is metered through a filtered stainless steel 0-827.4 kPa pressure regulator, and then passes through a 0-1000 Lpm Aalborg GFM671S flow meter with a resolution of ± 2% of full scale. The gas flow rate through the bed is controlled by adjusting the pressure regulator.

4.3.2 Bed Material

Each of the two bed materials used in this study are Geldart type B particles (Geldart 1973). A particle size range of 500-600 μm was utilized in all experiments and obtained by sieving the respective material multiple times. Glass beads are used as a benchmark for the fluidization behavior within the reactor; moreover, they are well characterized and have a fairly uniform spherical shape. Crushed walnut shell is chosen as a comparative bed material

to the glass beads in all aspects except for its natural characteristics and lower density, which makes it easier to visualize with X-rays.

The bulk void fraction for each bed condition is calculated by

$$\varepsilon_{g,b}=1-\rho_b/\rho_p \quad (1)$$

where ρ_b is the bulk density and ρ_p is the particle density provided by the manufacturer. The bulk density is measured for each test condition by recording the bed mass and volume (i.e., $\rho_p = m_{bed}/V_{bed}$, where m_{bed} is the bed mass and V_{bed} is the bed volume). Table 1 provides a summary of the bed properties. Note that the particle density for crushed walnut shell is provided by the manufacturer as a range (1200-1400 kg/m^3) because of the natural variability of the material and the midpoint was used in Eq. (1).

Table 4.1: Material properties

		Glass Beads	Walnut Shell
D_p	[μm]	500-600	500-600
ρ_b	[kg/m^3]	1500	570
m_{bed}	[g]	4160	1580
ρ_p	[kg/m^3]	2600	1200-1400
$\varepsilon_{g,b}$	[-]	0.42	0.56

4.3.3 Minimum Fluidization Velocity

Minimum fluidization velocity is generally determined experimentally because many of the calculable parameters can only be estimated (Davidson and Harrison 1963). According to Davidson and Harrison (1963), Felipe and Rocha (2007), and Hilal et al. (2001), bed packing effects cause a hysteresis affect in the bed when a piece-wise increase of superficial gas velocity is used to find the minimum fluidization velocity. Consequently, pressure drop across the bed is usually measured as the gas flow rate is decreased from fully fluidized to completely unfluidized. Minimum fluidization is then identified by the transition

from a bubbling bed to a fixed bed. A fixed bed is identified by a linearly increasing pressure drop with increasing superficial gas velocity, while the pressure drop is constant in a bubbling bed with increasing superficial gas velocity. Therefore, the superficial gas velocity associated with the transition from linearly increasing to constant pressure drop with increasing superficial gas velocity is the minimum fluidization velocity.

In this study, minimum fluidization velocity was determined by first fluidizing the bed and then recording the system pressure drop as the superficial gas velocity was decreased. A similar process was used to determine the pressure drop across the empty bed at each flow rate. The two pressure drop tests were then subtracted to determine the bed pressure drop as a function of superficial gas velocity (Franka, Drake et al. 2008). For this study, the minimum fluidization velocity was determined to be U_{mf} = 20.2 cm/s for glass beads and U_{mf} = 18.1 cm/s for crushed walnut shell.

The minimum fluidization velocity was then used as a reference condition for the subsequent repeatability and uniformity tests. In this study, the superficial gas velocity was specified at $U_g = 1.5U_{mf}$ and $3U_{mf}$.

4.3.4 X-ray Computed Tomography

The X-ray Computed Tomography (CT) system has been detailed by Heindel et al. (2008) and only a summary is provided here. The CT system uses a liquid cooled LORAD LPX200 X-ray source and emits a conical X-ray beam. The voltage and current can be adjusted from 10 to 200 keV and 0.1 to 10.0 mA, respectively, for a maximum power output of 900 W. In this study, the power settings were 160 keV and 4.5 mA, and 144 keV and 2.8 mA for glass beads and crushed walnut shell, respectively.

The X-ray detector for this study consists of a 44×44 cm CsI phosphor screen that fluoresces when X-rays are incident on it. The resulting image is captured by a 50 mm Nikon lens attached to an Apogee Alta U9 camera with a thermoelectrically cooled 3072×2048 active pixel CCD matrix. The CCD is capable of binning data over ranges from 1×1 to 8×8. The CCD thermoelectric cooler can be set to various temperatures, and exposure times can be changed to reduce noise in the image. The images acquired for this study were captured using the 4×4 binning option resulting in 768×512 effective pixels, with an exposure time of 1 second at a CCD temperature of 0°C.

To reconstruct an X-ray CT image, radiographs of multiple projections are needed. In this study, radiographs are acquired every degree as the X-ray source and detector are rotated around the fluidized bed (360 total radiographs). This process takes approximately 45 minutes and the resulting data are necessarily time-averaged. The multiple 2D radiographs are then reconstructed using filtered back projection (Kak and Slaney 1988; Kini 1994) to produce a 3D CT image. Two image corrections are applied during this process. First, pixel normalization is completed to account for non-uniformities in pixel signal response across the CCD matrix. Second, a beam hardening correction is applied to the glass bead data to account for the polychromatic X-ray source and the preferential absorption of the lower energy X-rays by the high density glass. The low energy X-rays were also filtered for both bed materials by placing two 0.6 mm thick copper plates and one 1.5 mm thick aluminum plate over the X-ray source window. Additional details on the pixel normalization and beam hardening corrections can be found elsewhere (Striegel 2005; Franka 2008; Heindel, Gray et al. 2008).

4.3.5 Gas Holdup

Local gas holdup, ε_g, is determined from (Hammer, Johansen et al. 2006):

$$\varepsilon_g = \frac{\mu-\mu_p}{\mu_g-\mu_p} = \frac{I-I_p}{I_g-I_p} \tag{2}$$

were μ, μ_p, and μ_g is the local X-ray attenuation for a dynamic bed, a particle, and the gas respectively. This assumes that the local X-ray attenuation is proportional to the X-ray CT intensity values for the dynamic bed (I), particle (I_p), and gas (I_g). Unfortunately, the intensity of a single 500 μm particle cannot be found in our system because of resolution issues. However, by solving for I_p in the bulk phase gas holdup:

$$\varepsilon_{g,b} = \frac{\mu_b-\mu_p}{\mu_g-\mu_p} = \frac{I_b-I_p}{I_g-I_p} \tag{3}$$

and substituting into Eq. (2), ε_g can be determined:

$$\varepsilon_g = \frac{I-I_b+\left(I_g-I\right)\varepsilon_{g,b}}{I_g-I_b} \tag{4}$$

where I_b is the intensity of a fixed bulk bed. Assuming the static bulk bed is homogeneous, the bulk phase gas holdup of the fixed bed is constant and obtained from Table 1. Therefore, finding the local time-average gas holdup from a single dynamic bed experiment requires three different X-ray CT files: (1) the X-ray CT of the dynamic bed (flow), (2) the X-ray CT of a static bed of the same material (bulk), and (3) the X-ray CT of an empty bed (gas). These files are used with Eq. (4) to generate a new 3D file that contains the local time-average gas holdup map. Note that all values in Eq. (4), except for $\varepsilon_{g,b}$, have unique time-average values at every voxel (3D pixel) within the imaging domain.

4.4 Results and Discussion

4.4.1 Repeatability

Repeatability was determined by acquiring time-average local gas holdup data (ε_g) for five unique tests with the same flow conditions. This was done for two different materials (glass beads and crushed walnut shell) at two different flow rates (U_g = 1.5 and $3U_{mf}$) to encompass a range of material densities and gas flow rates. Time-average gas holdup values were extracted from each 3D ε_g map in both the x-z and y-z planes. Figure 4.2 shows a schematic of how the 3D ε_g maps were oriented to extract quantitative data. Time-average local gas holdup values were also used to determine the average planar gas holdup in each z-slice as a function of height from each 3D mapping. Because of the large volume of data, only selected results are presented here.

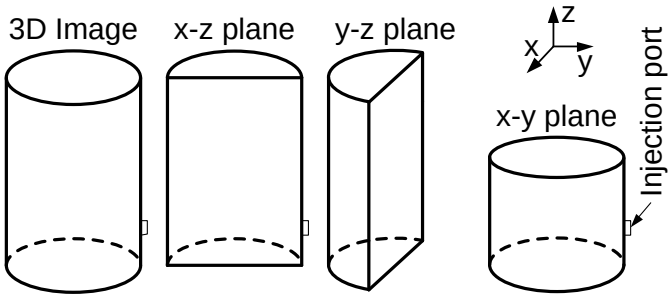

Figure 4.2: Selected X-ray CT imaging planes used for analysis.

High repeatability among all testing groups is observed for both the glass bead and crushed walnut shell beds. Figure 4.3 presents time-average gas holdup data along mutually perpendicular rays passing through the center of the glass bead bed at a bed height of h = 0.5D with $U_g = 1.5U_{mf}$ and $3U_{mf}$. It should be noted that in all graphs displaying ε_g data, discrete data points are obtained every 0.4 mm and the lines connecting data points on the

plots are only presented to show trends and do not imply continuous data. Each graph in Fig. 4.3 shows that all ε_g data sets are fairly uniform across the bed and in a relatively tight grouping in both the x-z and y-z planes. The tight grouping of the ε_g data from the five distinct tests shows that the data are very repeatable across the bed. This is also evident with increasing U_g, which translates to an increase in ε_g.

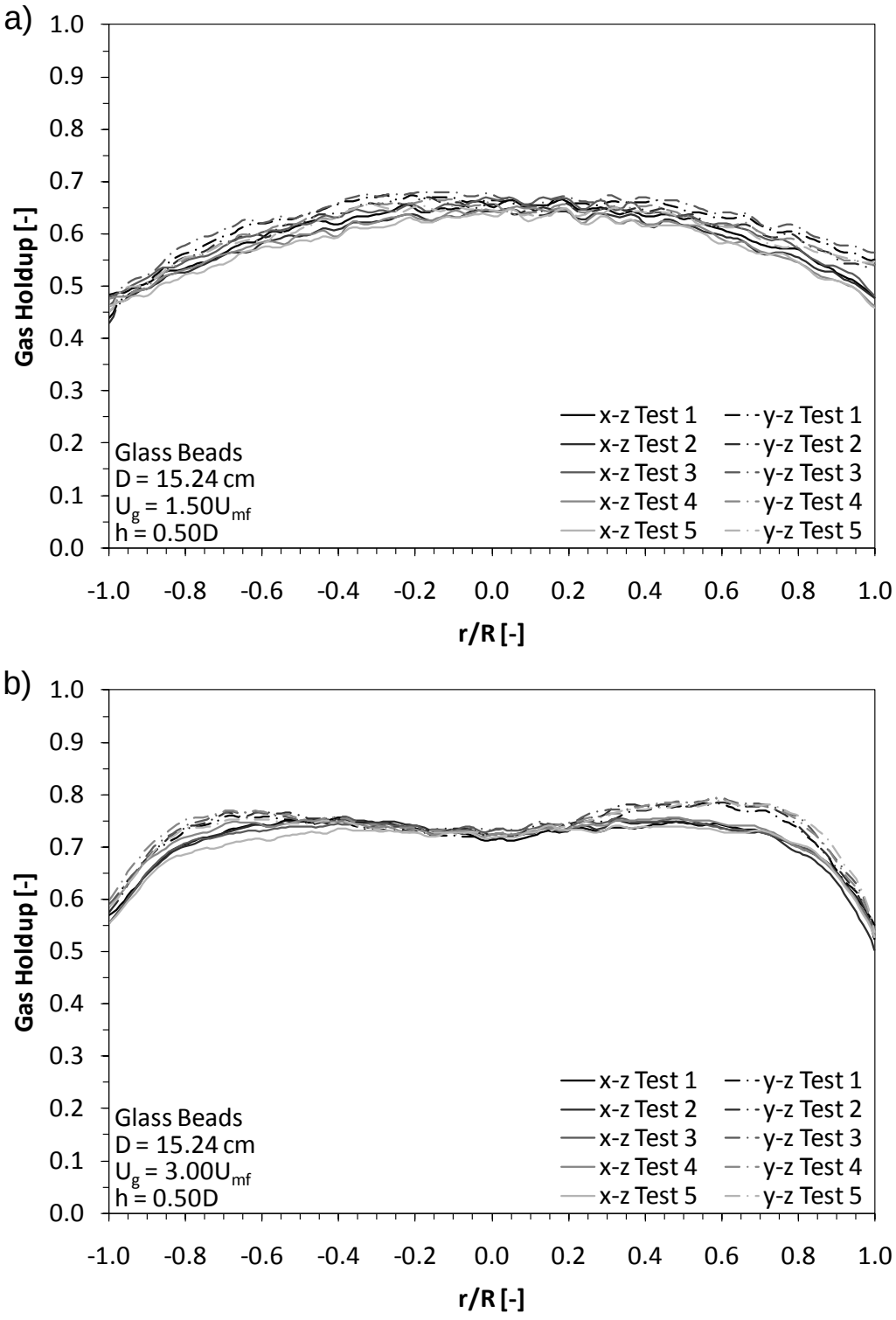

Figure 4.3: Radial x- and y-axis ε_g for a fluidized glass bead bed. Five tests are shown at h = 0.5D with (a) $U_g = 1.5U_{mf}$ and (b) $U_g = 3U_{mf}$.

The differences between the x-z and y-z profiles in Fig. 4.3 are caused by two factors. First, there are slight asymmetries between the two mutually perpendicular planes, which are to be expected in these particulate systems. Second, the difference near the right side of the graphs, particularly at $U_g = 1.5U_{mf}$, is due to a non-uniform boundary condition; the plugged side-air inlet shown in Fig. 4.1 does not provide a smooth wall boundary. The non-uniformity at the wall shows the need for applying proper boundary conditions when completing CFD simulations for comparison.

Figure 4.4 displays ε_g data at a bed height of h = 1D with $U_g = 1.5U_{mf}$ and $3U_{mf}$. Again, the plots show that the ε_g data are fairly uniform with the data sets much tighter at this bed height. The increasing tightness of the ε_g data, in comparison to a height of h = 0.5D, shows that increases in height suppress any local variations.

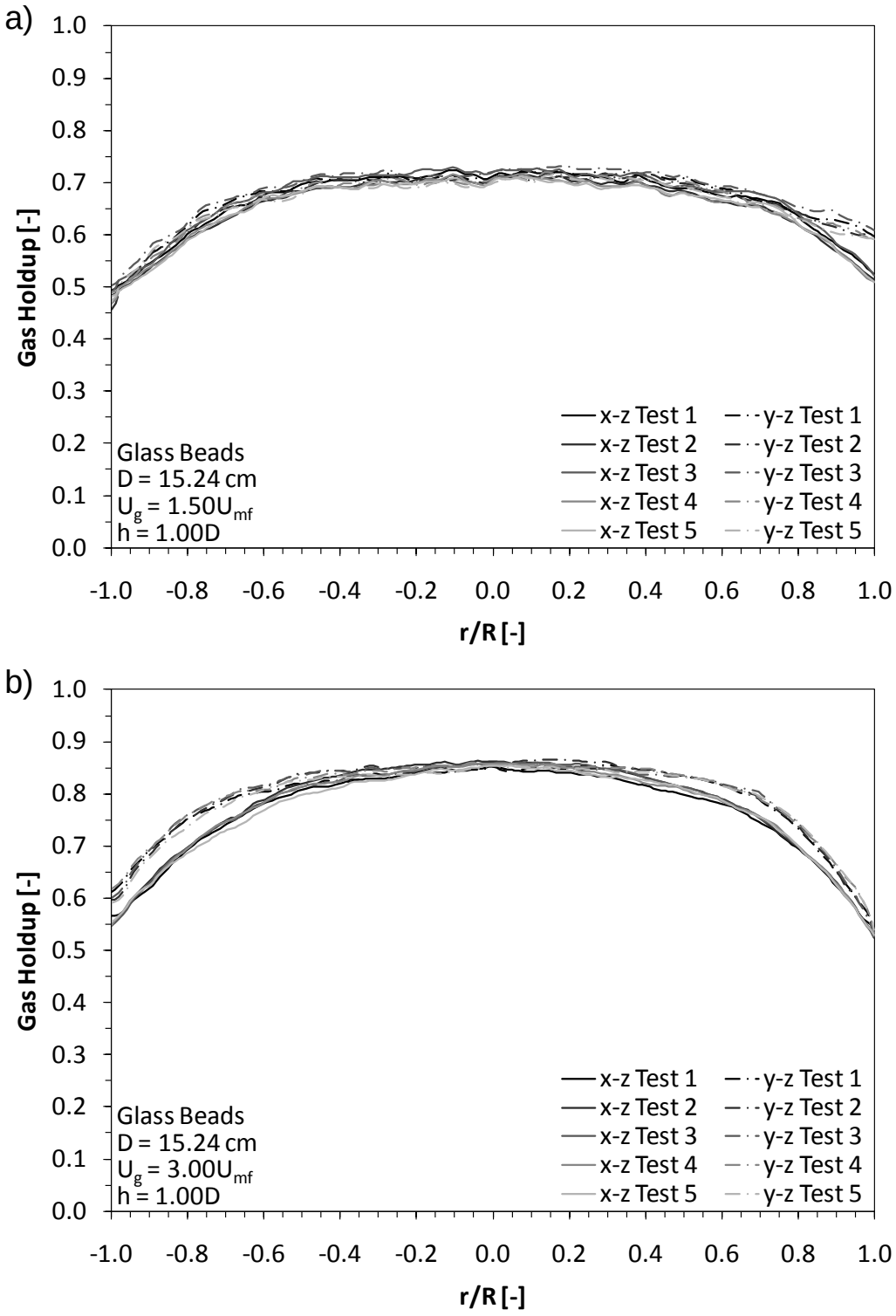

Figure 4.4: Radial x- and y-slice ε_g for a fluidized glass bead bed. Five tests are shown at h = 1D with (a) $U_g = 1.5U_{mf}$ and (b) $U_g = 3U_{mf}$.

When the fluidization material is changed to crushed walnut shell, similar repeatability results are observed (Fig. 4.5). The lighter material provides a flatter gas holdup profile across the bed. The natural crushed walnut shell system has variability in particle morphology and density compared to glass beads. This leads to a slight increases in the variability between tests, but is not significant.

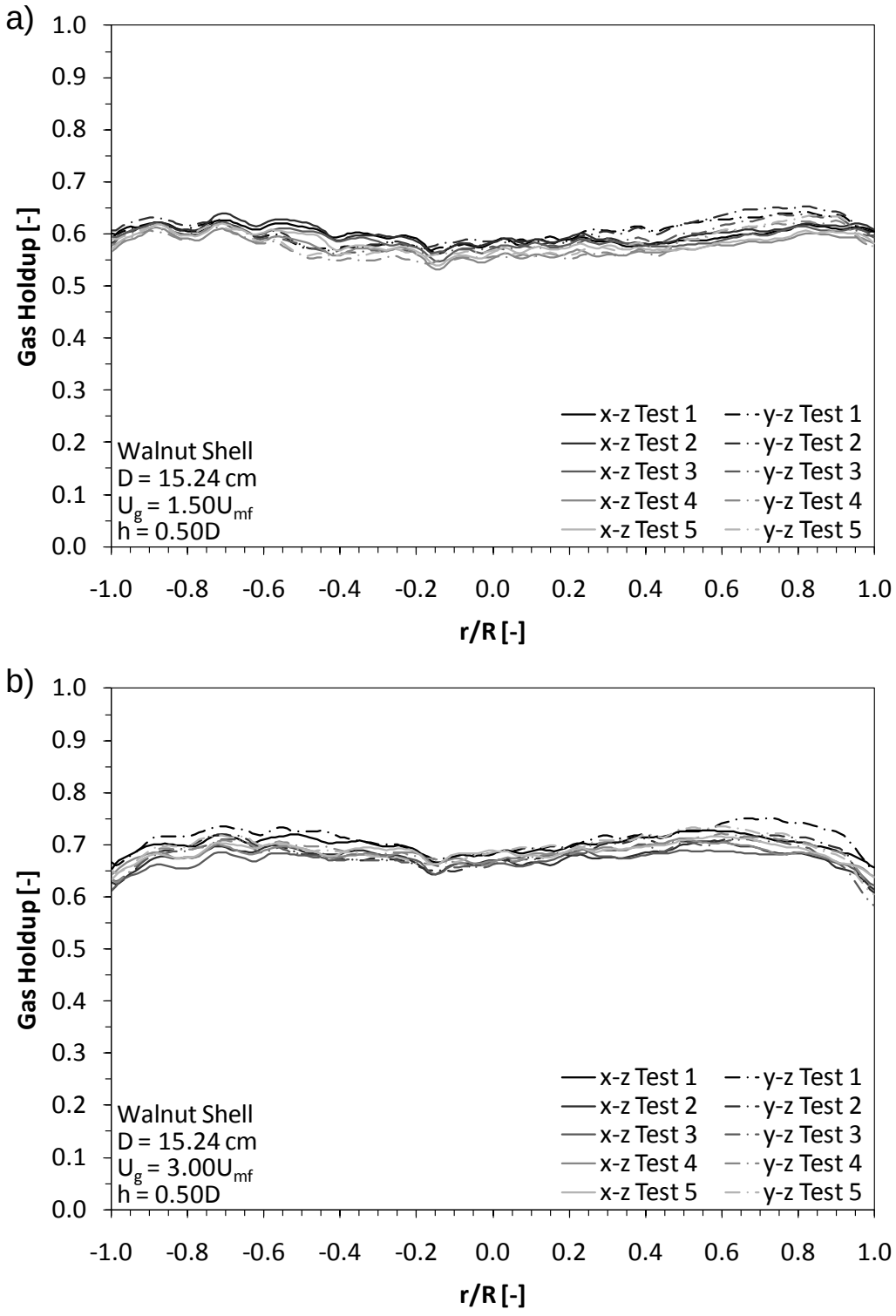

Figure 4.5: Radial x- and y-axis ε_g for a fluidized crushed walnut shell bed. Five tests are shown at h = 0.5D with (a) $U_g = 1.5U_{mf}$ and (b) $U_g = 3U_{mf}$.

Figure 4.6 shows the fluidized bed planar average ε_g for both glass beads and crushed walnut shell plotted as a function of height for $U_g = 1.5U_{mf}$ and $3U_{mf}$. A high degree of agreement between tests is shown by the tight grouping for each condition. The data below a bed height of h = 0.15D are omitted from the figure because the sharp discontinuities in material density caused by the bed flanges create image artifacts in this region. Small deviations exist between data sets for both materials but these are attributed to local variations in the two systems. One general observation is that the glass bead beds have more consistent results between tests; this is due to the fact that the glass bead system is better characterized and more uniform than the (natural) crushed walnut shell system. Also, higher superficial gas velocities generally produce more uniform results between tests because the systems are better mixed at the higher gas flow rates. The planar average values also show smaller variations towards the top of the fluidized bed (e.g., h = 1D) because the mixing is better in this region and any non-uniformities resulting from non-uniform mixing at the base of the bed are eliminated. This figure also shows that increasing the fluidization gas velocity results in bed expansion.

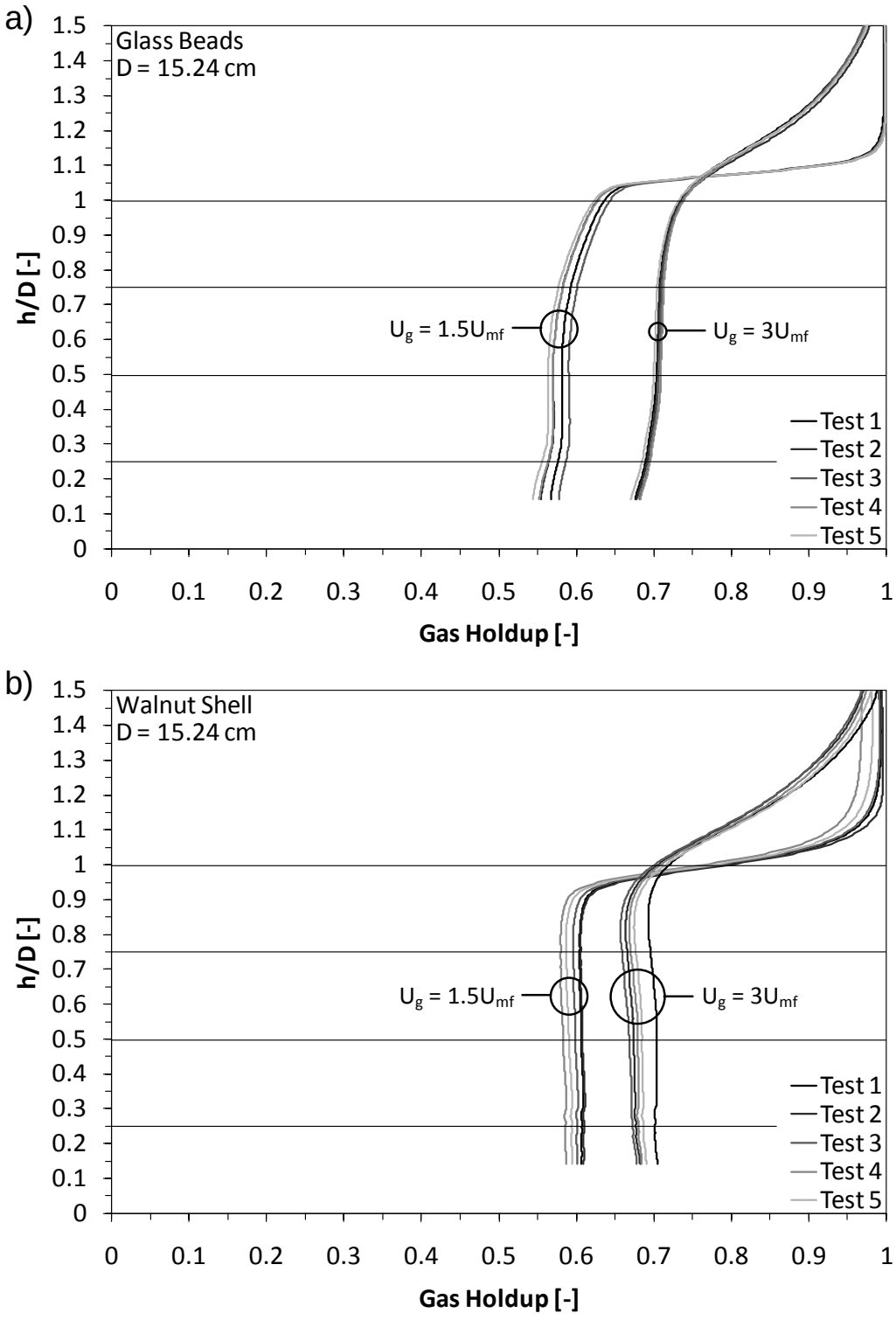

Figure 4.6: The average planar ε_g as a function of height for $U_g = 1.5U_{mf}$ and $3U_{mf}$ for (a) glass beads and (b) crushed walnut shell.

4.4.2 Uniformity

Gas holdup uniformity data were assessed under the same material and flow conditions as the repeatability tests; however, only one test was taken at each condition. Time-average local gas holdup values were extracted from each of the 3D ε_g maps in x-z planes oriented at twelve different azimuthal locations. The data are presented along a ray passing through the bed center in the x-slice ε_g plots at a particular height, where all twelve azimuthal locations are superimposed on the same graph. The presented heights correspond to h = 0.25D and 0.75D, although data at any height could be extracted from the 3D data. The x-slices pierce the bed center-line and are oriented in 15° increments, and correspond to the 12 azimuthal locations shown in Fig 4.7. For example, the x-axis passes through the center of the plugged side-air injection port located at 0° or 180° in Fig. 4.7. To extract the x-slice line of ε_g data across the bed at the 15° position, the X-ray CT data are rotated by 15°, which is easily accomplished in the reconstruction algorithm. This is completed at each of the 12 azimuthal locations for the four completed tests. Note that the aeration holes may or may not fall along a slice plane.

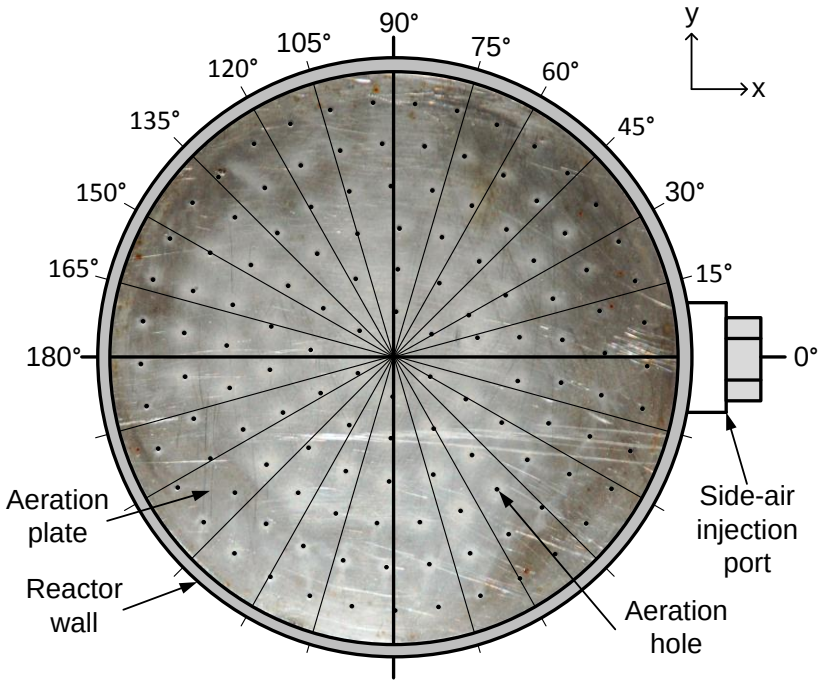

Figure 4.7: Diagram indicating how data are extracted at 12 different azimuthal locations from local time-average ε_g maps to show fluidization uniformity across the bed.

High axi-symmetric fluidization uniformity is observed with the glass bead bed at both U_g. Figure 4.8 presents fluidization uniformity data for glass beads at $U_g = 1.5U_{mf}$ and $3U_{mf}$ at bed heights of h = 0.25D and h = 0.75D. At h = 0.25D and $U_g = 1.5U_{mf}$, axi-symmetric fluidization shows regions of non-uniformity due to the fluidization jets from the discrete holes in the aeration plate. One region of jetting is observed by relatively large increases of ε_g over azimuthal locations from 55° to 120° and radial positions $-0.6 \leq r/R \leq -0.25$. Another region can be seen over azimuthal locations 60° and 105° and radial positions $0.3 \leq r/R \leq 0.6$. Lastly, large amounts of jetting occur near the reactor walls for all azimuthal locations and result in large ε_g fluctuations. At h = 0.25D and $U_g = 3U_{mf}$, mixing is promoted deeper into the bed, reducing jet penetration and increasing the uniformity in the bed center.

Jetting and the resulting air bubbles migrate towards the bed walls at h = 0.25D, causing the increase in gas holdup (and fluctuations) in this region.

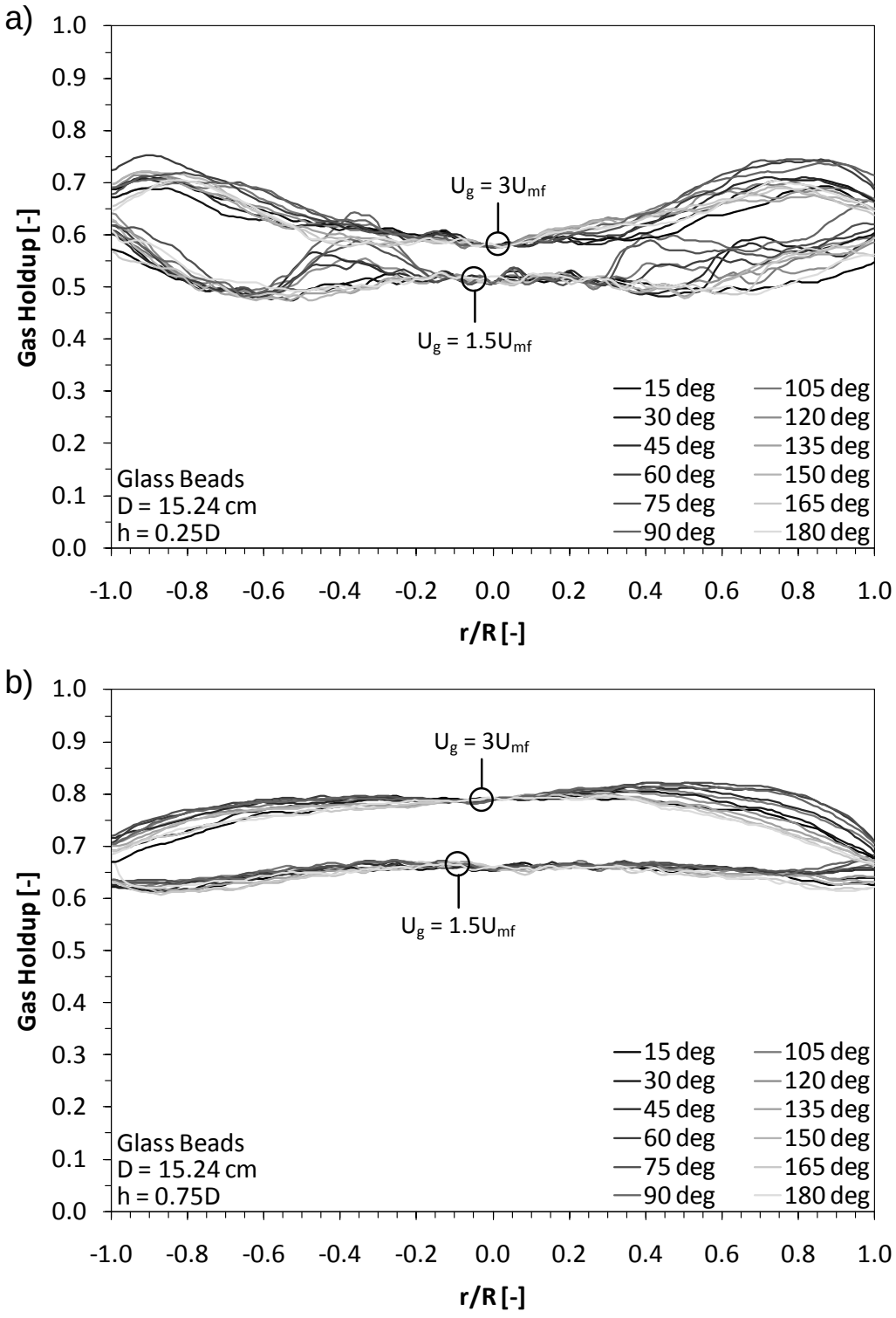

Figure 4.8: Radial x-slice ε_g for fluidized glass beads at $U_g = 1.5U_{mf}$ and $3U_{mf}$ at bed heights of (a) h = 0.25D and (b) 0.75D.

As height increases to h = 0.75D with $U_g = 1.5U_{mf}$, axi-symmetric fluidization becomes more uniform. This is expected because of gas dispersion throughout the bed at higher locations. At h = 0.75D and $U_g = 3U_{mf}$, fluidization is also more uniform and higher gas holdup regions migrate towards the reactor center. For both flow rates, the variations directly above the plugged side-air injection port emphasize how non-uniform wall boundary conditions can affect local conditions, even far away from the wall non-uniformity.

Figure 4.9 displays the axi-symmetric fluidization data for crushed walnut shell. The same trends are recorded for a fluidized crushed walnut shell bed as for a fluidized glass bead bed at the same heights and flow rates. At a lower height and velocity, e.g., h = 0.25D and $U_g = 1.5U_{mf}$, there are fluidization non-uniformities due to the effects of individual jets penetrating into this region. When U_g increases to $3U_{mf}$ with h = 0.25D, the non-uniformities caused by the individual jets are suppressed because the increased mixing enhances the bed uniformity deeper into the bed. Increasing the bed height to h = 0.75D for both flow rates also increases the bed uniformity.

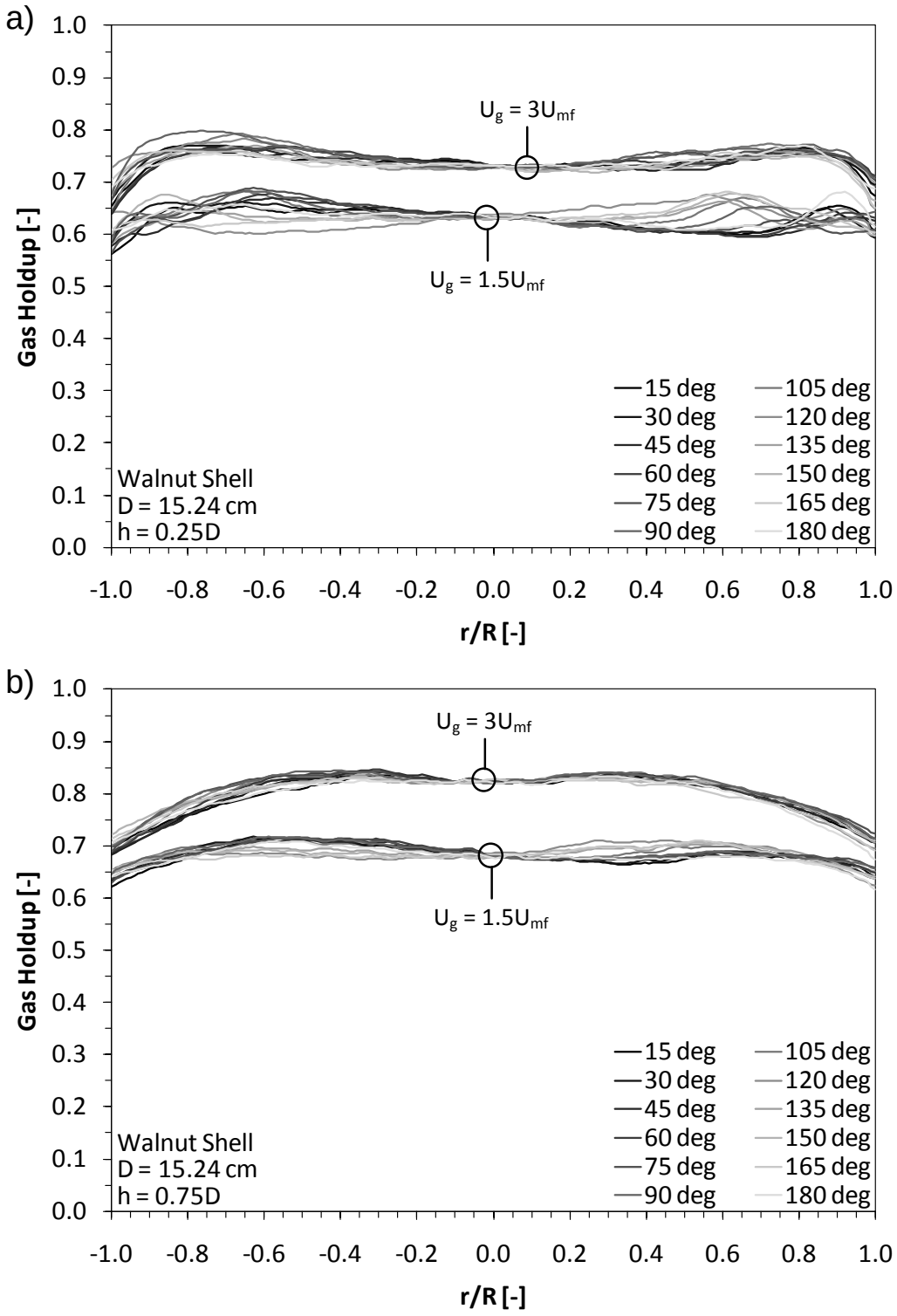

Figure 4.9: Radial x-slice ε_g for fluidized crushed walnut shell at $U_g = 1.5U_{mf}$ and $3U_{mf}$ at bed heights of (a) h = 0.25D and (b) 0.75D.

The most important outcome of Figs. 4.8 and 4.9 is that the majority of local non-uniformities caused by individual aeration jets are eliminated as the distance from the aeration plate increases. By analyzing the data at bed height locations of h = 0.25, 0.5, 0.75, and 1D (not shown), a bed height of h = 0.5D produced axi-symmetric gas holdup profiles for all tested conditions. And this height can be reduced by increasing the mixing in the bed. This is particularly important when comparing computational fluid dynamics (CFD) models to experimental data for model validation (Deza, Franka et al. 2009; Min, Drake et al. 2010). Most CFD simulations apply a uniform gas velocity inlet profile and this assumption is applicable as long as the bed height is far enough from the aeration region when comparing simulations to experimental data.

4.5 Conclusions

Time-average gas holdup data obtained by X-ray computed tomography have been shown to be highly repeatable. Five distinct tests using crushed walnut shell and glass beads at two different gas flow rates showed high repeatability in a 3D 15.2 cm ID cold flow fluidized bed reactor. Characteristic differences in bed materials caused slight variations in the repeatability.

Data extracted at different azimuthal locations showed that uniformity within the bed is highly dependent on the bed height, gas flow rate, and reactor geometry. Hydrodynamic structures such as jetting occurred near the aeration region. As gas flow rate increased, jetting tended to decrease due to increased mixing of the bed and resulted in more axi-symmetric flow. Lastly, slight variations in reactor geometry created variations in the flow conditions that persisted well beyond the variation.

CHAPTER 5 LOCAL TIME-AVERAGE GAS HOLDUP COMPARISONS IN COLD FLOW FLUIDIZED BEDS WITH SIDE-AIR INJECTION[2]

Equation Chapter 5 Section 1

5.1 Abstract

Fluidized beds are interesting and useful processing systems that are employed in many industries such as processing biomass into biofuels or the coating of pharmaceuticals. Knowledge of fluidized bed hydrodynamics is necessary for the design and scale-up of such devices. This paper describes the local time-average differences of gas holdup in a 10.2 cm and 15.2 cm diameter cold flow fluidized bed that were recorded using 3D X-ray computed tomography. Three different Geldart type B bed materials are studied at various superficial gas velocities and side-air injection flow rates, where the side-air injection simulated the immediate volatilization of a fuel like coal or biomass particles. Variations in side-air injection flow rate have little influence on global bed hydrodynamics, but significantly affects local gas holdup. Axial annular flow dominates over all flow conditions for each material and bed diameter. Wall effects increasingly influence hydrodynamics as bed diameter decreases for all materials.

5.2 Introduction

Processes such as granular mixing, drying, pyrolysis, and catalytic cracking widely use fluidized bed reactors for production of various consumer goods. Large voids of interstitial gas (i.e., bubbles) cause circulation of the bed material giving rise to properties

[2] Drake, J. B. and T. J. Heindel (2011). "Local time-average gas holdup comparisons in cold flow fluidized beds with side-air injection." Chemical Engineering Science **To Appear**.

such as low pressure drops, uniform temperature distributions, and high heat and mass transfer rates (Grace 2006; Cui and Grace 2007). To improve the design and scale-up for industrial applications, an understanding of the bed hydrodynamic behavior is required. Selected hydrodynamic studies have used a variety of experimental techniques such as fiber optic probes (Schweitzer, Bayle et al. 2001) or electrical capacitance tomography (Wang, Yu et al. 2010). The hydrodynamics of different bed diameters without side injection have also been presented in the literature (Knowlton, Karri et al. 2005; Wu, Yu et al. 2007). This paper focuses on bed diameter effects on the bed hydrodynamics when side-air is also injected into the bed, where the side-air injection simulates the immediate volatilization of a fuel stream.

Some of the major problems with fluidized bed scale-up involve the following: large gas throughputs requiring large reactor diameters; large reactor heights requiring greater process efficiencies; the addition of heat exchange systems for highly exothermic processes; and the location of feedstock and recirculated material injection ports taking advantage of recirculation zones. The influence of these issues on the bed hydrodynamics is related to the bed material and its properties and their bubbling characteristics. These properties not only describe the material but also determine how gas interacts with, and passes through, the bed. Depending on the process, a horizontal injection of gas into the reactor wall may be required. Moreover, the type of material that comprises the bed is important because it may interact with the feedstock that may be injected for possible conversion processes, as well as the reactor walls that contain it. A close look at the internal hydrodynamic structures within two different internal diameter cold flow fluidized bed reactors with side-air injection may give some insight to this problem.

Due to the nature of fluidized beds, the study of their hydrodynamics is problematic at best and, at times, impossible (Drake, Franka et al. 2008). Invasive and noninvasive methods can be employed, however, noninvasive observation techniques are more reliable (Geldart and Xie 1992). Techniques such as electrical capacitance (Du, Warsito et al. 2005), X-ray absorption (Drake and Heindel 2011), γ-ray absorption (Patel, Waje et al. 2008), or positron emission tomography (Dechsiri, Ghione et al. 2005) utilize field measurements (i.e., capacitance, absorption, transmission, etc.) to quantify local property variations. X-ray visualization has proven to be a useful tool in providing good qualitative and quantitative data of dynamic behavior. A review of various X-ray flow visualization techniques has recently been completed (Heindel 2011). Successful measurements have been made of fluidized bed hydrodynamic conditions using X-ray imaging techniques (Grohse 1955; Romero and Smith 1965; Rowe, Santoro et al. 1978; Yates and Cheesman 1992; Kantzas, Wright et al. 2001; Franka and Heindel 2009; Escudero and Heindel 2011). Liquid holdup (Toye, Marchot et al. 1998), solid concentrations (Grassler and Wirth 2000), and phase velocities through particle tracking (Kantzas, Wright et al. 2001; Seeger, Kertzscher et al. 2003; Drake, Franka et al. 2008) have also been completed using X-ray imaging techniques.

This paper uses X-ray computed tomography to record the local time-average gas holdup in two different fluidized beds operated over a range of conditions, without and with side-air injection, revealing bed diameter effects on local hydrodynamic conditions.

5.3 Experimental Setup

5.3.1 Fluidized Bed Reactor Design

The fluidized bed reactors used in this study are cold flow reactors modified for side-air injection (Figure 5.1). Both reactors are only summarized here since Franka (2008) discusses the design of the 10.2 cm diameter reactor in detail and the 15.2 cm diameter reactor has a similar design. The two fluidized bed reactors are made of transparent polyacrylic material allowing X-rays to pass through with little to no attenuation affects. Each component is bolted together with nylon bolts, and sealed with rubber gaskets cut so as not to interfere with the gas flow through the system. Each reactor has a boss located at the bottom of the reactor chamber that is tapped with a centerline located 1.27 cm above the aeration plate. This tap holds a nylon fitting used for side-air injection and is plugged with a nylon bolt when side-air injection is not being used. The nylon fitting holds a 0.95 cm ID tube used for side-air injection and simulates the immediate volatilization of a fuel stream such as coal or biomass particles. The injection port centerline does not differ between the 10.2 cm diameter and 15.2 cm diameter reactors.

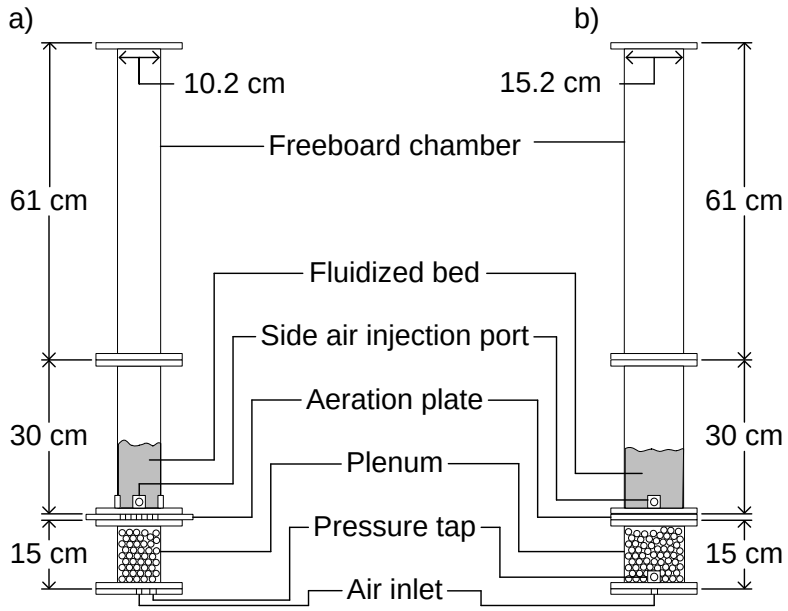

Figure 5.1: Schematic of the (a) 10.2 cm and (b) 15.2 cm fluidized bed reactor (not to scale).

The aeration plate for the 10.2 cm diameter reactor is composed of a transparent polyacrylic plate that is perforated with 62 uniformly distributed 1 mm diameter holes over a polar grid originating at the plate center, providing an open area ratio of 0.62%. The aeration plate for the 15.24 cm diameter reactor is designed in the same fashion but constructed of a stainless steel plate with 131 holes for an open area ratio of 0.57%. Each aeration plate is covered with a 470 μm mesh separating the reactor chamber from the plenum. A pressure transducer is fixed to the plenum to read pressure for minimum fluidization studies. This transducer is located on the bottom of the plenum for the 10.2 cm diameter reactor and on the side of the 15.24 cm diameter reactor.

5.3.2 Bed Material Selection

Each of the three bed materials used in this study (glass beads, crushed walnut shell, and ground corncob) were chosen based on four criteria: fluidization behavior, size range,

density, and aspect ratio. To achieve similar fluidization behavior between different bed materials, Geldart type B particles are used (Geldart 1973). The visualization of the fluidization behavior of low density particles is attractive because of the nature of X-rays. Moreover, uniformly shaped particles are desirable because they fluidize most like conventional inert fluidized bed systems. The particles in this study were chosen because of their availability and represent a range of particle densities. Table 1 provides a summary of the bed material properties used in this study.

Glass beads were chosen as a baseline material because they are well characterized, have a fairly uniform shape, and have similar properties to inert sand as is commonly used in industrial fluidized bed systems. This material is used as a benchmark for the fluidization behavior of various materials within both fluidized bed reactors. However, glass beads have a fairly high density and provide challenges with the X-ray imaging techniques like nonuniform attenuation (beam hardening) and signal penetration. Consequently, crushed walnut shell and ground corncob were chosen as comparative bed materials to the glass beads. The aspect ratio of the crushed walnut shell and ground corncob is not uniform, yet when compared with the Geldart classification chart, all three materials fall within the Geldart type B grouping (Geldart 1973).

To measure the bed weight and bulk density, each material is placed into either reactor at a height of 1 reactor diameter, slightly fluidized to remove packing effects, and removed from the reactor and weighed. The bulk density, ρ_b, for each bed is then calculated by

$$\rho_b = \frac{m_{bed}}{V_{bed}} \tag{1}$$

where m_{bed} is the bed mass and V_{bed} is the bed volume. The particle density (ρ_p) for each material is provided by the manufacturer. The bulk void fraction for each bed is calculated by

$$\varepsilon_{g,b}=1-\frac{\rho_b}{\rho_p} \quad (2)$$

2.1.1 Minimum Fluidization Velocity

Determination of the minimum fluidization velocity is completed experimentally. The superficial gas velocity (U_g) is set to a point past where the bed begins to bubble then reduced to zero, because packing effects cause a hysteresis affect when superficial gas velocity is increased (Davidson and Harrison 1963; Hilal, Ghannam et al. 2001; Felipe and Rocha 2007). Therefore, pressure drop across the bed is measured as the gas flow rate is decreased from fully fluidized to completely unfluidized as described by Franka (2008). The velocity at which the bed transitions from a bubbling to a fixed bed is identified as the minimum fluidization velocity. When the pressure drop vs. superficial gas velocity is analyzed quantitatively, a bubbling bed is identified by a constant pressure drop with an increasing superficial gas velocity and a fixed bed is associated with a linearly increasing pressure drop with increasing superficial gas velocity. Side-air flow rates are referenced to the minimum fluidization volumetric flow rate (Q_{mf}). A summary of the minimum fluidization velocities and flow rates used for each material in each reactor is included in Table 1.

2.1.2 X-ray Computed Tomography

Only a summary of the X-ray computed tomography (CT) equipment used in this study is given here; Heindel et al. (2008) have described it in detail. The X-ray source is a liquid cooled LORAD LPX200 that emits a conical X-ray beam. A maximum of 900 W can be provided through an adjustable voltage and current from 10 to 200 keV and 0.1 to 10.0 mA, respectively. A 44×44 cm CsI phosphor screen that fluoresces when X-rays are incident on it is used as the X-ray detector for this study. A 50 mm Nikon lens attached to an Apogee Alta U9 camera with a thermoelectrically cooled 3072×2048 active pixel CCD matrix captures the resulting image. The CCD is capable of binning data over ranges from 1×1 to 8×8. To reduce noise in the images, exposure times and the CCD thermoelectric cooler can be set to various times and temperatures, respectively.

X-ray CT reconstruction requires the capture of multiple radiographic images taken from different projections. In this study, radiographs are acquired at every degree around the fluidized bed for a total of 360 radiographs, which takes approximately 45 minutes. A 3D CT image is then reconstructed using filtered back projection (Kak and Slaney 1988; Kini 1994), two image corrections are applied during this process, and the resulting data is time-averaged. During the first image correction, a pixel normalization is completed where non-uniformities from noise in the pixel signal response across the CCD matrix is smoothed. Second, the polychromatic X-ray source and preferential absorption of lower energy X-rays cause false signals by high density materials and a beam hardening correction is applied. A combination of 0.6 mm and 1.5 mm thick copper and aluminum plates are placed over the X-ray source window to filter the low energy X-rays to also reduce beam hardening effects. Additional details on the pixel normalization and beam hardening corrections can be found

elsewhere (Striegel 2005; Franka 2008; Heindel, Gray et al. 2008). A summary of the equipment settings used to acquire data for each material and reactor is included in Table 1.

Table 5.1: Experimental properties and settings

		10.2 cm reactor			15.2 cm reactor		
		Glass Beads	**Walnut Shell**	**Corncob**	**Glass Beads**	**Walnut Shell**	**Corncob**
Material Properties							
D_p	[μm]	500-600	500-600	500-600	500-600	500-600	500-600
ρ_b	[kg/m^3]	1491	579	392	1500	570	395
m_{bed}	[g]	1220	477	323	4160	1580	1098
ρ_p	[kg/m^3]	2600	1200-1400	800-1200	2600	1200-1400	800-1200
$\varepsilon_{g,b}$	[-]	0.43	0.55	0.61	0.42	0.56	0.6
Minimum Fluidization Velocity and Flow Rate Conditions							
U_{mf}	[cm/s]	21.7	18.4	17.1	20.2	16.3	16.8
Q_{mf}	[L/min]	105.3	89.3	83.2	220.6	178.4	183.7
Equipment Settings							
Source Voltage	[keV]	150	130	130	160	139	139
Source Current	[mA]	3.5	3.2	3.2	4.5	3.9	3.9
CCD Exposure	[s]	1	1	1	1	1	1
CCD Temperature	[ºC]	0	0	0	0	0	0
Filters	[-]	1Al & 2Cu	1Al & 1Cu	1Al & 1Cu	1Al & 2Cu	1Al & 1Cu	1Al & 1Cu
Binning	[-]	4x4	4x4	4x4	4x4	4x4	4x4

2.1.3 Gas Holdup Calculation and Display

Gas holdup or void fraction is defined as the volumetric gas fraction inside the bed, and the local time-average gas holdup, ε_g, is determined from (Heindel 2011):

$$\varepsilon_g = \frac{\mu-\mu_p}{\mu_g-\mu_p} = \frac{I-I_p}{I_g-I_p} \tag{3}$$

were μ, μ_p, and μ_g are the local X-ray attenuation for a dynamic bed, a particle, and the gas, respectively. This assumes that the local X-ray attenuation is proportional to the X-ray CT values for the dynamic bed (I), particle (I_p), and gas (I_g). Unfortunately, the CT value of a single 500 μm particle cannot be found in our system because of resolution issues. However, by solving for I_p in the bulk phase gas holdup:

$$\varepsilon_{g,b} = \frac{\mu_b - \mu_p}{\mu_g - \mu_p} = \frac{I_b - I_p}{I_g - I_p} \tag{4}$$

and substituting into Eq. (3), ε_g can be determined:

$$\varepsilon_g = \frac{I - I_b + \left(I_g - I\right)\varepsilon_{g,b}}{I_g - I_b} \tag{5}$$

where I_b is the CT value of a fixed bulk bed. Assuming the static bulk bed is homogeneous, the bulk phase gas holdup of the fixed bed is constant and obtained from Table 1. Therefore, finding the local time-average gas holdup from a single dynamic bed experiment requires three different X-ray CT files: (1) the X-ray CT of the dynamic bed (flow), (2) the X-ray CT of a static bed of the same material (bulk), and (3) the X-ray CT of an empty bed (gas). These files are used with Eq. (5) to generate a new 3D file that contains the local time-average gas holdup map. Note that all values in Eq. (5), except for $\varepsilon_{g,b}$, have unique time-average values at every voxel (3D pixel), which are 450 μm × 450 μm × 450 μm in size, within the imaging domain. The ε_g calculation error is estimated to be approximately ±2%.

Qualitative ε_g maps are displayed as images by slicing the newly generated 3D file into slices as shown in Fig. 5.2. The y-slice bisects the reactor through the center of the bed and the injection port and is important for describing the effects of side-air injection on fluidization, while the z-slice illustrates fluidization symmetry at various heights above the distributor plate in each reactor. The left and right edges of the x-slice images represent the boundaries of the fluidized bed while the bottom of the CT image corresponds to the top of the distributor plate. The side-air injection port is identified by a gray rectangular region on the bottom right of the y-slices. Each CT image includes a color scale showing ε_g which is

identical for all slices in a given material and reactor but differs between materials. Therefore, the color scales are modified to improve image resolution in the respective figures.

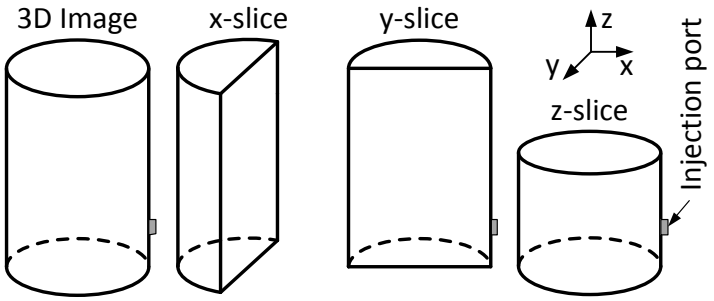

Figure 5.2: CT imaging planes.

2.2. Results and Discussion

Local time-average gas holdup was determined for each bed diameter and material by acquiring a single CT data set for each desired flow condition, which has been shown to be repeatable (Drake and Heindel 2011). Four superficial gas velocities (U_g = 1.25U_{mf}, 1.5U_{mf}, 1.75U_{mf}, and 2U_{mf}) with five side-air flow rates (Q_s = 0Q_{mf}, 0.05Q_{mf}, 0.1Q_{mf}, 0.15Q_{mf}, and 0.2Q_{mf}, where Q_{mf} is the minimum fluidization volumetric flow rate) were chosen for each material-reactor combination. Results of ε_g will be presented with both qualitative and quantitative data primarily focusing on glass beads. Note that only results for U_g = 1.5U_{mf} and 2U_{mf} with Q_s = 0Q_{mf}, 0.1Q_{mf}, and 0.2Q_{mf} are presented here for representative comparisons but results at the other flow conditions follow the recorded trends.

2.2.1 Effects of Side-air Injection on Gas Holdup

Trends of side-air injection were very similar for all three materials used in this study; hence, glass beads will be the focus of this section. Figure 5.3 presents qualitative ε_g data for

a fluidized glass bead bed in both reactors at $U_g = 1.5U_{mf}$. This figure, and others like it, present y- and z-slice ε_g maps for both reactors running at a specified U_g with side-air injection flow rates of $Q_s = 0Q_{mf}$, $0.1Q_{mf}$, and $0.2Q_{mf}$. The first three columns correspond to the 10.2 cm diameter bed, while the last three columns denote the 15.2 cm diameter bed. Each flow condition contains two z-slices located above and two below each y-slice that signify the ε_g map across the bed at a particular height above the distributor (h = 0.25D, 0.5D, 0.75D, and 1D). The side-air injection port is indicated by a small dark gray box at the right of the y-slices for both geometries. To simplify comparisons between geometries, ε_g for both reactors is scaled over the same range found at the bottom of the figure. Also note that the physical domain of each geometry represents the respective bed internal diameters.

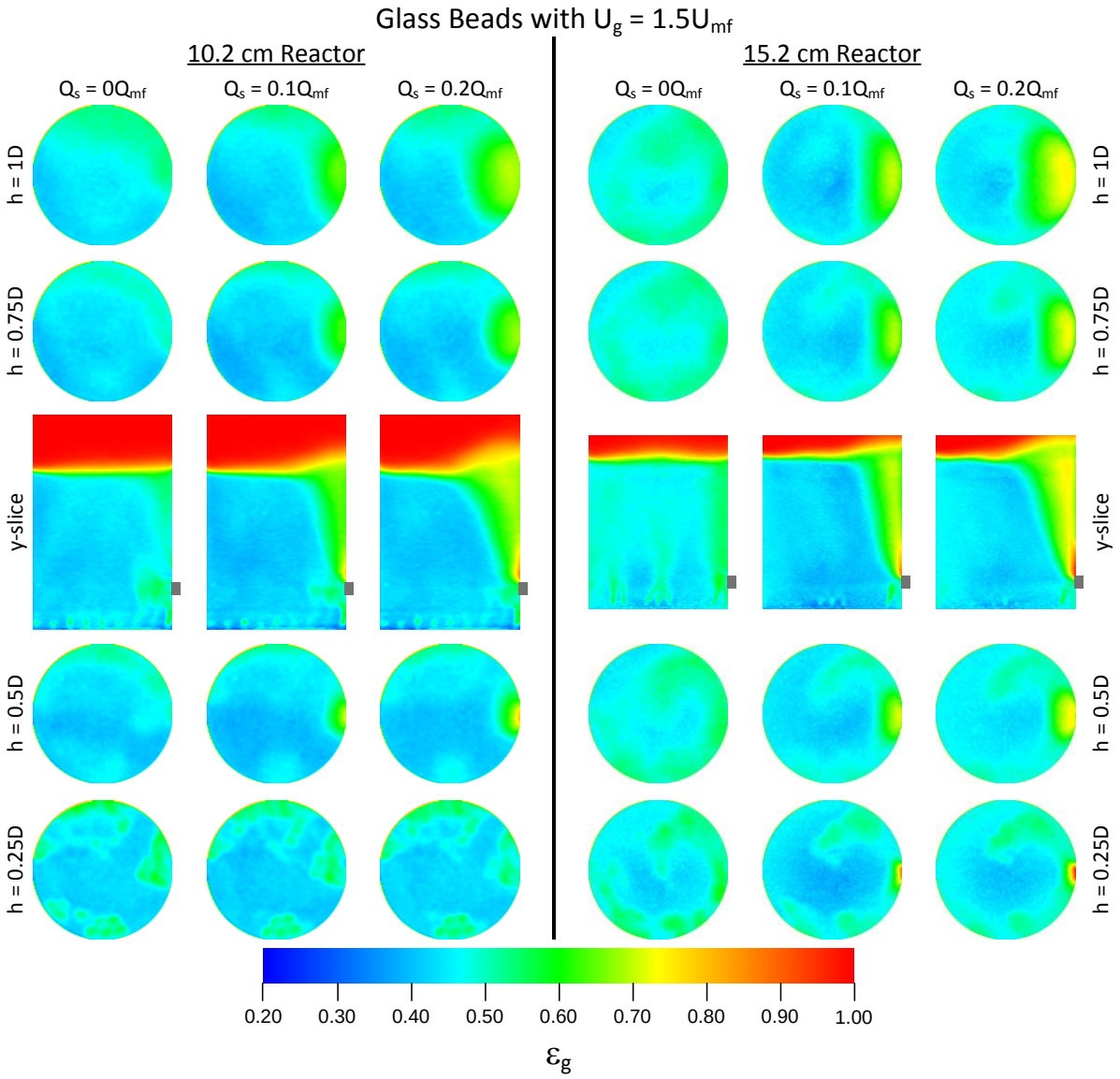

Figure 5.3: Qualitative ε_g for a fluidized glass bead bed in both reactors at $U_g = 1.5U_{mf}$ with varying Q_s.

Figure 5.3 reveals the influence of side-air injection on the general bed hydrodynamics. When $Q_s > 0Q_{mf}$, a large plume of relatively high gas holdup is observed on the right of the y-slice just above the side-air injection port. The plume is a preferential air flow channel created by friction along the adjacent wall where a boundary layer of air from the side-air injection port can easily burrow through the bed. A core, identified by the streak

of yellow within the plume, appears to be present as Q_s increases indicating the preferential flow path, particularly in the 15.2 cm diameter bed. The plume disperses horizontally towards the bed center as height increases due to an increased horizontal projection of the gas momentum from enhanced gas-solid interaction. Plume penetration also increases with increasing Q_s. The time-average bed height directly above the plume is greater than that of the rest of the bed, and increasing Q_s increases this height. This observation is expected because of an increased amount of volumetric air injected into the system. Note that the time-average bed height outside of the plume stays relatively constant regardless of changes in Q_s. Note the gas holdup increase near the side-air injection port when $Q_s = 0Q_{mf}$ is caused by a local boundary condition non-uniformity (Drake and Heindel, 2011); the side-air plug does not provide a smooth wall condition at this location.

Although the side-air injection plume significantly changes the ε_g distribution near the injection port, a relatively uniform flow is observed outside this region. Small regions of relatively high ε_g are observed near the bottom of the bed and are jets from the individual aeration holes in the aeration plate. As bed height increases, these jets appear to either coalesce into larger regions of increased volume or diffuse horizontally into the bed. Qualitatively, jet length and coalescence is not affected by changes in Q_s.

Figure 5.4 displays plots of local ε_g vs. radial position for a fluidized glass bead bed in both bed diameters at (a) h = 0.5D and (b) h = 1D with $U_g = 1.5U_{mf}$ and $Q_s = 0Q_{mf}$, $0.1Q_{mf}$, and $0.2Q_{mf}$. The line graphs in Fig. 5.4 represent local time-average ε_g as a function of radial position and is normalized with the respective reactor radius (r/R); data points have been replaced by continuous lines used to represent trends and do not imply continuous data. The quantitative data displayed in Fig. 5.4 show slight differences that are difficult to realize in

Fig. 5.3. First, the non-dimensional horizontal plume penetration into the bed with increasing height is smaller in the 10.2 cm diameter bed than in the 15.2 cm diameter bed. Second, the ε_g profile within the plume region at the wall differs with bed height. Both the plume diffusion and profile differences occur due to wall effects and the relative height of the injection port centerline with respect to the static bed height. Major losses from wall effects require more energy to fluidize the 10.2 cm diameter bed because of greater frictional losses; therefore, advective effects within hydrodynamic structures like the plume are decreased.

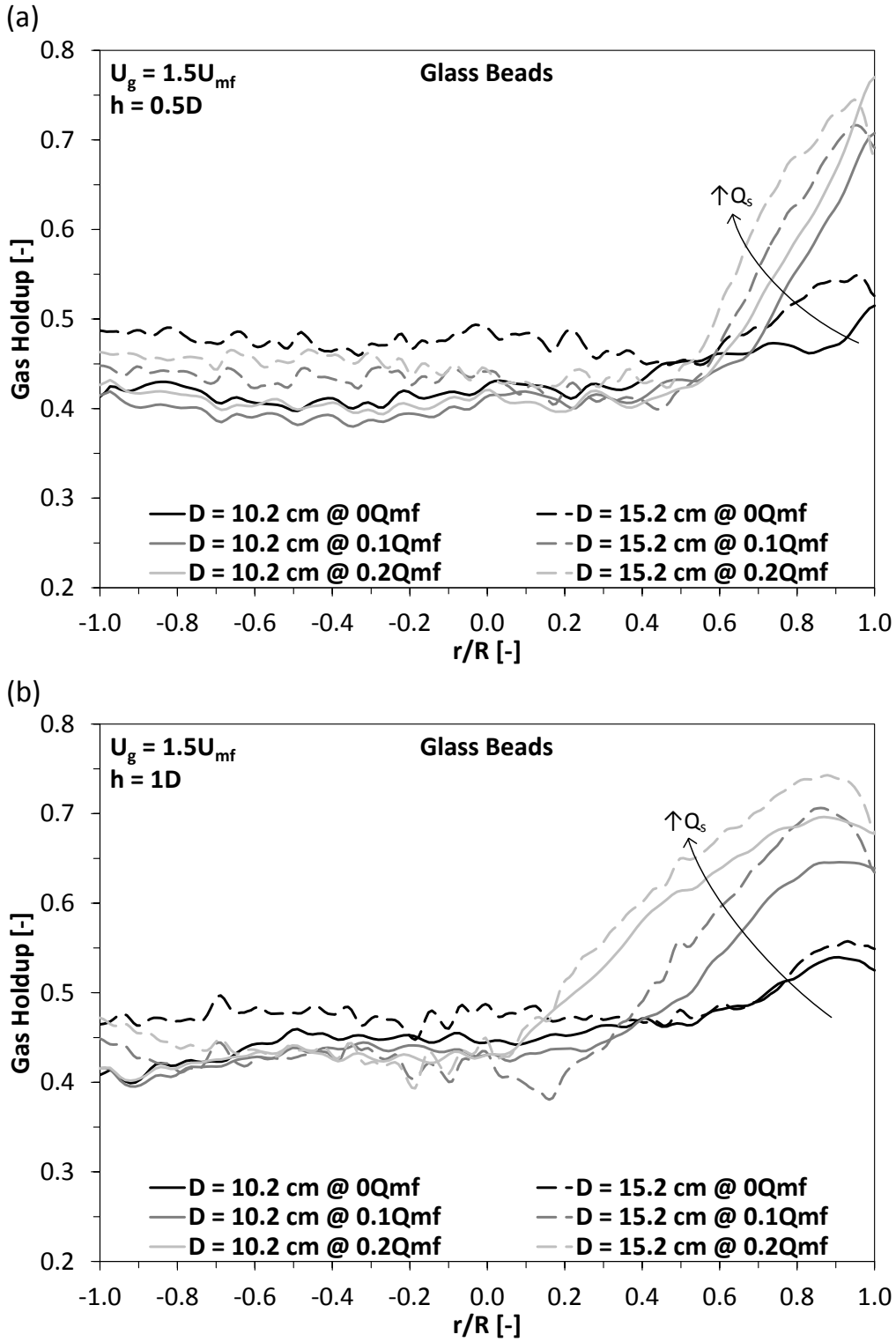

Figure 5.4: Local time-average gas holdup for a fluidized glass bead bed in both reactors at (a) h = 0.5D and (b) h = 1D, where $U_g = 1.5U_{mf}$ with varying Q_s.

Figure 5.5 presents qualitative ε_g data for a fluidized glass bead bed in both reactors at $U_g = 2U_{mf}$. An expansion of approximately 25% and 12% is observed for the 10.2 cm and 15.2 cm diameter beds, respectively. The difference in expansion is due to wall effects increasing the energy to fluidize the bed. Variations of U_g highly affect the relative influences of side-air injection in both bed diameters. First, at higher U_g, the plume from the side-air injector appears to be completely enveloped by an increased annular flow due to increased mixing were only the plume core is observed. Second, an increased horizontal diffusion into the bed can be seen in the plume core at higher U_g, which indicates an increased fluidization quality with higher U_g. Lastly, the difference between the time-average bed height above the plume and the rest of the bed decreases as U_g increases. Similar qualitative results (not shown) are observed when the bed material is changed to crushed walnut shell or ground corncob.

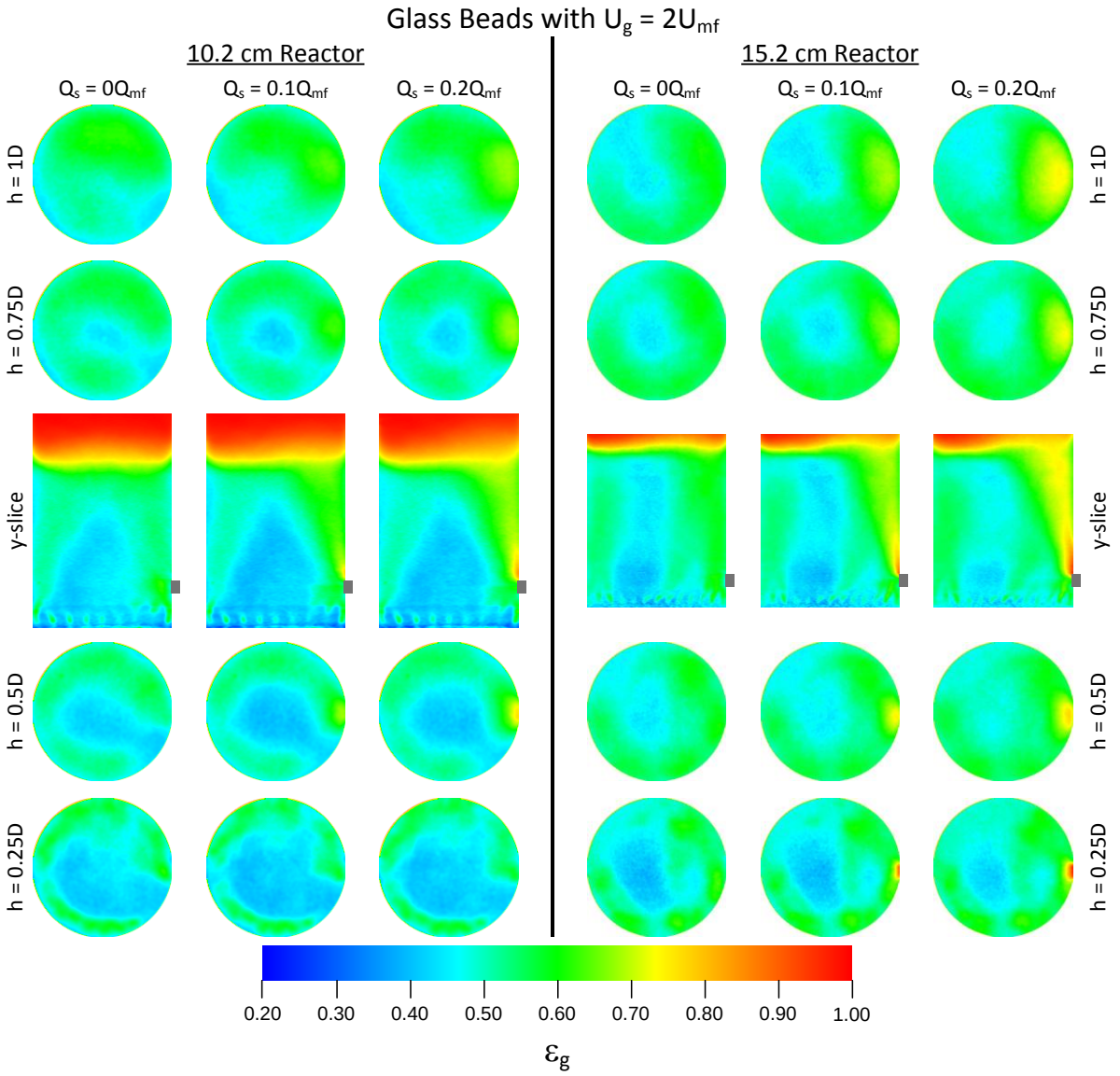

Figure 5.5: Qualitative ε_g for a fluidized glass bead bed in both reactors at $U_g = 2U_{mf}$ with varying Q_s.

Observations show that raising U_g increases annular flow throughout the bed from top to bottom in both bed diameters. However, a difference in annular flow between bed diameters is also observed. In the 10.2 cm diameter bed, ε_g increases annularly in the horizontal direction towards the bed core as bed height increases. These increases converge in the bed center between h = 0.75D and 1D, creating a "pile" of relatively low ε_g from this

height to the bottom of the bed. This implies that bubbles form near the walls at the bottom of the bed and grow while migrating towards the bed center as they rise to the surface, confirming results reported by Davidson and Harrison (1963) and Lim et al. (2007). These observations are seen in the 15.2 cm diameter bed as well; however, a convergence in the bed center does not occur, in fact, the increase stops at approximately h = 0.5D, leaving a column of relatively low ε_g at the bed core over the entire height of the bed.

The effects of changing U_g without side-air injection on general bed hydrodynamics can be observed in Fig. 5.6a at lower regions of the bed. Figure 5.6 displays plots of local ε_g vs. radial position for a fluidized glass bead bed in both bed diameters at (a) h = 0.25D and (b) h = 1D when $Q_s = 0Q_{mf}$ and $U_g = 1.25U_{mf}$, $1.5U_{mf}$, $1.75U_{mf}$, and $2U_{mf}$. A lack of fluidization uniformity is seen at h = 0.25D for all U_g in both bed diameters, which appear as local regions of higher ε_g across the bed. These regions are areas of coalescence from aeration jets lower in the bed. They tend to occur at similar locations, either at or near the bed walls and core, and expectedly rise in value as U_g increases. As U_g increases, mixing is enhanced and the areas of coalescence that occur in the central regions of the bed at h = 0.25D have migrated to the bed walls at h = 0.5D (not shown). This action increases the ε_g profile near the walls as they become more tightly grouped near the bed core. This migration trend shows the preferential gas paths in the lower portions of the bed.

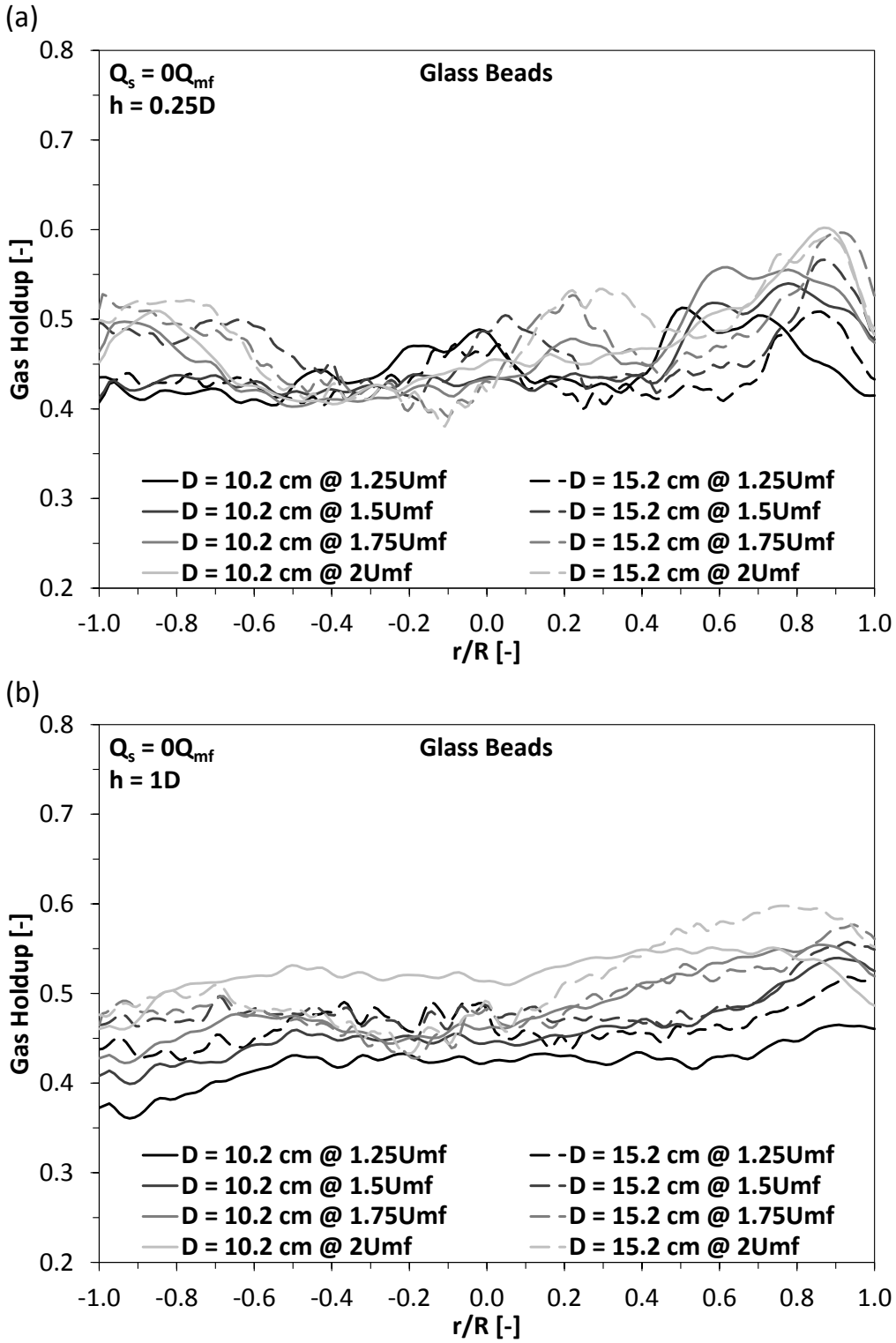

Figure 5.6: Local time-average gas holdup for a fluidized glass bead bed in both reactors at (a) h = 0.25D and (b) h = 1D, where $Q_s = 0Q_{mf}$ with and varying U_g.

The effects on general bed hydrodynamics in higher regions of the bed from changing U_g without side-air injection can be observed in Fig. 5.6b. It shows that fluidization uniformity increases with height and the wall coalescence regions begin to diffuse horizontally into the bed for both diameters and the amount of diffusion into the bed is comparable between diameters as height increases. At h = 1D the coalescence region at the right wall appears to have completely diffused into the bed for both diameters, however, the region at the right wall does not change. Again, this is an effect created by the side-air injection port and although the port is plugged, the plug surface is flat and not curved with the inside of the reactor forming a small ridge at the bed wall. One difference that is observed as U_g increases in the upper portions of the bed between diameters is that ε_g profiles in the 10.2 cm diameter bed begin to increase slightly over the entire bed diameter whereas in the 15.2 cm diameter bed, this occurs only above the side-air injector (the right side of Fig. 5.6b).

The influence of side-air injection on local gas holdup is clearly shown in Fig. 5.7 where plots of local ε_g vs. radial position are shown for a fluidized glass bead bed in both bed diameters at (a) h = 0.5D and (b) h = 1D with $U_g = 2U_{mf}$ and $Q_s = 0Q_{mf}$, $0.1Q_{mf}$, and $0.2Q_{mf}$. The quantitative data agree with the trends observed by the qualitative data regarding side-air injection affects with changing U_g. However, there are noticeable differences in ε_g profiles. First, a dip in the ε_g profile across the bed in the core region occurs at h = 0.5D with $U_g = 2U_{mf}$, whereas it is not as apparent at h = 1D. Second, it is clear from Fig. 5.7 that the 15.2 cm diameter reactor provides a higher ε_g in the side-air plume and the plume penetrates farther into the bed than in the 10.2 cm reactor, due to decreased wall effects that in-turn increase mixing. Plume penetration also increases with increasing Q_s.

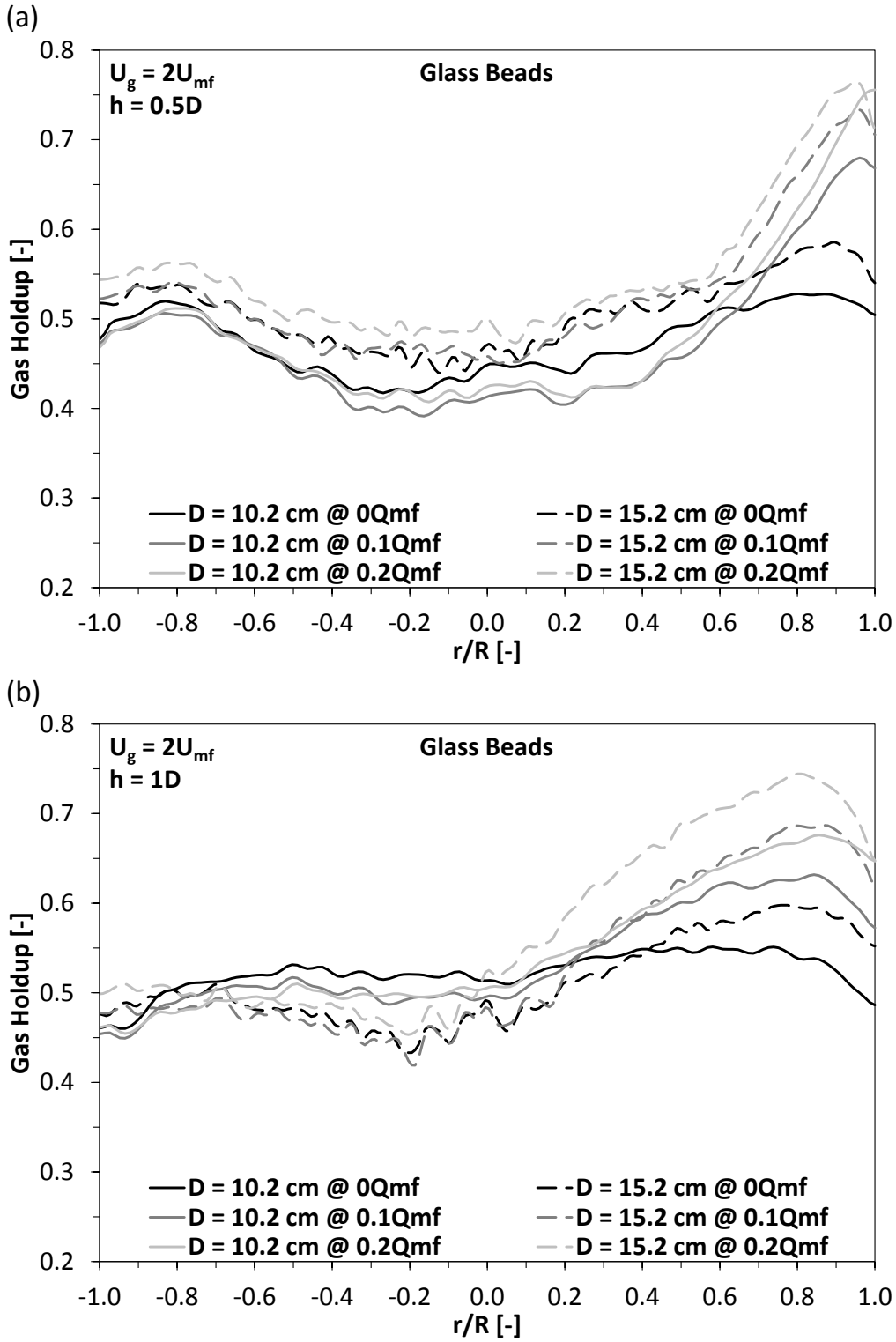

Figure 5.7: Local time-average gas holdup for a fluidized glass bead bed in both reactors at (a) h = 0.5D and (b) h = 1D, where $U_g = 2U_{mf}$ with varying Q_s.

2.2.2 Effects of Bed Material Variation on Gas Holdup

Figure 5.8 compares gas holdup maps in the reactor mid-planes as bed material changes for both bed diameters at $U_g = 2U_{mf}$ with $Q_s = 0Q_{mf}$ and $0.1Q_{mf}$. Image intensity values in Fig. 5.8 are scaled over ranges that begin at the respective materials bulk void fraction to 1 for easier comparison of hydrodynamic structures between bed materials and diameters. The respective scale for each material is shown at the bottom of the set of images for the particular material. Both bed diameters are scaled to the same normalized diameter for height comparisons. Changes in material density do not appear to affect hydrodynamic structures or fluidization uniformity in either diameter bed when operating at the same Q_s. The time-average bed height for all materials tends to be slightly higher in the 10.2 cm diameter bed due to wall effects. No significant changes occur when U_g is changed. Jetting in the aeration zone is similar for both bed diameters but appears to change in height from glass beads to ground walnut shell and crushed corncob. With the exception to differences in the jet penetration length, these trends indicate that particle type and density have a negligible effect on bed hydrodynamic structures except in the aeration region at the bottom of the bed.

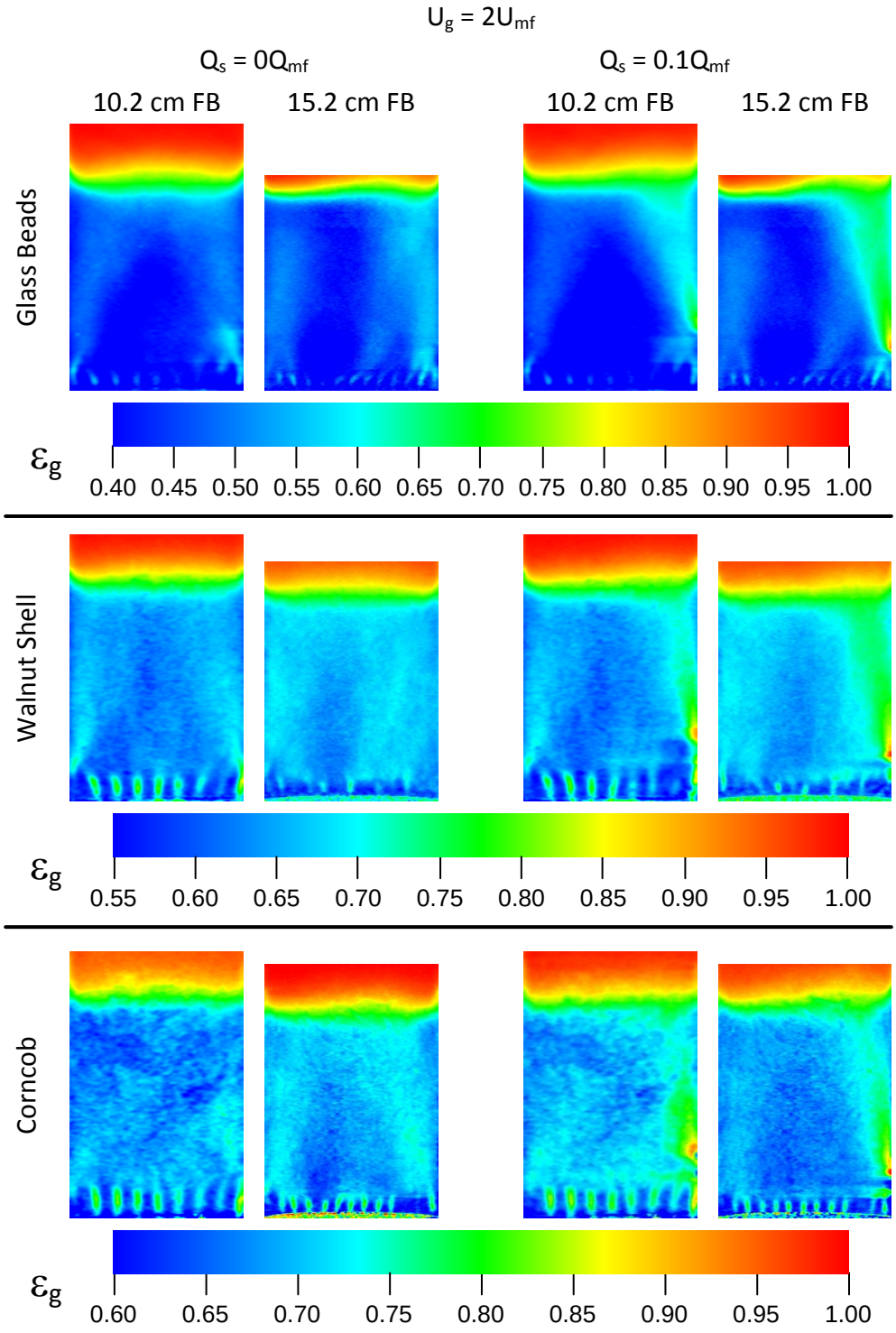

Figure 5.8: Y-slice time-average gas holdup for all materials in both reactors at $U_g = 2U_{mf}$ for $Q_s = 0Q_{mf}$ and $0.1Q_{mf}$.

Figure 5.9 displays plots of local ε_g vs. radial position for all materials in both bed diameters at h = 0.75D when (a) $U_g = 1.5U_{mf}$ and (b) $U_g = 2U_{mf}$ and $Q_s = 0Q_{mf}$. The crushed walnut shell and ground corncob have higher local ε_g values because the initial bulk values ($\varepsilon_{g,b}$) are higher due to the porous nature of these natural materials. The ε_g profile appears to be slightly higher in the 15.2 cm diameter bed for all materials when $U_g = 1.5U_{mf}$ but the difference is negligible when $U_g = 2U_{mf}$ due to enhanced mixing. The ε_g uniformity across the beds is increased using the lighter material because the heavy glass beads suppress bed mixing compared to lighter materials. When side-air injection is introduced into the beds (Fig. 5.10), similar trends are observed.

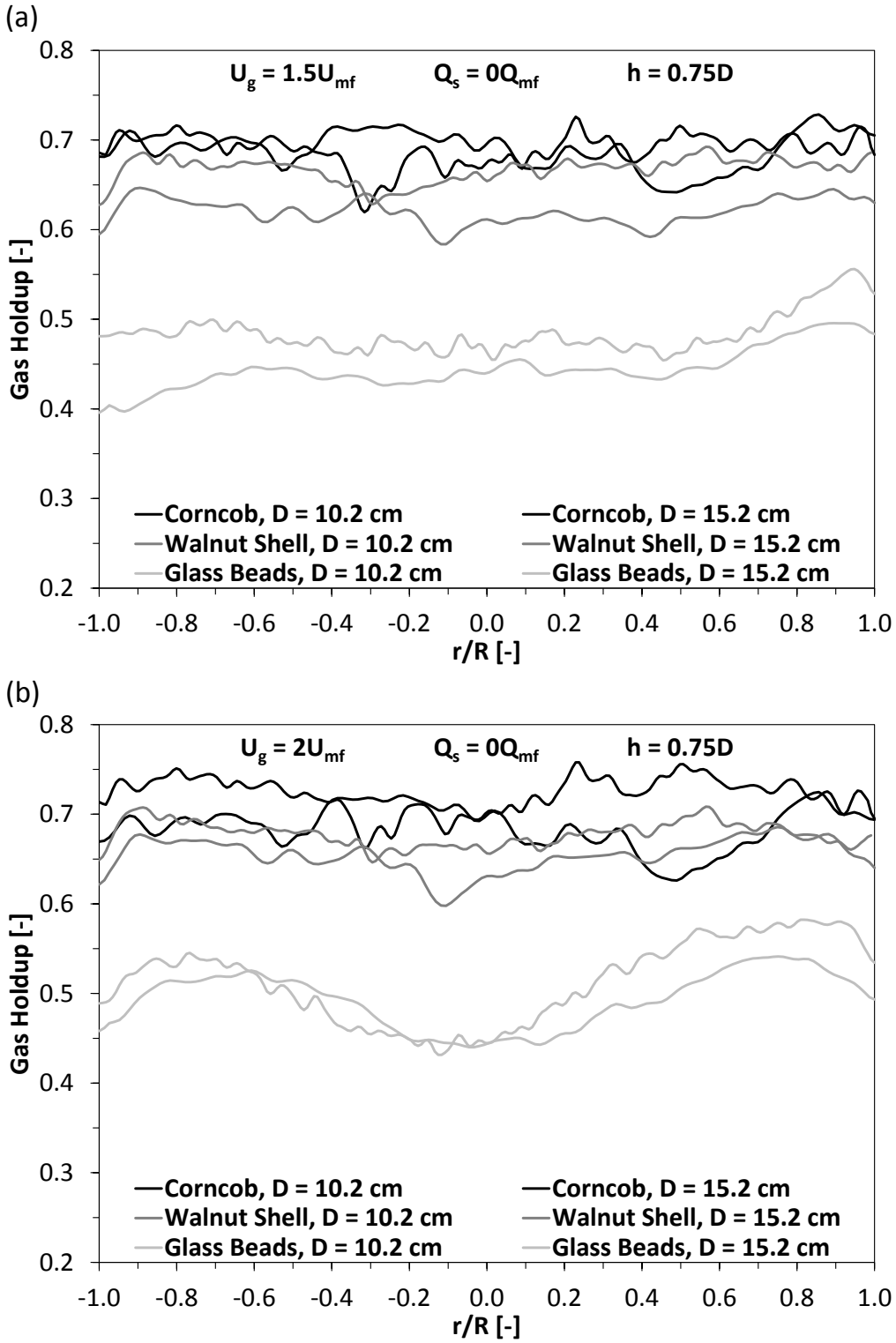

Figure 5.9: Local time-average gas holdup for all materials in both reactors at (a) $U_g = 1.5U_{mf}$ and (b) $U_g = 2U_{mf}$, where $Q_s = 0Q_{mf}$ and h = 0.75D.

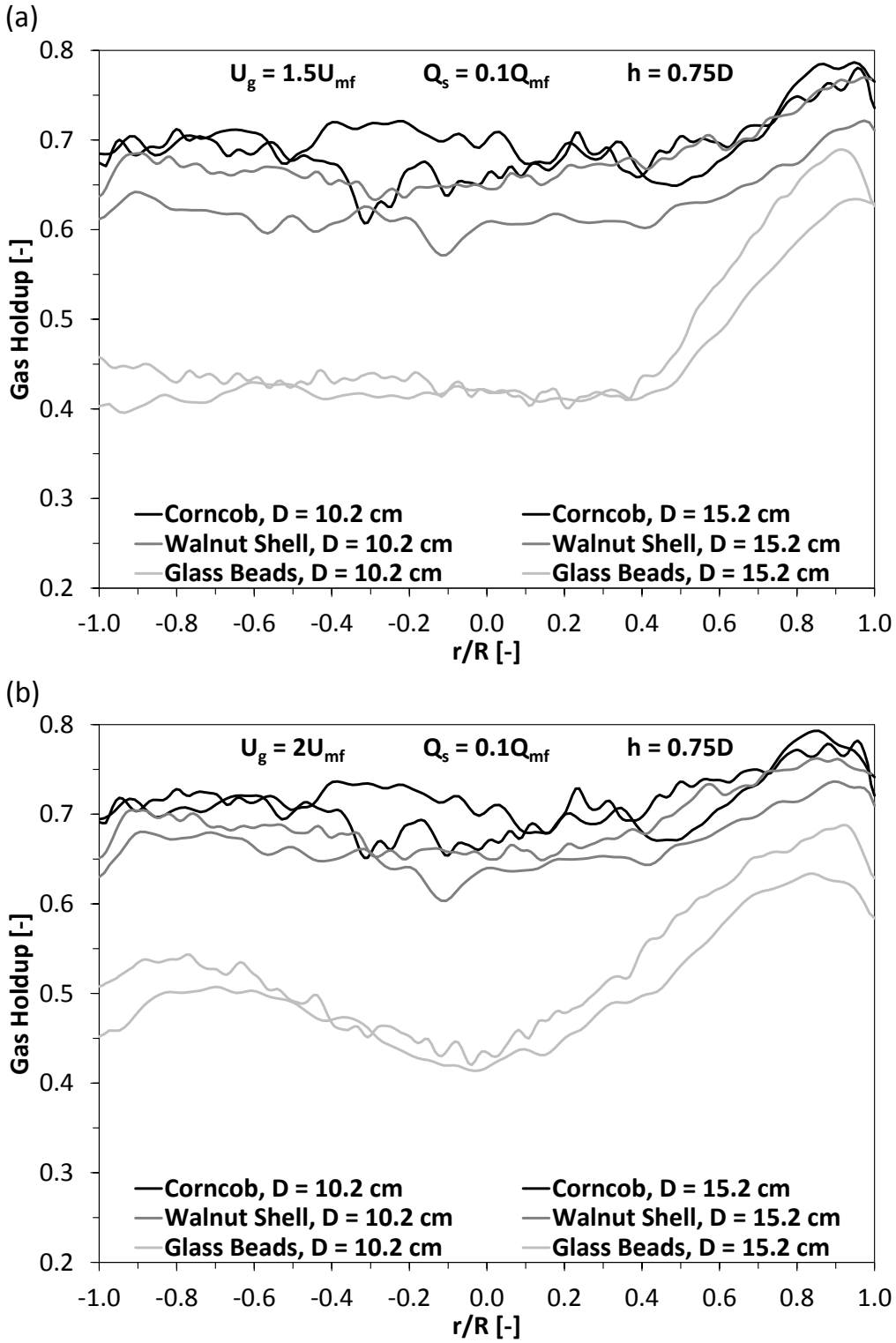

Figure 5.10: Local time-average gas holdup for all materials in both reactors at (a) $U_g = 1.5U_{mf}$ and (b) $U_g = 2U_{mf}$, where $Q_s = 0.1Q_{mf}$ and h = 0.75D.

2.3. Conclusions

The effects of fluidization velocity, side-air injection, material density, and bed diameter on the bed hydrodynamic structures and local time-average gas holdup were investigated in this study. Local time-average gas holdup becomes increasingly annular as bed height increases; furthermore, it increases with increasing U_g and Q_s and decreasing material density. Bed diameter did not affect the overall structure of ε_g, however, the locations of relatively high ε_g differed between bed diameters. Bubble migration in the 10.2 cm diameter bed began at the walls low in the bed and then migrated to the reactor center in which an annular convergence occurred. In the 15.2 cm diameter bed, bubble migration again began at the walls low in the bed, but only slightly migrated towards the bed center. The 10.2 cm diameter bed had a slightly higher time-average bed height when compared to the 15.2 cm diameter bed due to wall effects. Differences in the locations of relatively high ε_g between bed diameters are also due to wall effects and differences in material densities in the aeration region of the bed. Changes in side-air injection flow rate do not have a significant effect on general hydrodynamic structures when varying bed material density or bed diameter. The side-air injection plume is the dominant hydrodynamic structure and tends not to affect the annular flow within any fluidized bed over all side-air and superficial gas flow rates. Overall, bed mixing and uniformity were enhanced in both reactors when a lighter material was used.

CHAPTER 6 COMPARISONS OF ANNULAR HYDRODYNAMIC STRUCTURES IN 3D FLUIDIZED BEDS USING X-RAY CT[3]

Equation Chapter 6 Section 1

6.1 Abstract

Fluidized beds are common equipment in many process industries. Knowledge of the hydrodynamics within a fluidized bed on the local scale is important for the improvement of scale-up and process efficiencies. This knowledge is lacking due to limited observational technologies at the local scale. This paper uses X-ray computed tomography (CT) imaging to describe the local time-average gas holdup differences of annular hydrodynamic structures that arise through axisymmetric annular flow in a 10.2 cm and 15.2 cm diameter cold flow fluidized bed. Geldart type B glass bead, ground walnut shell, and crushed corncob particles were studied at various superficial gas velocities. Assuming axisymmetry, the local 3D time-average gas holdup data acquired through X-ray CT imaging was averaged over concentric annuli, resulting in a 2D annular and time-average gas holdup map. These gas holdup maps show that four different types of annular hydrodynamic structures occur in the fluidized beds of this study, zones of 1) aeration jetting, 2) bubble coalescence, 3) bubble rise, and 4) particle shear. Changes in superficial gas velocities, bed diameters, and bed material densities display changes in these zones. The 2D gas holdup maps provide a benchmark that can be used by computational fluid dynamic (CFD) users for direct comparisons of 2D models, assuming axisymmetric annular flow.

[3] Drake, J. B. and T. J. Heindel (2011). "Comparisons of annular hydrodynamic structures in 3D fluidized beds using X-ray CT." Journal of Fluids Engineering **In Review**.

6.2 Introduction

The advantageous properties of fluidized beds such as low-pressure drops, uniform temperature distributions, excellent gas-solid contacting for high heat and/or mass transfer rates, the accommodation of a wide range of particle properties, and the ability of handling limited quantities of liquids [1], entice many industries to use fluidized beds for processing purposes. For example, fluidized beds are key components in the manufacture of various intermediate and end-user products [2], such as gaseous and liquid fuels, commodity chemicals, and pharmaceuticals [3]. Furthermore, fluidized beds are quickly becoming the standard technology for small scale power generation (less than 25 MW) that is widely used in Europe, North America, and China, among other countries [4] for processing coal, biomass, and solid wastes through pyrolysis and gasification.

Some of the most daunting problems facing fluidized bed reactors in terms of process efficiencies are [5]: 1) the need for large gas throughputs requiring large reactor diameters and heights; 2) the addition of heat exchange systems for highly exothermic processes; 3) the location of feedstock and recirculated material injection ports; and 4) the need for injection of gas horizontally through reactor walls. When reduced to their most basic form, all of these problems are hydrodynamically dependent and related to the bubbling of gas through the bed material and around submerged and fixed structures in the bed, the bed geometry, and properties of the fluidizing gas and bed material. The hydrodynamic characterization of a fluidized bed requires a deep understanding of these dependencies, particularly in the design process when mistakes can become extremely expensive. In fact, system failures have been reported in commercial reactors designed from laboratory or pilot scale models due to hydrodynamic changes over reactor scale-up [6, 7].

Fluidized bed scale-up from laboratory or pilot scales to commercial scales comes with an understanding of the fluidized bed hydrodynamic behavior. Computational fluid dynamics (CFD), as a modeling tool, is increasingly being used to supplement the scale-up process. Although CFD is the standard for studying single-phase systems; it is still in the testing and validation stage for many multiphase systems. The use of CFD to model fluidized beds is highly dependent on boundary conditions and validation through experimentation. Deza et al. [8, 9] and Min et al. [10] have shown that X-ray visualization techniques can be used as a validation tool for fluidized bed hydrodynamic simulations.

Due to the nature of fluidized beds, hydrodynamic studies can be problematic at best and, at times, impossible. Invasive and noninvasive methods can be employed, however, noninvasive observation techniques are more reliable [11]. Techniques such as electrical capacitance [12], X-ray absorption [13], γ-ray absorption [14], or positron emission tomography [15] utilize field measurements (i.e., capacitance, absorption, transmission, etc.) to quantify local property variations. X-ray visualization has proven to be a useful and relatively inexpensive tool in providing good qualitative and quantitative data of dynamic behavior [16]. Successful measurements of time-average gas holdup have been made using these techniques [13, 17-20].

If the height above the aeration zone is sufficient, it can be assumed that the flow within the fluidized bed is annular and fluidization uniformity is axisymmetric [13]. With the assumption of axisymmetry, the data can be averaged over concentric annuli to produce 2D maps of the annular and time-average gas holdup. This paper employs this assumption and data analysis technique to identify hydrodynamic flow structures within two different fluidized beds filled with three different materials. The data provided by these 2D maps offer

a benchmark for CFD modelers to make direct comparisons to 2D CFD simulations that can then be extrapolated to a 3D bed when axisymmetry is assumed.

6.3 Experimental Setup

The fluidized bed reactors used in this study are non-reactive cold flow reactors. Their ID measurements are 10.2 cm and 15.2 cm, and made of transparent polyacrylic material allowing X-rays to pass through with little to no attenuation affects. The aeration scheme for each reactor uses a perforated plate that consists of uniformly distributed 1 mm diameter holes over a polar grid originating at the plate center for each reactor. The aeration plates for the 10.2 cm and 15.2 cm diameter reactors contain 62 and 131 perforations, respectively, providing open area ratios of 0.62% and 0.57%. Further details are provided in Drake and Heindel [13].

The three bed materials used in this study are Geldart type B particles [21] (glass beads, crushed walnut shell, and ground corncob) and were chosen based on their fluidization behavior, size range, density, aspect ratio, availability, and similarity to materials used in conventional inert fluidized bed systems. Glass beads are used as a reference material in this study and provide a benchmark for the fluidization behavior of various materials within both fluidized bed reactors. Table 1 provides a summary of the bed material properties used in this study.

To measure the bed weight and bulk density, each material is placed into either reactor and slightly fluidized to remove packing effects. Material is added or removed from the bed until a bed height of 1 reactor diameter is reached. The material is then removed from the reactor and weighed. The bulk density, ρ_b, for each bed is then calculated by

$$\rho_b = \frac{m_{bed}}{V_{bed}} \quad (1)$$

where m_{bed} is the bed mass and V_{bed} is the bed volume. The material density (ρ_p) was provided by the manufacturer. The bulk (static) void fraction for each bed is calculated by

$$\varepsilon_{g,b} = 1 - \frac{\rho_b}{\rho_p} \quad (2)$$

The minimum fluidization velocity (U_{mf}) of each bed is determined experimentally using the procedure described by Drake and Heindel [13]. Table 1 summarizes the minimum fluidization velocities and flow rates used for each material in each reactor. The superficial gas velocity (U_g) defined as the volumetric flow rate divided by the reactor cross-sectional area, is then referenced to the respective U_{mf} values.

Heindel et al. [22] have described the X-ray CT equipment used in this study and the specifics of the described-ray imaging used in this paper are found in Drake and Heindel [13, 19]. A summary of the equipment settings used to acquire the data for this study is provided in Table 6.1.

Table 6.1: Material properties, minimum fluidization, and equipment settings

		10.2 cm reactor			15.2 cm reactor		
		Glass Beads	Walnut Shell	Corncob	Glass Beads	Walnut Shell	Corncob
Material Properties							
D_p	[μm]	500-600	500-600	500-600	500-600	500-600	500-600
ρ_b	[kg/m^3]	1491	579	392	1500	570	395
m_{bed}	[g]	1220	477	323	4160	1580	1098
ρ_p	[kg/m^3]	2600	1200-1400	800-1200	2600	1200-1400	800-1200
$\varepsilon_{g,b}$	[-]	0.43	0.55	0.61	0.42	0.56	0.6
Minimum Fluidization Velocity and Flow Rate Conditions							
U_{mf}	[cm/s]	21.7	18.4	17.1	20.2	16.3	16.8
Q_{mf}	[L/min]	105.3	89.3	83.2	220.6	178.4	183.7
Equipment Settings							
Source Voltage	[keV]	150	130	130	160	139	139
Source Current	[mA]	3.5	3.2	3.2	4.5	3.9	3.9
CCD Exposure	[s]	1	1	1	1	1	1
CCD Temperature	[ºC]	0	0	0	0	0	0
Filters	[-]	1Al & 2Cu	1Al & 1Cu	1Al & 1Cu	1Al & 2Cu	1Al & 1Cu	1Al & 1Cu
Binning	[-]	4x4	4x4	4x4	4x4	4x4	4x4

Gas holdup or void fraction is defined as the volumetric gas fraction inside the bed, and the local time-average gas holdup, ε_g, is determined from [16]:

$$\varepsilon_g = \frac{I - I_b + (I_g - I)\varepsilon_{g,b}}{I_g - I_b} \tag{3}$$

were each variable I is the local X-ray CT value extracted from different X-ray CT images; these refer to a dynamic bed (I), a static bed (I_b), and an empty bed (I_g). Performing this calculation generates a new 3D file that contains the local time-average gas holdup map. Note that all values in Eq. (3), except for $\varepsilon_{g,b}$, have unique time-average values at every voxel (3D pixel). It is estimated that the absolute error in ε_g is ~ ±2%.

The newly generated 3D ε_g file consists of a rectangular matrix of voxels where each voxel is 450 μm on a side. A region of interest (ROI) is chosen within the 3D ε_g file that contains only the fluidized bed, excluding the reactor walls and aeration plate. Quantitative 2D contour maps are generated from analysis within this ROI. These maps display time-

average gas holdup (Eq. (3)) that is further averaged around concentric annuli to yield an averaged annular gas holdup, $\varepsilon_{g,r}$. Hence, each pixel within a $\varepsilon_{g,r}$ map represents the average ε_g value in an annulus at a particular height and radius incremented by one voxel in either the axial or radial directions (i.e., each annulus is 450 μm wide and 450 μm high). Defining which voxels fall within particular annuli is determined by rounding each voxel to the nearest integer annulus. For example, Fig. 6.1 shows a schematic (not to scale) of concentric circles superimposed on the perforated aeration plate of the 15.2 cm diameter reactor. The 10.2 cm reactor has fewer concentric circles because of the smaller diameter; however, in both reactors, concentric annuli encompass rings of aeration jets as shown in Fig. 6.1, allowing well-defined averages for the aeration jets in the $\varepsilon_{g,r}$ contour maps that are displayed in proceeding figures.

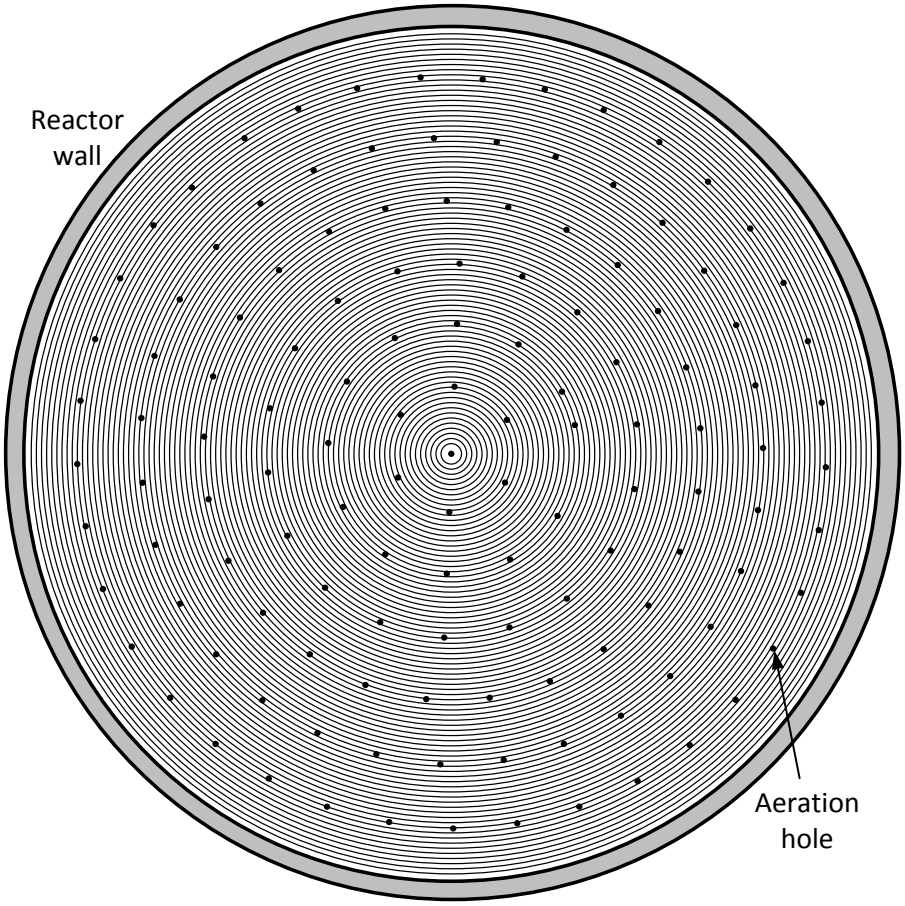

Figure 6.1: Schematic of annuli inscribed inside of the 15.2 cm reactor (not to scale).

Noise is introduced to the data in many ways when performing the annular averaging analysis technique discussed here. First, large density gradients create artifacts in reconstructed X-ray CTs, for a more detailed discussion of this phenomena see Franka [23]. Second, both the convolution method used to reconstruct X-ray CTs and the annular averaging methods used to create the 2D $\varepsilon_{g,r}$ surface maps intrinsically create noise. Both are founded on the same conceptual ideal that when averaging data, noise is reduced by increasing the sample size. Therefore, when calculating $\varepsilon_{g,r}$ from the ε_g map, as $r \rightarrow 0$, the number of voxels in the average decreases, increasing the noise. To overcome this problem, all voxels within the first three radii are averaged together, creating a 2.7 mm diameter core

of averaged data centered on the bed center. To further reduce the noise in the derived 2D $\varepsilon_{g,r}$ map, the data are smoothed using a curve fitting method both vertically over all radii and horizontally over every slice.

Figure 6.2 shows a plot of $\varepsilon_{g,r}$ as a function of height in a fluidized glass bead bed contained by the 15.2 cm diameter reactor with $U_g = 2U_{mf}$. This figure demonstrates how noise in the data is greatly increased as the number of voxels in the average decrease. Two distinct plots are shown for two annular averages of ε_g. The left plots show the noisier lower voxel count core and the right plots show a less noisy, higher voxel count annular average near the reactor wall. Both sets of plots include the smoothed data superimposed over the noisy data and observations show that the smoothed data follows the general trend of the noisy data. The amplification of the noise decreases as r increases as revealed in the outer annuli plot. Finally, the variations near the base of the bed are also influenced by the large material variations caused by the flange region; the smoothing routine also reduces this artifact.

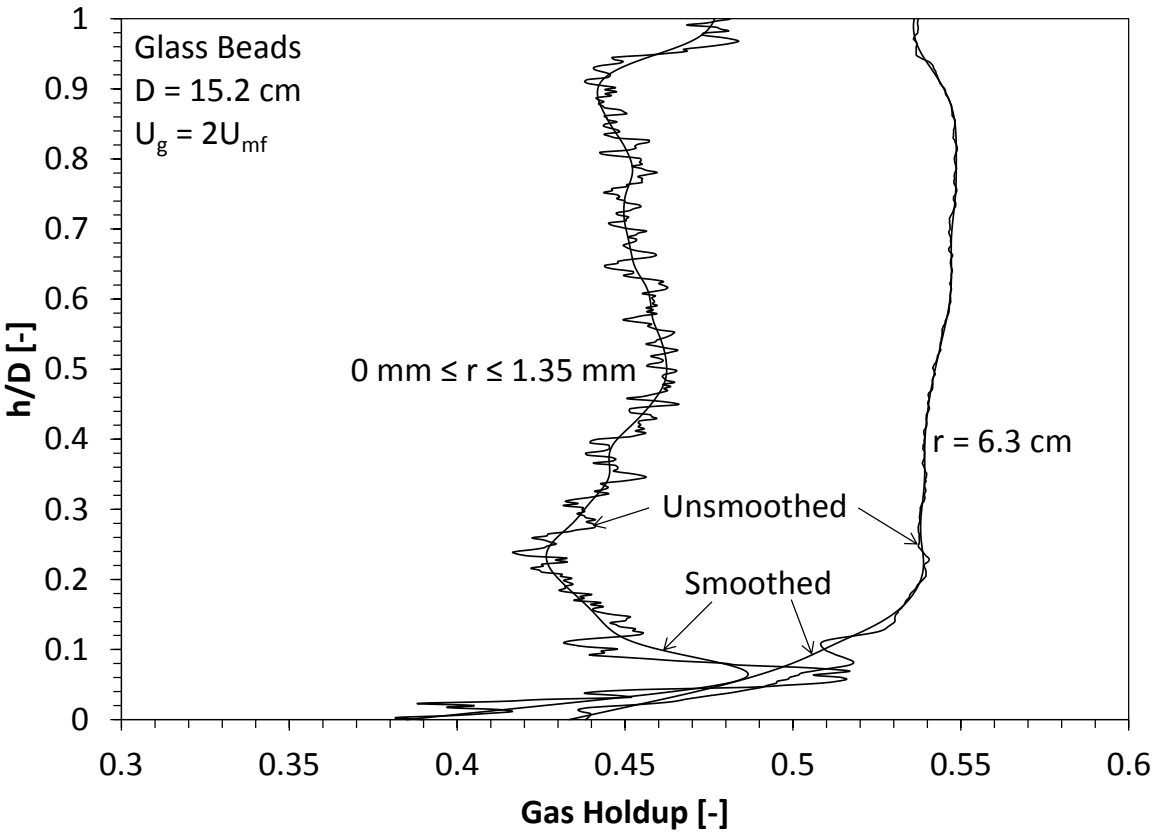

Figure 6.2: Comparison of smoothed and unsmoothed gas holdup data in the bed center and near the bed wall of a fluidized glass bead bed in the 15.2 cm diameter reactor with $U_g = 2U_{mf}$.

Each 2D surface plot of $\varepsilon_{g,r}$ that follow in the results section are dimensionally normalized both vertically and horizontally by h/D and r/R, respectively. The left edge of each map represents the reactor center, the right edge signifies the bed wall, and the bottom corresponds to the top of the aeration plate. Each image comparison includes a color scale showing $\varepsilon_{g,r}$ and are identical for all slices in a given material and reactor but differ between materials. Therefore, the color scales are modified to improve image resolution in the respective figures.

6.4 Results and Discussion

Local time-average gas holdup was determined for each bed diameter and material by acquiring a single test at various flow conditions. Previous work has shown that the data are repeatable [13]. Four superficial gas velocities ($U_g = 1.25U_{mf}$, $1.5U_{mf}$, $1.75U_{mf}$, and $2U_{mf}$) were chosen per material in each reactor. Results of $\varepsilon_{g,r}$ will be presented using glass beads as the reference material with the ground walnut shell and crushed corncob showing similar trends.

6.4.1 Effect of Bed Diameter on Gas Holdup

Figure 6.3 presents $\varepsilon_{g,r}$ contour maps for fluidized glass beads in both reactors at $U_g = 1.5U_{mf}$. The left and right maps display $\varepsilon_{g,r}$ in the 10.2 cm and 15.2 cm diameter beds, respectively. To simplify comparisons between geometries, $\varepsilon_{g,r}$ for both reactors is scaled over the same range found at the right of the figure. Note the difference in vertical scaling in Fig. 3 is due to the physical extent of the imaged regions; the 15.2 cm bed encompasses a larger physical domain but was slightly smaller than the 10.2 cm bed when nondimensionalized.

Figure 6.3 shows that the bed expansion is higher (in a dimensionless sense) in the smaller bed. This is due to a deeper penetration of frictional losses into the bed caused by larger wall effects in the smaller column. Therefore, the effective column diameter decreases causing local gas velocities to increase due to conservation laws. This leads to an increase in bed material momentum in the center of the bed, and ultimately, an increase in the time-average bed height.

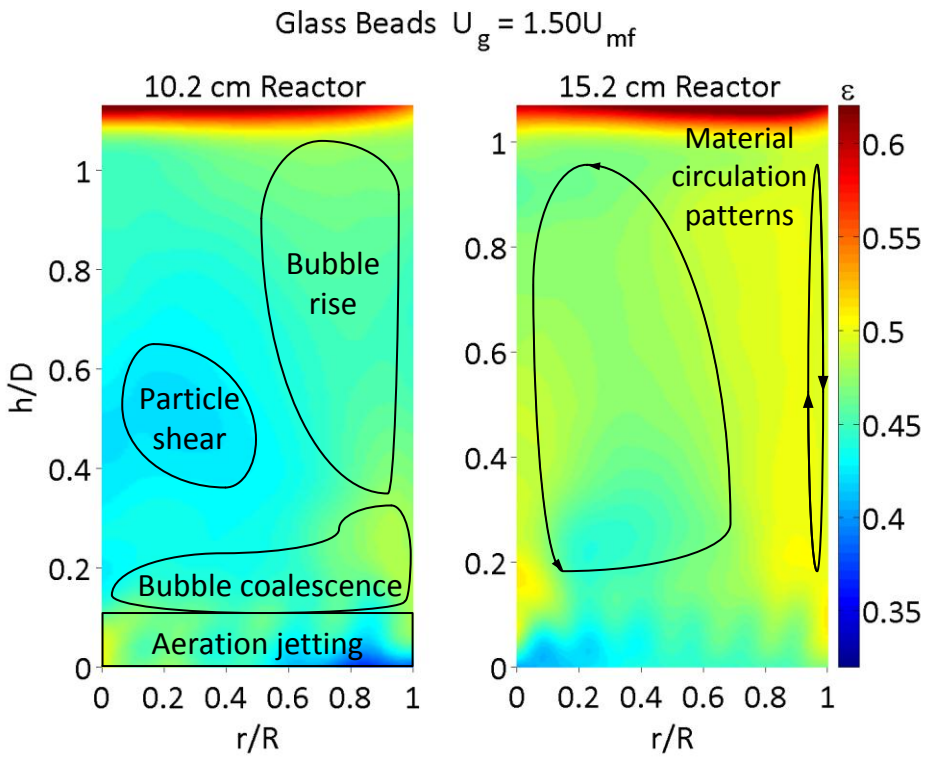

Figure 6.3: Local time-average annular gas holdup surface maps for fluidized glass bead bed in the (left) 10.2 cm diameter reactor and (right) 15.2 cm reactor at $U_g = 1.5U_{mf}$.

Although, it appears that $\varepsilon_{g,r}$ is fairly uniform across the bed in both reactors when $U_g = 1.5U_{mf}$ and h > 0.6D, some annular hydrodynamic structures do stand out. Four different prominent structures can be observed in both beds and have been defined as zones of 1) aeration jetting, 2) bubble coalescence, 3) bubble rise, and 4) particle shear. These structures are schematically shown in the 10.2 cm reactor although they appear in both reactors. The structures are hypothesized to change in shape, size, and location due to the aeration scheme chosen for fluidization (i.e., perforated plate, porous plate, etc.). Aeration jetting is identified by long, thin regions of relatively high $\varepsilon_{g,r}$ emanating from the bottom of the bed. The bubble coalescence zone is observed as a region of relative high $\varepsilon_{g,r}$ just above, and generally attached to, individual aeration jets; this zone is largest near the wall. The bubble rise zone is

a region of gradually widening plume of relatively high $\varepsilon_{g,r}$ emanating from the bubble coalescence zone, particularly near the wall. Areas of particle shear are identified by local regions of relatively low $\varepsilon_{g,r}$ in areas of the bed away from the aeration region. Time-average gas holdup values provided by 2D simulations of the same system made by Min et al. [10] show the same structures in the beds.

The aeration jets emanate from the concentric annuli containing the aeration plate perforations (Fig. 6.1). The jets tend to reach approximately the same height in both reactors, between 0.15D to 0.175D and have completely dissipated at heights of h = 0.2D. These jets tend to lean towards the reactor wall, which is indicative of a counter-clockwise circulation of bed material just above the aeration zone in both reactors. An interesting difference between bed diameters is that the jets become more prominent near the reactor center in the 10.2 cm reactor and less prominent near the reactor wall. This is opposite for the 15.2 cm reactor and is most likely due to wall effects affecting the bed material circulation near the reactor base.

Bubble coalescence occurs above the aeration region and is most prevalent near the wall. There is also a noticeable region near the center of the 15.2 cm bed. The location of these regions is most likely due to wall effects and is influenced by the circulation of the bed material. The bubble coalescence regions predominantly pull gas from nearby aeration jets while gas from relatively distant jets dissipates as interstitial gas.

Regions of bubble rise are similar between bed diameters near the reactor walls; however, a center rise path is also visible in the 15.2 cm reactor. Again, this is most likely due to the wall effects on the circulation patterns. Generally, bubble rise regions reach the top of the bed if they occur near the reactor wall. When they are found near the bed center

they tend to become widely dispersed throughout the bed and generally dissipate due to material falling in the central region of the bed. For both reactors, the bubble rise region originating near the wall penetrates almost to the bed center at the top of the bed, indicating the migration of large bubbles towards the bed center as they rise. A stark difference between rise paths is their prominence, where the intensity is greater in the 15.2 cm reactor than in the 10.2 cm reactor.

Regions of particle shear are identified by relatively low $\varepsilon_{g,r}$ where particle circulation is concentrated and particle-particle interaction is the greatest. The difference in particle shear zones between reactors is in their location and size. Two zones (reactor center and wall) appear and are shown for illustration purposes in the 15.2 cm reactor in Fig. 6.3, although they are found in both reactors. In the 10.2 cm reactor, the dense center zone is relatively large and is centered at approximately a height of h = 0.5D and a radius of r = 0.2R. The central zone in the 15.2 cm reactor is not as dense with a center of rotation at about h = 0.2D and r = 0.2R. The circulation direction for these zones is most likely in the counter-clockwise direction due to the wall leaning aeration jets and the rising gas near the wall. The wall zones are harder to identify in Fig. 6.3; however, visual observations of the beds reveal that material falls near the walls. Therefore, a bubble rise path near the walls implies particle rise in this region, creating a thin clock-wise particle circulation zone right along the entire height of the wall. This is observed in both reactors. This is confirmed by the decreasing $\varepsilon_{g,r}$ as $r \rightarrow R$. The circulation patterns observed in Fig. 6.3 are comparable to those made by Soria-Verdugo et al. [24] in a similar system.

Figure 6.4 displays plots of $\varepsilon_{g,r}$ of a fluidized glass bead bed in both reactors with $U_g = 1.5U_{mf}$ and h = 0.75D. Observations show that in both reactors, the bubble rise zone is

visible by the local maximum in gas holdup near the reactor wall, and the penetration depth is approximately the same. At h = 0.75D, there is a significant difference in $\varepsilon_{g,r}$ values between the two bed diameters, and is most likely due to wall effects causing slight changes in circulation patterns and gas rise through the bed. This follows the results observed by both Drake and Heindel [13, 19] and Franka and Heindel [18].

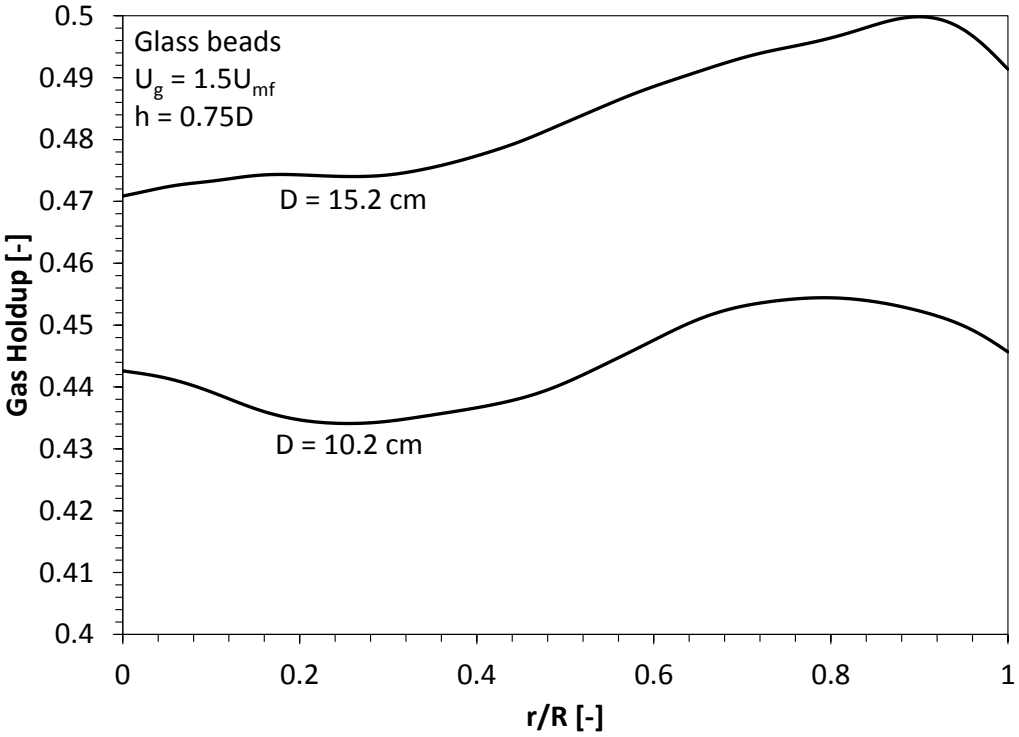

Figure 6.4: Radial $\varepsilon_{g,r}$ for a fluidized glass bead bed in the 10.2 cm and 15.2 cm diameter reactors with $U_g = 1.5U_{mf}$ at h = 0.75D.

6.4.2 Effect of Superficial Gas Velocity on Gas Holdup

Figure 6.5 presents $\varepsilon_{g,r}$ contour maps with increasing U_g left to right, top to bottom for fluidized glass beads in the 10.2 cm reactor. All contour maps are scaled over the same range to simplify comparisons between flow rates.

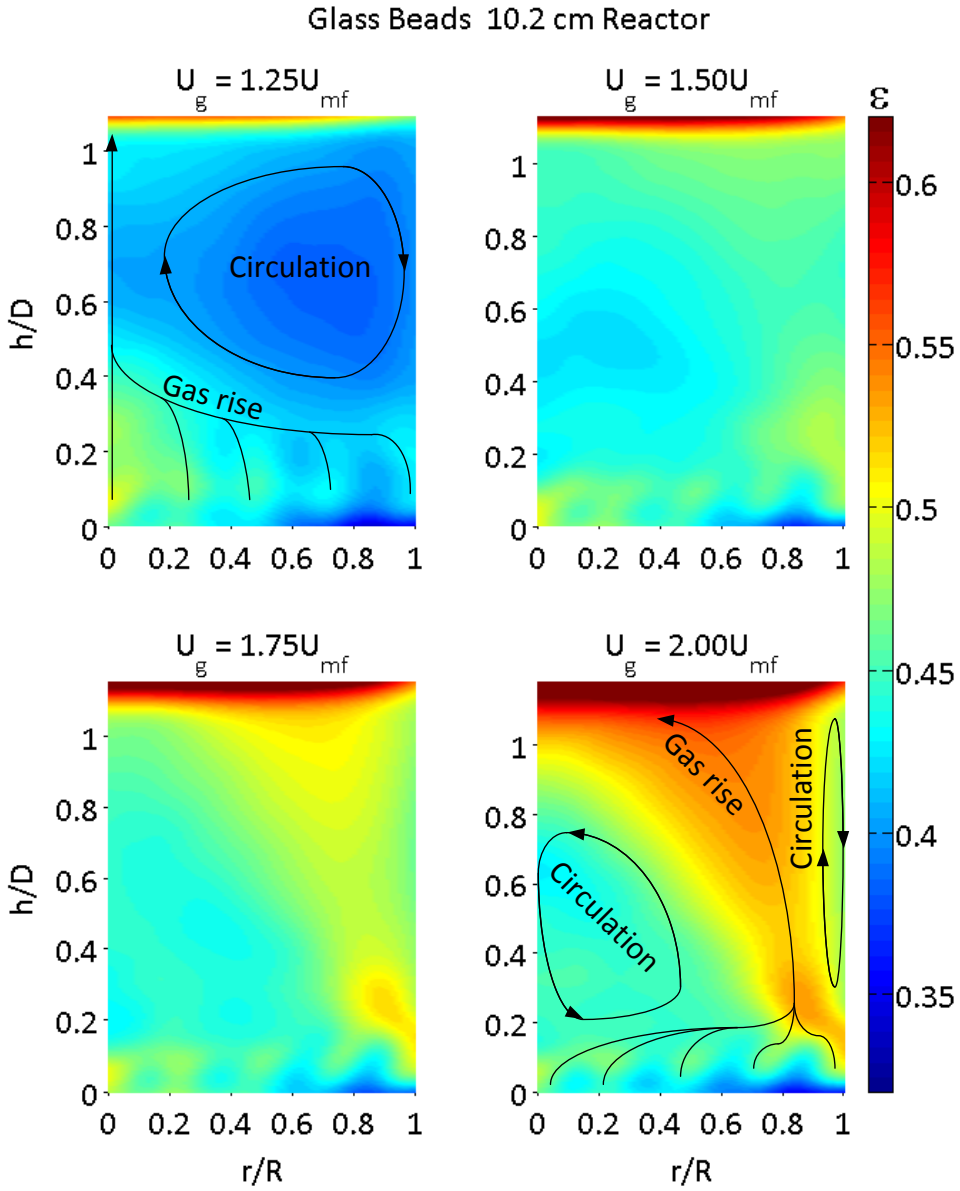

Figure 6.5: Local time-average annular gas holdup surface maps for fluidized glass bead beds in the 10.2 cm diameter reactor at (upper left) $U_g = 1.25U_{mf}$, (upper right) $U_g = 1.5U_mf$, (lower left) $U_g = 1.75U_{mf}$, and (lower left) $U_g = 2U_{mf}$.

Again, the same four annular hydrodynamic structures stand out in Fig. 6.5, although their size and location are influenced by U_g. As U_g increases, fluidization uniformity tends to decrease as mixing in the bed increases. This is due to the development of bubble rise paths near the reactor walls, which increase in width and intensity from enhanced mixing as U_g

increases. Note that when $U_g = 2U_{mf}$, the width of the bubble rise path at the top of the bed is equal to R, indicating that a taller bed would most likely have very uniform fluidization above h = 1D. As these rise paths increase in prominence with increasing U_g, the particle shear zone in the bed center tends to decrease in size and height while migrating from the reactor wall to the reactor center, forming a cone-like low gas holdup region. As stated previously, a second particle shear zone develops near the reactor wall and increases in prominence as U_g increases. In contrast to the $U_g = 2U_{mf}$, when $U_g = 1.25U_{mf}$ only one circulation zone appears to be present and is most likely in the clockwise direction, as can be inferred from the center leaning aeration jets. This assumption is further supported by the bubble coalescence region in the bed center, showing that relatively large amounts of gas pass there and not at the wall. As U_g increases, observations show the wall leaning aeration jets and absent bed centered coalescence zone, indicating the separation of the single particle shear zone into two opposing circulation patterns.

Figure 6.6 shows $\varepsilon_{g,r}$ countour maps with increasing U_g for fluidized glass beads in the 15.2 cm reactor. Again, observations show much of the same trends as seen in the 10.2 cm reactor. One difference is the size of the particle shear zone and the gas rise pattern when $U_g = 1.25U_{mf}$. This is most likely due to a decrease in the wall effects with an increased bed diameter allowing for better mixing quality at lower flow rates. Another difference is the decrease in bubble rise path penetration depth. Lastly, a clear development of the wall circulation pattern is not as apparent in the larger reactor, although visual observations confirm downward particle motion at the walls.

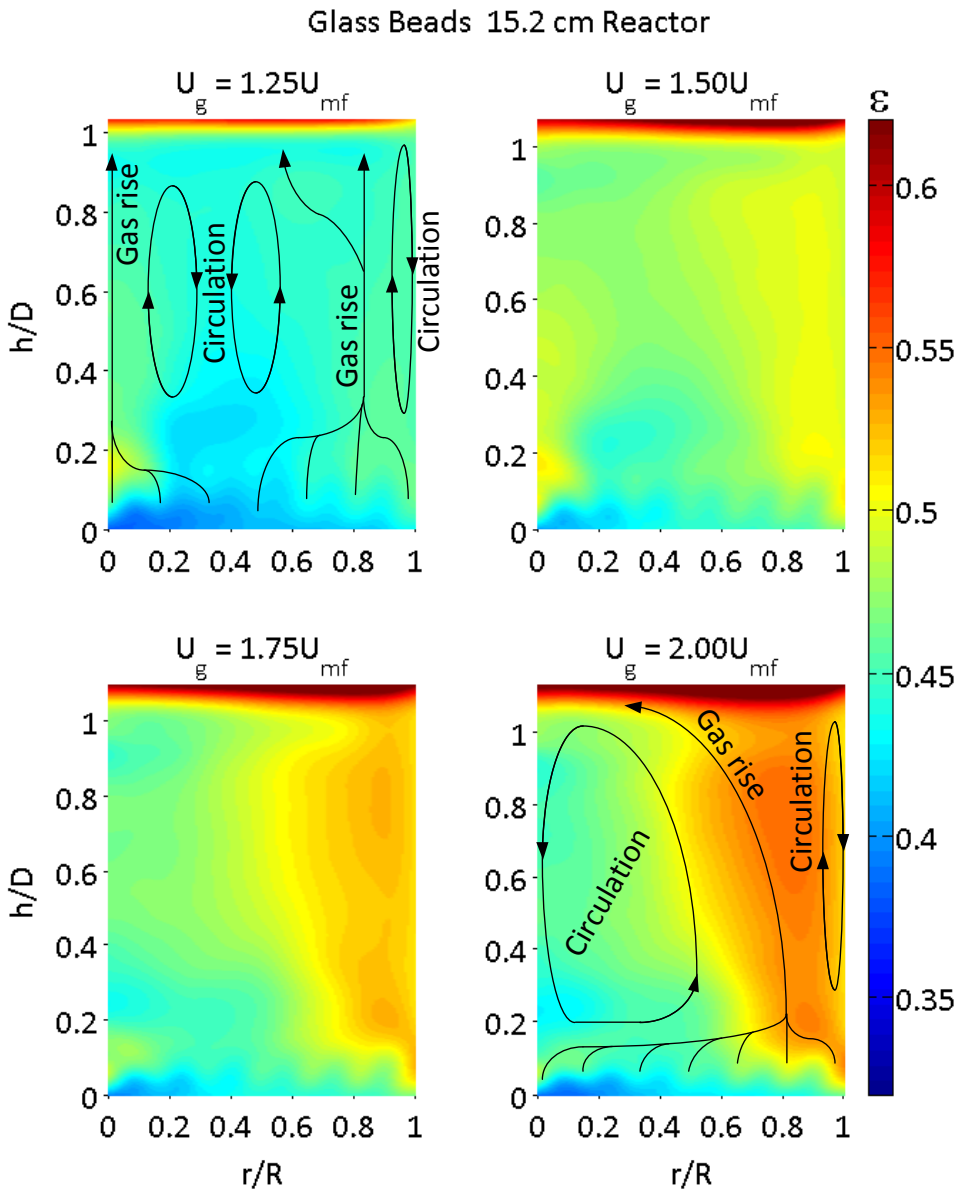

Figure 6.6: Local time-average annular gas holdup surface maps for fluidized glass bead beds in the 15.2 cm diameter reactor at (upper left) $U_g = 1.25U_{mf}$, (upper right) $U_g = 1.5U_{mf}$, (lower left) $U_g = 1.75U_{mf}$, and (lower left) $U_g = 2U_{mf}$.

Figure 6.7 shows how the bubble rise zone and wall circulation region evolves as U_g increases in both fluidized beds at a fixed dimensionless height. The bubble rise region penetration depth and $\varepsilon_{g,r}$ increase as U_g increases in both reactors. The appearance of a

prominent local maximum in $\varepsilon_{g,r}$ as U_g increases implies the wall circulation region increases as U_g increases; the circulation region is smaller (in a dimensionless sense) for the larger bed diameter. The width can be estimated by the radial location of the maximum $\varepsilon_{g,r}$ value within the bubble rise zone for each reactor. As U_g increases, this maximum migrates further away from the reactor wall, indicating an increasing circulation region; however, as bed diameter increases, the maximum $\varepsilon_{g,r}$ migration decreases or is not as far away from the reactor wall at all U_g. This is mainly due to increasing wall effects with decreasing reactor diameter.

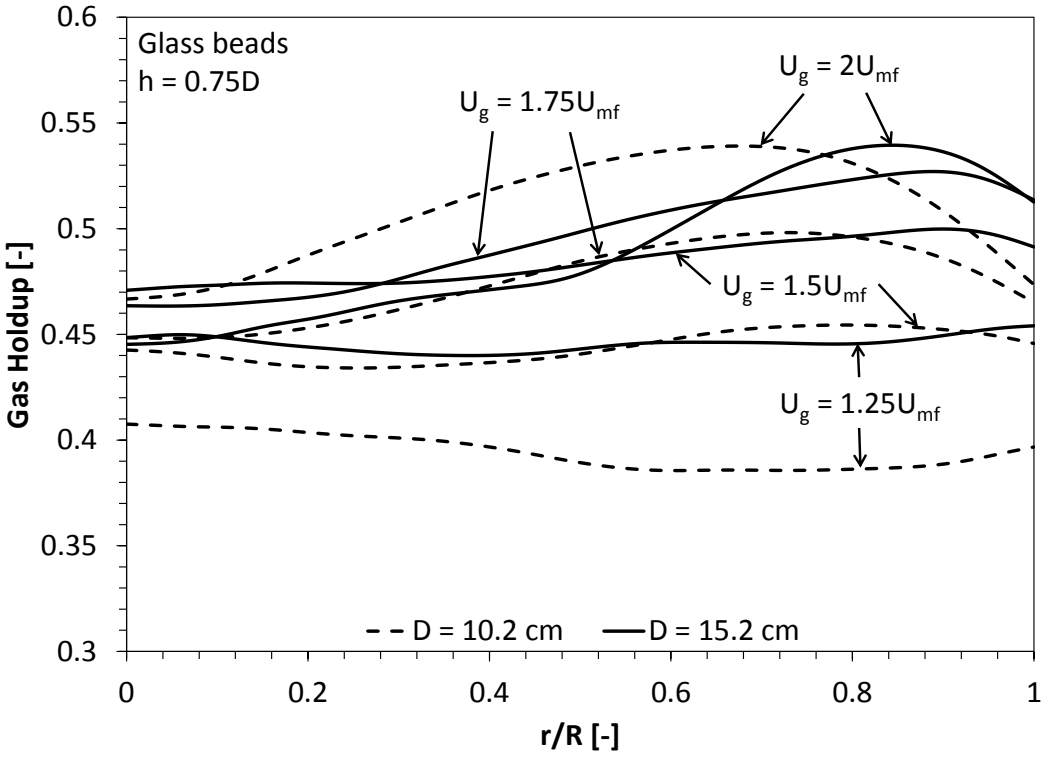

Figure 6.7: Radial $\varepsilon_{g,r}$ for a fluidized glass bead bed in the 10.2 cm and 15.2 cm diameter reactor with $U_g = 1.25U_{mf}$, $1.5U_{mf}$, $1.75U_{mf}$, and $2U_{mf}$ at h = 0.75D.

Figure 6.8, shows how the bubble rise zone and wall circulation region evolve, as the bed height increases for $U_g = 2U_{mf}$. The lower gas holdup near the wall is a clear indication of particle circulation in this region. The growth in penetration region as height increases is

clearly observed in the 10.2 cm reactor. In contrast, the penetration region as height increases only grows a small amount with increasing height in the 15.2 cm bed. These profiles are comparable to those observed by Paaneerselvam et al. [25] in CFD simulations of a gas-liquid-solid fluidized bed of glass beads, water, and air, showing that these results can be extrapolated to three phase systems as well.

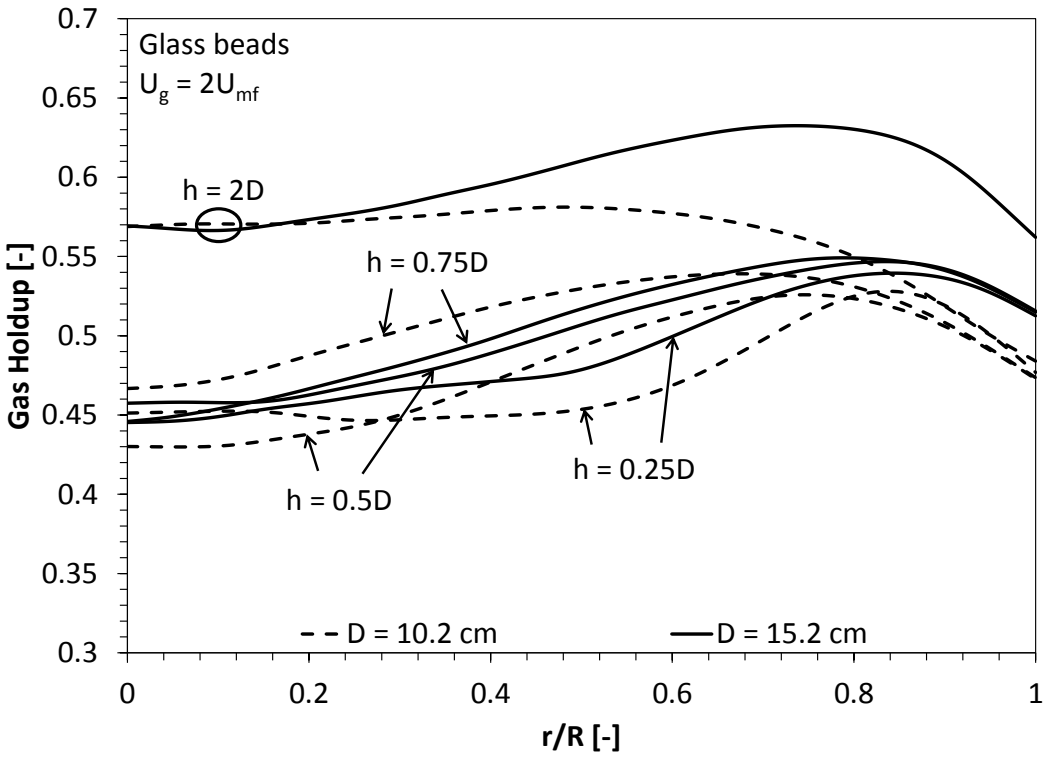

Figure 6.8: Radial $\varepsilon_{g,r}$ for a fluidized glass bead bed in the 10.2 cm and 15.2 cm diameter reactor with $U_g = 2U_{mf}$ at h = 0.25D, 0.5D, 0.75D, and D.

6.4.3 Effect of Bed Material Density on Gas Holdup

Figure 6.9 displays $\varepsilon_{g,r}$ surface maps of fluidized beds with increasing bed material density from left to right in the 10.2 cm reactor at $U_g = 1.5U_{mf}$. All surface maps are scaled over different ranges where each range is centered on the bulk holdup value to simplify comparisons between densities.

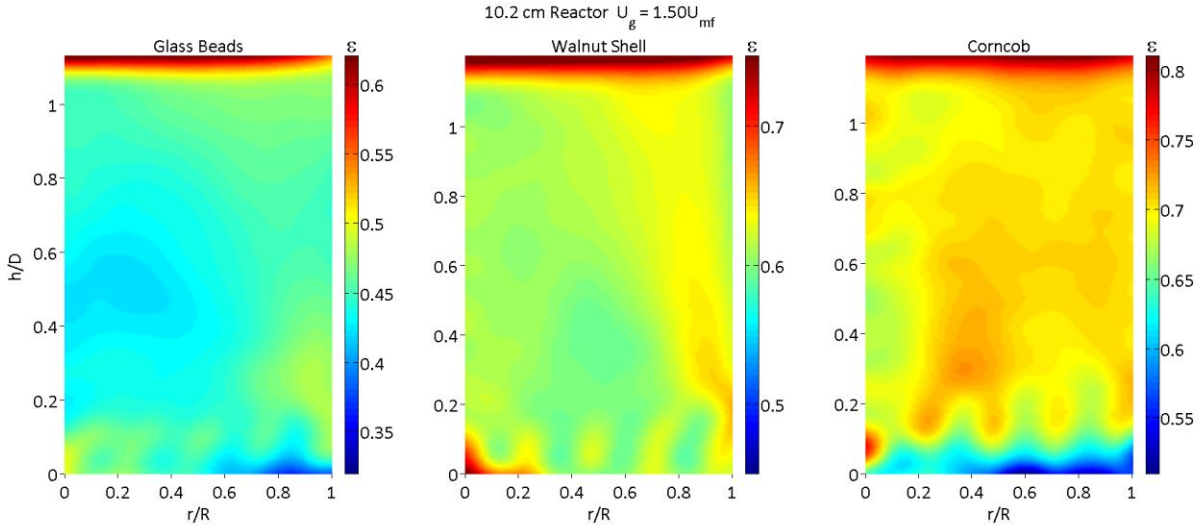

Figure 6.9: Local time-average annular gas holdup surface maps for fluidized beds of increasing density in the 10.2 cm reactor at $U_g = 1.5U_{mf}$.

All three beds show $\varepsilon_{g,r}$ variations in different regions of the bed. Bubble rise paths near the reactor wall are identifiable in the glass bead bed, apparent in the ground walnut shell bed, and absent in the crushed corncob bed. The crushed corncob has the smallest density of the three materials in this study. The low density promotes bed mixing, and at $U_g = 1.5U_{mf}$, distinct bubble rise paths are not observed. In addition to material density, it is hypothesized that these observations are also influenced by particle-particle interaction and material properties such as shape factor, coefficient of restitution, and porosity.

Bubble coalescence zones in beds of glass beads and ground walnut shell appear to be similar with a focus near the wall; however, crushed corncob shows a different pattern. The main coalescence zone in crushed corncob is centered around r = 0.4R and h = 0.3D. The main reason for this difference is the bed of crushed corncob is less dense, which promotes enhanced mixing, reducing regions of relatively low gas holdup, as observed in glass bead and ground walnut shell beds. For all three materials, these zones tend to be fed by two

adjacent concentric aeration jetting circles, where all other jets tend to disperse as interstitial gas.

Figure 6.10 shows $\varepsilon_{g,r}$ surface maps of fluidized beds with increasing bed material density from left to right in the 10.2 cm reactor at $U_g = 2U_{mf}$. The ground walnut and crushed corncob shell beds show an increase of $\varepsilon_{g,r}$ throughout the bed with increasing U_g. The glass bead bed displays an increase in the bubble rise path. The particle shear zone shows a large region of relatively low $\varepsilon_{g,r}$ more typical of values near incipient fluidization. This is most likely due to the increased density and uniform shape of the glass beads compared to the ground walnut shell and crushed corncob particles.

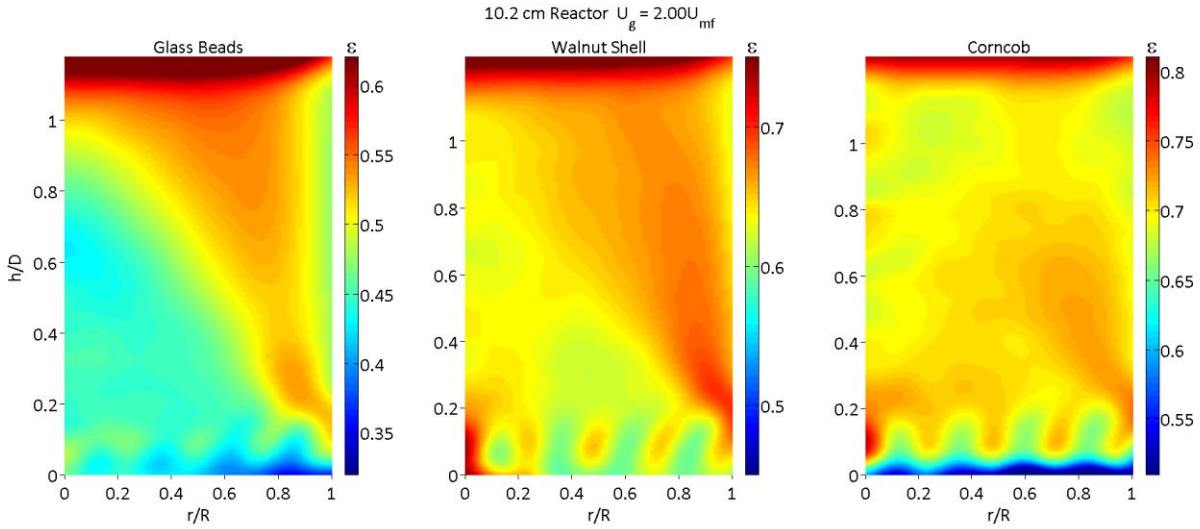

Figure 6.10: Local time-average annular gas holdup surface maps for fluidized beds of increasing density in the 10.2 cm reactor at $U_g = 2U_{mf}$.

The bubble coalescence zones and rise paths in each material occur in the same locations, but increase in size as expected with increased U_g. The location and size of particle shearing zones change with increasing U_g. The glass bead bed shows the particle

shearing zone decreases in size and the low gas holdup center migrates higher in the bed. In the ground walnut shell bed, the low gas holdup shear zone decreases in size and is still centered near the same location. The upper zone in the crushed corncob bed did not change in shape or location; however, it did increase in size. The lower zone decreased in size and an increase of downward flowing material at the reactor wall developed. Aeration jets do not appear to change with increasing U_g except for a more defined jetting region, which is expected.

Figure 6.11 shows how the bubble rise zone and wall circulation region evolves as bed material density changes in both fluidized beds at a fixed height of h = 0.75D and superficial gas velocity of $U_g = 2U_{mf}$. The depth of bed penetration across the bubble rise zone and the prominence of the wall circulation region appear to increase slightly as material density increases in both reactors. If the radial location of the maximum $\varepsilon_{g,r}$ is an indicator of the width of the wall circulation region, then the width increases as bed diameter decreases. Again, this is due to increasing wall effects with decreasing reactor diameter. Furthermore, a maximum $\varepsilon_{g,r}$ is not as apparent in the crushed corncob beds due to the enhanced mixing this low density material promotes.

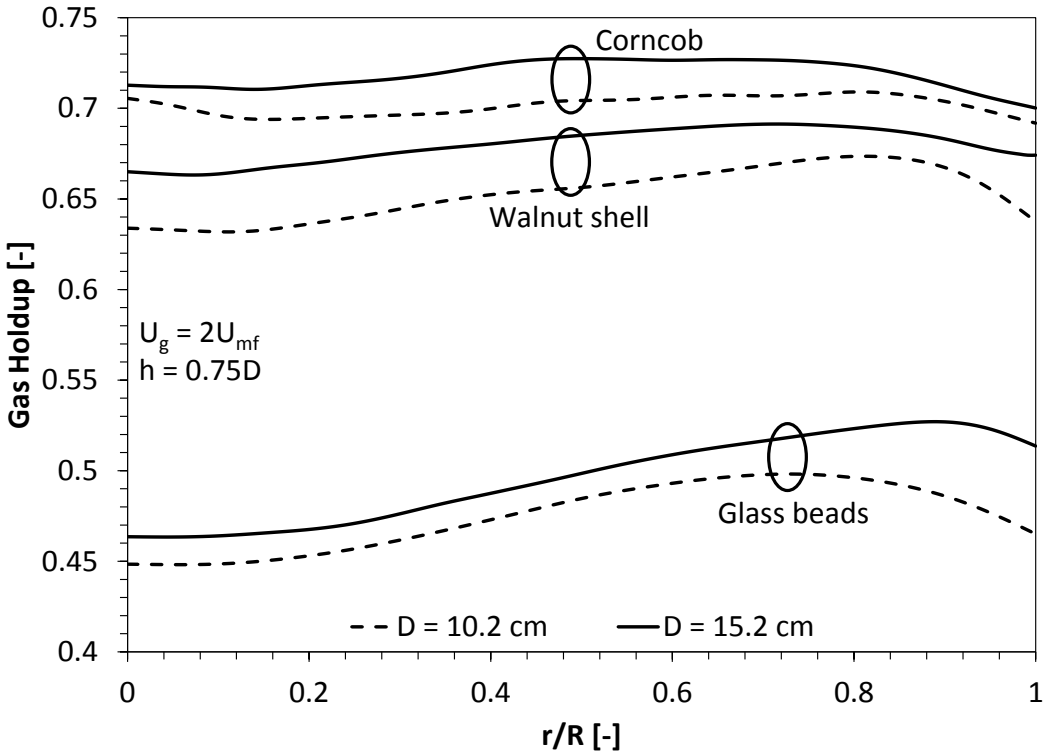

Figure 6.11: Radial $\varepsilon_{g,r}$ for a fluidized bed of glass beads, ground walnut shell, and crushed corncob in the 10.2 cm and 15.2 cm diameter reactor with $U_g = 2U_{mf}$ at h = 0.75D.

6.4.4 Conclusions

The effects of fluidization velocity, material density, and bed diameter on the annular hydrodynamic structures and local annular and time-average gas holdup were investigated in this study. The results show that four different annular hydrodynamic structures occur in the dynamic fluidized beds used in this study, and include zones of 1) aeration jetting, 2) bubble coalescence, 3) bubble rise, and 4) particle shear. Changes in the shape, size, and location of these zones occur with changes in U_g, bed diameter, and bed material density. It is also hypothesized that the aeration scheme of the bed and the bed material properties (i.e., shape factor and coefficients of restitution) may play a role in the development of these structures;

this area is in need of further investigation. These experimental conclusions are of great importance to modeling of multiphase systems. By assuming that aeration is uniform, fluidization is homogeneous, and the flow is axisymmetric, direct comparisons of 2D CFD models can be made to these experimental results of local time-averaged annular gas holdup values derived from X-ray CT imaging techniques.

CHAPTER 7 CONCLUSIONS AND FUTURE WORK

Equation Chapter 7 Section 1

7.1 Conclusions

As processing tools, fluidized beds are key components in many industrial sectors. The wide use of fluidized beds in power generation alone is enough to commission many highly specific studies of fluidized beds. One in particular would be how to increase the efficiency of energy conversion through gasification, pyrolysis, or combustion? The specifics regarding the previous question fall soundly within the realm of the physical; therefore, to understand the phenomenon of gasification, pyrolysis, and combustion, a thorough understanding of the hydrodynamics must be obtained. This study helps to do just that in showing how the hydrodynamics change between two reactors of different ID's with varying bed material densities and flow conditions.

7.1.1 Repeatability and Uniformity of Gas Holdup

Determining ε_g using the method described in chapter 3 is shown to be highly repeatable. Both ground walnut shell and glass beads over five different tests on different days showed high repeatability in the 15.2 cm reactor. When ε_g was analyzed as a function of height, all data fell within 0.1 standard deviations of each other. Moreover, data extracted at different azimuthal locations showed that uniformity within the bed is highly dependent on the bed height, gas flow rate, and reactor geometry. Hydrodynamic structures such as jetting occurred near the aeration region. As gas flow rate increased, jetting tended to decrease due to increased mixing of the bed and resulted in more axi-symmetric flow. Lastly, slight

variations in reactor geometry created variations in the flow conditions that persisted well beyond the variation.

7.1.2 Local Time-Average Gas Holdup Comparisons

The local time-average gas holdup, ε_g, within the bed is affected by changes in U_g, Q_s, bed material density, and jetting or the aeration scheme. More specifically, overall ε_g increases with increased U_g, Q_s, and decreased material density but does not change with increased reactor size, due to increased mixing. Furthermore, overall ε_g is affected by jetting, where jet size and length appear to decrease with increasing U_g, again due to increased mixing. However, this does not seem to be the case with increasing Q_s though. Material density effects increase mixing in the bed due to the decreased amount of energy needed to move the bed particles, which is evident in both reactors.

The only significant changes in overall ε_g due to changes in reactor size are from differences in hydrodynamic structures and average bed heights. In the 10.2 cm reactor, bubble coalescence begins at the walls just above the aeration jets, then as the bubbles rise they migrate towards the reactor center. Although bubble coalescence occurred in a similar fashion in the 15.2 cm reactor, the bubbles migrated only a short distance into the bed as they rose adjacent to the reactor walls. In terms of average bed height, the 10.2 cm reactor had a higher average bed height compared to the 15.2 cm reactor. Both circulation pattern and average bed height differences are due to major losses from wall effects, where more energy is required to fluidize the bed in the smaller reactor because of greater frictional losses compared to bulk flow effects with a smaller diameter.

7.1.3 Annular Hydrodynamic Structure Comparisons

By assuming that aeration is uniform, fluidization is homogeneous, and flow is annular, direct comparisons of 2D CFD models can be made with experimental results of local time-averaged annular gas holdup values derived from X-ray CT techniques. The results of this study show that four different types of annular hydrodynamic structures that occur in dynamic fluidized beds, zones of 1) aeration jetting, 2) bubble coalescence, 3) bubble rise paths, and 4) particle shear. Changes in the shape, size, number, and location occur with changes in U_g, bed diameter, and bed material density. It is also suspected that the aeration scheme of the bed and the bed material properties i.e. shape factor, coefficients of restitution, and porosity play a role in the development of these structures. These conclusions are of great importance to modeling of multiphase systems by showing how boundary conditions and system properties can change the hydrodynamics within the system.

7.2 Future Work

The large amount of waste biomass available and the need to decrease greenhouse gas production increasingly makes gasification an important processing method (Cui and Grace 2007). Moreover, the application of electrical generation by combustion of gasified products addresses the increased demand for alternative energies by both societal and legislative pressures (Brown 2003). The recent popularity increase of the gasification process demands efficiency improvements through experimentation, in which CFD models can be validated. These validated models can then be used to potentially enhance gasification efficiencies. Experimentally tracking biomass particles are limited and the need for high quality experimental data for validation of these simulations must be met.

The experimental limitations arise from the monitoring of biomass as it is injected into a fluidized bed, the reaction of biomass and its volatilization after being injected, the visualization of the gasification process, and the effects of gas injection as biomass enters the reactor through the injector port. A few of these limitations have been addressed in detail by Drake et al. (2009) while using the XFloViz facility at Iowa State University for this work. Details regarding future experiments that address some of these limitations will be given in the following two subsections: first, X-ray particle tracking velocimetry, and second, X-ray bubble tracking velocimetry.

7.2.1 X-ray Particle Tracking Velocimetry (XPTV)

The interactions between a large biomass particle and a dynamic fluidized bed are not well characterized for the gasification process. Future experimentation using the developed X-ray particle tracking velocimetry method explained by Drake et al. (2009) will help to characterize these interactions. A larger study of this method with both the 10.2 cm and 15.2 cm ID reactors filled with the glass bead material used in this study will show similarities between interactions in different geometries. Tests would be conducted in the same fashion as the gas holdup tests described in chapter 3 and a tracer particle would be manufactured specifically for the glass bead bed material. The tracer particle manufacturing of the has been explained by Drake et al. (2011).

There are some possible problems that could arise during this study. The cameras may not be able to capture adequate images of the tracer particle movement at high superficial gas velocities. The tracer particle's velocity increases with U_g, making it increasingly difficult to capture an image of the particle in a stationary position at the time of

exposure, which increases particle detection error. To decrease this error, the camera exposure time must be decreased, meaning less light is captured by the camera creating an underdeveloped image. Increasing the X-ray energy emitted by the source would increase the amount of light captured by the camera; however, this increasingly saturates the image and results in decreased image quality. On the other hand, if U_g is too low, then the particle will fall to bottom of the bed and become trapped between jets from the aeration plate making it impossible to be dynamic within the bed. Moreover, if Q_s is too low, the particle will not even enter the bed from the particle injection system because of the lack of momentum to overcome the bed material blocking the injector.

The behavior of the tracer particle is expected to follow the trends discussed by Drake et al. (2009). Expanding on this, the tracer particle should follow the dominant bubble rise paths vertically through the bed and fall with the dominant bed material recirculation paths or around particle shear zones. These patterns and paths will be developed through many trials where the overall movement patterns of the tracer particle will be found.

7.2.2 X-ray Bubble Tracking Velocimetry (XBTV)

The tracer particle interactions with the bed occur through fluidization by a gas. The interaction that the gas has with the bed material is important when trying to characterize the tracer particle's behavior in the fluidized bed. Therefore, an understanding of how the gas moves through the bed is important in knowing how the gas affects the tracer particle's movement in the bed. The results shown in chapter 6 are only of averaged local time-average annular gas holdup data, where only the dominant paths that the gas travels through the bed are revealed. The gas moving through these paths is assumed to be in the form of

bubbles, which would be confirmed if a method to track bubbles in a fluidized bed was developed and used in conjunction with the developed XPTV method. Other advantages of an XBTV method are: instantaneous localized ε_g within the bed, the process of bubble coalescence and at what heights in the bed this takes place, and dominant bubble sizes in differing material densities and flow conditions.

To track bubbles, a similar method would be employed as is with the XPTV method. Tests would be completed in both reactors, with all three bed materials, and at the same flow conditions used in the gas holdup tests given in chapter 3. Stereographic images of a dynamic fluidized bed would be taken and analyzed to locate and track bubble centroids, volumes, and velocities as they rise through the bed. Bubbles are identified in each image by using a surface thresholding method that identifies gray scale gradients indicating the bubble surface. Once the bubble surface is identified, the centroid is calculated and compared to the centroids of bubbles located in the respective perpendicular image taken at the same time. If the centroids match the same heights and follow the predicted path, then the bubble is matched in each image. As the bubble rises in the bed, its centroid should not vary more than a few degrees from a specified path, depending on U_g. The bubbles are then reconstructed in a virtual 3D bed where the surface is extrapolated from the known surfaces found in the perpendicular images by revolution, assuming a uniform and continuous deformation of the bubble. Bubble volumes are then calculated to find instantaneous ε_g in the bed, which is superimposed in the virtual bed with all images. This is then compared to the time-average values found and reported in chapter 6, as a verification method. The changes in bubble volumes as they rise through the bed give coalescence data for differing geometries, material densities, and flow conditions.

The potential problems with this method are similar to those experienced with the XPTV method. Eventually, as the flow conditions are varied, bubbles will begin to rise faster than the cameras in the XFloViz facility will be able to capture. However, a more insidious problem is the occurrence of bubble overlap, where one bubble either partially or completely covers another in one or both images. Furthermore, the assumptions needed to reconstruct virtual bubbles could be poor. These problems would cause potentially large errors in calculations of instantaneous ε_g, enough to make this method incomparable to the time-average data given in chapter 6.

The results of this study are expected to show that as the bubbles rise farther in the bed, their size will increase, due to coalescence with other bubbles. Therefore, bubble population higher in the bed will decrease. The zones in which bubble coalescence occurs should decrease with height as U_g increases, due to increased mixing. Lastly, the dominant bubble rise paths should follow the same trends that are reported in chapter 6.

ACKNOWLEDGEMENTS

I would like to thank my major professor, Dr. Theodore Heindel, for giving me a research opportunity in the experimental multiphase flow laboratory at Iowa State University. As a mentor, Dr. Heindel gave me invaluable advice and support that I will always be grateful for and rely on in my professional career. I would also like to thank my committee, Dr. Hui Hu, Dr. Ron Nelson, Dr. Michael Olsen, and Dr. Shankar Subramaniam for reviewing my work and thesis. Lastly, I would like to thank Nathan Franka for his help in working with me and providing some of the data used in this study.

The initial support for this study was provided by Conoco-Philips and the X-ray facility was funded by the National Science Foundation under award number CTS-0216367.

REFERENCES

Adamczyk, A. A. and L. Rimai (1988). "Reconstruction of a 3-dimensional flow field from orthogonal views of seed track video images." Experiments in Fluids **6**(6): 380-386.

ASTM (1997). Standard Guide for Computed Tomography (CT) Imaging. Philadelphia, ASTM.

Basu, P. (2006). Combustion and gasification in fluidized beds. Boca Raton, CRC/Taylor & Francis.

Boerefijn, R., M. Poletto and P. Salatino (1999). "Analysis of the dynamics of heat transfer between a hot wire probe and gas fluidized beds." Powder Technology **102**(1): 53-63.

Brown, R. C. (1997). ME 539: fluidized bed processes. Course Notes for ME539/ChE539. Ames, IA, Iowa State University.

Brown, R. C. (2003). Biorenewable Resources Engineering New Products from Agriculture. Ames, IA, Blackwell Publishing.

Bukur, D. B., J. G. Daly and S. A. Patel (1996). "Application of γ-ray attenuation for measurement of gas holdups and flow regime transitions in bubble columns." Industrial & Engineering Chemistry Research **35**(1): 70-80.

Chaouki, J., F. Larachi and M. P. Dudukovic (1997). "Noninvasive tomographic and velocimetric monitoring of multiphase flows." Industrial & Engineering Chemistry Research **36**(11): 4476-4503.

Chaouki, J., F. Laradhi and M. P. Dudukovic, Eds. (1997). Non-Invasive Monitoring of Multiphase Flows. Amsterdam, Netherlands, Elsevier Science B.V.

Cheng, D.-C. and H. Burkhardt (2003). "Bubble tracking in image sequences." International Journal of Thermal Sciences **42**(7): 647-655.

Cheremisinoff, N. P. (1986). "Review of experimental methods for studying the hydrodynamics of gas-solid fluidized beds." Industrial & Engineering Chemistry, Process Design and Development **25**(2): 329-351.

Clark, K. N. and N. R. Foster (1987). "Application of neutron techniques to studies of reactor fluid dynamics." Chemical Engineering Journal **34**(1): 35-46.

Clark, N. N. and R. L. Flemmer (1985). "Predicting the holdup in two-phase bubble upflow and downflow using the zuber and findlay drift-flux model." AIChE Journal **31**(3): 500-503.

Clift, R., J. R. Grace and M. E. Weber (1978). Bubbles, drops, and particles. New York, Academic Press.

Collins, R. (1965). "The rise velocity of Davidson's fluidization bubble." Chemical Engineering Science **20**(8): 788-790.

Cowen, E. A. and S. G. Monismith (1997). "A hybrid digital particle tracking velocimetry technique." Experiments in Fluids **22**(3): 199-211.

Crowe, C. T. and E. E. Michaelides (2006). Basic concepts and definitions. Multiphase Flow Handbook. C. T. Crowe. Boca Raton, FL, CRC Press**:** 1.1-1.79.

Cui, H. and J. R. Grace (2007). "Fluidization of biomass particles: A review of experimental multiphase flow aspects." Chemical Engineering Science **62**(1-2): 45-55.

Davidson, J. F. (1961). "Discussion following symposium on fluidization." Transactions of The Institution of Chemical Engineers(39): 230-232.

Davidson, J. F. and D. Harrison (1963). Fluidised Particles. London, NW, Cambridge, University Press.

De Lasa, H., S. L. P. Lee and M. A. Bergougnou (1984). "Bubble measurement in three-phase fluidized beds using a u-shaped optical fiber." Canadian Journal of Chemical Engineering **62**(2): 165-169.

Dechsiri, C., A. Ghione, F. Van De Wiel, H. G. Dehling, A. M. J. Paans and A. C. Hoffmann (2005). "Positron emission tomography applied to fluidization engineering." Canadian Journal of Chemical Engineering **83**(1): 88-96.

Deckwer, W. D., Y. Lousi, A. AZaidi and Ralek (1980). "Hydrodynamic properties of the Fischer-Tropsch slurry process." Industrial & Engineering Chemistry Process Design and Development **19**: 699-708.

Delhaye, J. M. (1969). "Hot-film anemometry in two- phase flow." (Compendex): 58-69.

Delhaye, J. M., R. Semeria and J. C. Flamand (1973). "Void fraction and vapor and liquid temperatures: local measurements in two-phase flow using a microthermocouple." Journal of Heat Transfer **95 Ser C**(3).

Dencs, B. (1996). "Local particle velocity and hydrodynamic features measurements in mechanically agitated fluidized beds." Hungarian Journal of Industrial Chemistry **24**(3): 235-240.

Deng, R., F. Wei, Y. Jin and Q. Zhang (2002). "Downer catalytic pyrolysis (DCP): A novel process for light olefins production." Chemical Engineering and Technology **25**(7): 711-716.

Deza, M., F. Battaglia and T. J. Heindel (2011). "Effects of mixing using side port air injection on a biomass fluidized bed." Journal of Fluids Engineering **In Print**.

Deza, M., N. P. Franka, T. J. Heindel and F. Battaglia (2009). "CFD modeling and x-ray imaging of biomass in a fluidized bed." Journal of Fluids Engineering, Transactions of the ASME **131**(Compendex): 1113031-11130311.

Deza, M., N. P. Franka, T. J. Heindel and F. Battaglia (2009). "CFD modeling and x-ray imaging of biomass in a fluidized bed." Journal of Fluids Engineering, Transactions of the ASME **131**(11): 1113031-11130311.

Drake, J. B., N. P. Franka and T. J. Heindel (2008). X-ray particle tracking velocimetry for applications in fluidized beds. ASME International Mechanical Engineering Congress and Exposition. Boston, MA, USA, ASME Press, Paper IMECE2008-66224**:** 8.

Drake, J. B. and T. J. Heindel (2011). "Local time-average gas holdup comparisons in cold flow fluidized beds with side-air injection." Chemical Engineering Science **To Appear**.

Drake, J. B. and T. J. Heindel (2011). "The repeatability and uniformity of 3D fluidized beds." Powder Technology **213**(1-3): 148-154.

Drake, J. B., A. L. Kenney, T. B. Morgan and T. J. Heindel (2011). Developing tracer particles for X-ray particle tracking velocimetry. ASME-JSME-KSME Joint Fluids Engineering Conference 2011, AJK2011-FED, July 24- July 29, 2011, Hamamatsu, Shizuoka, JAPAN.

Drake, J. B., L. Tang and T. J. Heindel (2009). X-ray particle tracking velocimetry in fluidized beds. 2009 ASME Fluids Engineering Division Summer Conference, FEDSM2009, August 2, 2009 - August 6, 2009, Vail, CO, United states, American Society of Mechanical Engineers.

Du, B., W. Warsito and L.-S. Fan (2005). "ECT studies of gas-solid fluidized beds of different diameters." Industrial and Engineering Chemistry Research **44**(14): 5020-5030.

Dudukovic, M. P., F. Larachi and P. L. Mills (1999). "Multiphase reactors - revisited." Chemical Engineering Science **54**(13-14): 1975-1995.

Ellenberger, J. and R. Krishna (1994). "Unified approach to the scale-up of gas-solid fluidized bed and gas-liquid bubble column reactors." Chemical Engineering Science **49**(24 B): 5391-5411.

Escudero, D. and T. J. Heindel (2011). "Bed height and material density effects on fluidized bed hydrodynamics." Chemical Engineering Science **66**(Compendex): 3648-3655.

Euzen, J. P., P. Trambouze and J. P. Wauquier (1993). Scale-Up Methodology for Chemical Processes. Houston, TX, Gulf Pub. Co.

Felipe, C. A. S. and S. C. S. Rocha (2007). "Prediction of minimum fluidization velocity of gas-solid fluidized beds by pressure fluctuation measurements - Analysis of the standard deviation methodology." Powder Technology **174**(3): 104-113.

Felipe, C. A. S. and S. C. S. Rocha (2007). "Prediction of minimum fluidization velocity of gas-solid fluidized beds by pressure fluctuation measurements - Analysis of the standard deviation methodology." Powder Technology **174**(Compendex): 104-113.

Ford, J. J., T. J. Heindel, T. C. Jensen and J. B. Drake (2008). "X-ray computed tomography of a gas-sparged stirred-tank reactor." Chemical Engineering Science **63**(8): 2075-2085.

Franka, N. P. (2008). Visualizing fluidized beds with X-rays. Mechanical Engineering. Ames, IA, Iowa State University. **Master of Science:** 272.

Franka, N. P. (2008). Visualizing fluidized beds with X-rays. Department of Mechanical Engineering. Ames, IA, Iowa State University. **Masters of Sicence:** 272.

Franka, N. P., J. B. Drake and T. J. Heindel (2008). Minimum Fluidization Velocity and Gas Holdup in Fluidized Beds with Side Port Air Injection. ASME Fluids Engineering Division Summer Meeting. Jacksonville, Fl, USA, ASME Press, Paper FEDSM2008-55100**:** 11.

Franka, N. P. and T. J. Heindel (2009). "Local time-averaged gas holdup in a fluidized bed with side air injection using X-ray computed tomography." Powder Technology **193**(1): 69-78.

Franka, N. P., T. J. Heindel and F. Battaglia (2007). Visualizing Cold-Flow Fluidized Beds with X-Rays. ASME International Mechanical Engineering Congress and Exposition. Seattle, Washington, ASME Press, Paper IMECE2007-43073**:** 7.

Gao, J., X. Lan, Y. Fan, J. Chang, G. Wang, C. Lu and C. Xu (2009). "Hydrodynamics of gas-solid fluidized bed of disparately sized binary particles." Chemical Engineering Science **64**(20): 4302-4316.

Gartside, R. J. (1989). A new reaction system. Fluidization VI. J. R. Grace, L. W. Shemilt and M. A. Bergougnou. New York, NY, Engineering Foundation.

Gauthier, D., S. Zerguerras and G. Flamant (1999). "Influence of the particle size distribution of powders on the velocities of minimum and complete fluidization." Chemical Engineering Journal **74**(3): 181-196.

Geldart, D. (1973). "Types of gas fluidization." Powder Technology **7**(5): 285-292.

Geldart, D. and J. R. Kelsey (1972). "The use of capacitance probes in gas fluidised beds." Powder Technology **6**(1): 45-50.

Geldart, D. and H. Y. Xie (1992). The use of pressure probes in fluidized beds of Group A powder. Fluidization VII : proceedings of the Seventh Engineering Foundation Conference on Fluidization, New York, NY, U.S.A., Engineering Foundation.

Godbole, S. P., A. Schumpe and Y. T. Shah (1983). "Hydrodynamics and mass transfer in bubble columns: effect of solids." Chemical Engineering Communications **24**(4-6): 235-258.

Grace, J. R. (2006). Hydrodynamics of fluidized beds. Multiphase Flow Handbook. C. T. Crowe. Boca Raton, FL, CRC Press**:** 5.1-5.29.

Grassler, T. and K. E. Wirth (2000). "X-ray computer tomography - potential and limitation for the measurement of local solids distribution in circulating fluidized beds." Chemical Engineering Journal **77**(1): 65-72.

Groen, J. S., R. F. Mudde and H. E. A. Van Den Akker (1995). "Time dependent behaviour of the flow in a bubble column." Chemical Engineering Research and Design **73**(A6): 615-621.

Grohse, E. W. (1955). "Analysis of gas-fluidized solid systems by X-ray absorption." Chemical Engineering Progress **1**(3): 358-365.

Guezennec, Y. G., R. S. Brodkey, N. Trigui and J. C. Kent (1994). "Algorithms for fully automated three-dimensional particle tracking velocimetry." Experiments in Fluids **17**(4): 209-219.

Hammer, E. A., G. A. Johansen, T. Dyakowski, E. P. L. Roberts, J. C. Cullivan, R. A. Williams, Y. A. Hassan and C. S. Claiborn (2006). Advanced experimental techniques. Multiphase Flow Handbook. C. T. Crowe. Boca Raton, FL, CRC Press**:** 14.11-14.125.

Heindel, T. J. (2011). "A review of X-ray flow visualization with applications to multiphase flows." Journal of Fluids Engineering, Transactions of the ASME **133**(Compendex).

Heindel, T. J., J. N. Gray and T. C. Jensen (2008). "An X-ray system for visualizing fluid flows." Flow Measurement and Instrumentation **19**(2): 67-78.

Hilal, N., M. T. Ghannam and M. Z. Anabtawi (2001). "Effect of bed diameter, distributor and inserts on minimum fluidization velocity." Chemical Engineering and Technology **24**(2): 161-165.

Hills, J. H. (1976). "Operation of a bubble column at high throughputs - 1. Gas holdup measurements." Chemical Engineering Journal and the Biochemical Engineering Journal **12**(2): 89-99.

Hubers, J. L. (2005). An X-ray visualization facility for large-scale multiphase flows. Mechanical Engineering. Ames, IA, Iowa State University. **Master of Science:** 113.

Hulme, I. and A. Kantzas (2004). "Determination of bubble diameter and axial velocity for a polyethylene fluidized bed using X-ray fluoroscopy." Powder Technology **147**(1-3): 20-33.

Im, K.-S., K. Fezzaa, Y. J. Wang, X. Liu, J. Wang and M. C. Lai (2007). "Particle tracking velocimetry using fast x-ray phase-contrast imaging." Applied Physics Letters **90**(9): 091919.

Inga, J. R. and B. I. Morsi (1999). "Effect of operating variables on the gas holdup in a large-scale slurry bubble column reactor operating with an organic liquid mixture." Industrial and Engineering Chemistry Research **38**(3): 928-937.

Jackson, R. (1963). "The mechanucs of fluidized beds, Part 2." Transactions of The Institution of Chemical Engineers(41): 22-48.

Jahnig, C. E., D. L. Campbell and H. A. Martin (1980). History of fluidized solids development at EXXON. Fluidization. G. J.R. and M. J.M. New York, Plenum Press**:** 3–24.

Kak, A. C. and M. Slaney (1988). Principles of Computerized Tomographic Imaging. New York, IEEE Press.

Kantzas, A., I. Wright, A. Bhargava, F. Li and K. Hamilton (2001). "Measurement of hydrodynamic data of gas-phase polymerization reactors using non-intrusive methods." Catalysis Today **64**(3-4): 189-203.

Kaza, S. R. V. N. (2008). "Effect of the shape of the baffles on the hydrodynamics of a fluidized bed." International Journal of Chemical Reactor Engineering **6**.

Kertzscher, U., A. Seeger, K. Affeld, L. Goubergrits and E. Wellnhofer (2004). "X-ray based particle tracking velocimetry - A measurement technique for multi-phase flows and flows without optical access." Flow Measurement and Instrumentation **15**(4): 199-206.

Kini, V. (1994). Tomographic inspection system using X-rays. Department of Electrical Engineering. Ames, IA, Iowa State University. **Masters of Science**.

Knowlton, T. M., S. B. R. Karri and A. Issangya (2005). "Scale-up of fluidized-bed hydrodynamics." Powder Technology **150**(Compendex): 72-77.

Krambeck, F. J., A. A. Avidan, C. K. Lee and M. N. Lo (1987). "Predicting fluid-bed reactor efficiency using adsorbing gas tracers." AIChE Journal **33**(10): 1727-1734.

Krishna, R., J. M. Van Baten and J. Ellenberger (1998). "Scale effects in fluidized multiphase reactors." Powder Technology **100**(2-3): 137-146.

Kumar, S. B., M. P. Dudukovic and B. A. Toseland (1996). Measurement techniques for local and global fluid dynamic quantities in two and three phase systems. Non-invasive monitoring of multiphase flows. J. Chaouki, F. Larachi and M. P. Dudukovic. Amsterdam, Netherlands, Elsevier Science B.V.**:** 1-45.

Kunii, D. and O. Levenspiel (1991). Fluidization Engineering. Boston, Butterworth-Heinemann.

Lanneau, K. P. (1960). "Gas-solids contacting in fluidized beds." Chemical engineering research & design **38**(a): 125.

Lee, D. J. and S. S. Cha (2003). Three-dimensional measurement of fluid flow by stereoscopic tracking velocimetry. Optical Technology and Image Processing for Fluids and Solids Diagnostics Proceedings. Beijing, China, The International Society for Optical Engineering. **5058:** 73-85.

Lee, D. J., S. S. Cha and N. Ramachandran (2004). Three-dimensional high-resolution optical/X-ray stereoscopic tracking velocimetry. ASME International Mechanical Engineering Congress and Exposition. Anaheim, CA, ASME**:** 53-62.

Lee, S. J. and S. Kim (2005). "Simultaneous measurement of size and velocity of microbubbles moving in an opaque tube using an X-ray particle tracking velocimetry technique." Experiments in Fluids **39**(3): 490-495.

Lim, C. N., M. A. Gilbertson and A. J. L. Harrison (2007). "Bubble distribution and behaviour in bubbling fluidised beds." Chemical Engineering Science **62**: 56-69.

Lim, K. S., J. X. Zhu and J. R. Grace (1995). "Hydrodynamics of gas-solid fluidization." International Journal of Multiphase Flow **21**(Supplement 1): 141-193.

Loth, E., G. Tryggvason, Y. Tsuji, S. E. Elghobashi, C. T. Crowe, A. Berlemont, M. Reeks, O. Simonin, T. Frank, Y. Onishi and B. van Wachem (2006). Modeling. Multiphase Flow Handbook. Boca Raton, FL, CRC Press**:** 13.11-13.150.

Matsuda, S. (2008). "Measurement of solid circulation rate in a circulating fluidized bed." Powder Technology **187**(2): 200-204.

Merchuk, J. C. and Y. Stein (1981). "Local hold-up and liquid velocity in air-lift reactors." AIChE Journal **27**(3): 377-388.

Michiyoshi, I. and A. Serizawa (1986). "Turbulence in two-phase bubbly flow." Nuclear Engineering and Design **95**: 253-267.

Min, J., J. B. Drake, T. J. Heindel and R. O. Fox (2010). "Experimental validation of CFD simulations of a lab-scale fluidized-bed reactor with and without side-gas injection." AIChE Journal **56**(Compendex): 1434-1446.

Moll, T., P. Douek, G. Finet, F. Turjman, C. Picard, D. Revel and M. Amiel (1998). "Clinical assessment of a new stereoscopic digital angiography system." Cardiovascular and Interventional Radiology **21**(1): 11-16.

Mori, S., K. Fujimi and C. Kuroda (1968). "Simple stereographic method in gastrointestinal X-ray examination." Journal of Gastroenterology **3**(4): 321-321.

Nakoryakov, V. E., O. N. Kashinisky and B. K. Kozmenko (1984). Electrochemical methos for measuring turbulent characteristics of gas-liquid flows. Measuring techniques in gas-liquid two-phase flows. J. M. Delhaye and G. Cognet. Berlin ; New York, Springer-Verlag.

Oka, S. and E. J. Anthony (2004). Fluidized Bed Combustion. New York, M. Dekker.

Oka, S. N. (2004). Fluidized Bed Combustion. Monticello, NY, Marcel Dekker, Inc.

Okhi, K. and T. Shirai (1976). Particle velocity in a fluidized bed. Fluidization Technology. D. L. Keairins. Washington, Hemisphere Pub. Corp.**:** 95-119.

Ozkaynak, T. F. and J. C. Chen (1978). "Average residence times of emulsion and void phases at the surface of heat transfer tubes in fluidized beds." AIChE Symposium Series **74**(174): 334-343.

Panneerselvam, R., S. Savithri and G. D. Surender (2009). "CFD simulation of hydrodynamics of gas-liquid-solid fluidised bed reactor." Chemical Engineering Science **64**(Compendex): 1119-1135.

Pannek, U. and L. Mleczko (1997). "Effect of scale-up on the performance of a fluidized-bed reactor for the oxidative coupling of methane." Chemical Engineering Science **52**(14): 2429-2434.

Park, W. H., W. K. Kang, C. E. Capes and G. L. Osberg (1969). "The properties of bubbles in fluidized beds of conducting particles as measured by an electroresistivity probe." Chemical Engineering Science **24**: 851-870.

Patel, A. K., S. S. Waje, B. N. Thorat and A. S. Mujumdar (2008). "Tomographic diagnosis of gas maldistribution in gas-solid fluidized beds." Powder Technology **185**(3): 239-250.

Ramakrishna, K., K. Muralidhar and P. Munshi (2006). "Beam-hardening in simulated X-ray tomography." NDT and E International **39**(6): 449-457.

Reh, L. (1971). "Fluidized bed processing." Chemical Engineering Progress **67**(2): 58-63.

Reh, L. (1986). Circulating Fluid Bed Reactor - A Key to Efficient Gas/Solid Processing. Circulating Fluidized Bed Technology, Proceedings of the First International Conference., Halifax, NS, Can, Pergamon Press.

Resch, F. J. and H. J. Leutheusser (1972). "Reynolds stress measurements in hydraulic jumps." Journal of Hydraulic Research **10**(4): 409-430.

Richtberg, M., R. Richter and K. E. Wirth (2005). "Characterization of the flow patterns in a pressurized circulating fluidized bed." Powder Technology **155**(2): 145-152.

Romero, J. B. and D. W. Smith (1965). "Flash x-ray analysis of fluidized beds." AIChE Journal **11**(4): 595-600.

Romero, J. B. and D. W. Smith (1965). "Flash X-ray analysis of fluidized beds." A.I.Ch.E. Journal **11**(4): 595-600.

Rowe, P. N., L. Santoro and J. G. Yates (1978). "Division of gas between bubble and interstitial phases in fluidised beds of fine powders." Chemical Engineering Science **33**(1): 133-140.

Sahoo, A. and G. K. Roy (2005). "Mixing characteristic of homogeneous binary mixture of regular particles in a gas-solid fluidized bed." Powder Technology **159**(3): 150-154.

Schouten, J. C., M. L. M. Vander Stappen and C. M. Van Den Bleek (1996). "Scale-up of chaotic fluidized bed hydrodynamics." Chemical Engineering Science **51**(10 pt A): 1991-2000.

Schweitzer, J. M., J. Bayle and T. Gauthier (2001). "Local gas hold-up measurements in fluidized bed and slurry bubble column." Chemical Engineering Science **56**(Compendex): 1103-1110.

Seeger, A., K. Affeld, L. Goubergrits, U. Kertzscher and E. Wellnhofer (2001). "X-ray-based assessment of the three-dimensional velocity of the liquid phase in a bubble column." Experiments in Fluids **31**(2): 193-201.

Seeger, A., U. Kertzscher, K. Affeld and E. Wellnhofer (2003). "Measurement of the local velocity of the solid phase and the local solid hold-up in a three-phase flow by X-ray based particle tracking velocimetry (XPTV)." Chemical Engineering Science **58**(9): 1721-1729.

Sherlock, R. A. and W. M. Aitken (1980). "A method of precision position determination using x-ray stereography." Physics in Medicine and Biology **25**(2): 349-355.

Singh, R. K. and G. K. Roy (2005). "Prediction of minimum bubbling velocity, fluidization index and range of particulate fluidization for gas-solid fluidization in cylindrical and non-cylindrical beds." Powder Technology **159**(3): 168-172.

Soria-Verdugo, A., L. M. Garcia-Gutierrez, S. Sanchez-Delgado and U. Ruiz-Rivas (2011). "Circulation of an object immersed in a bubbling fluidized bed." Chemical Engineering Science **66**(1): 78-87.

Squires, A. M., M. Kwauk and A. A. Avidan (1985). "Fluid Beds: At Last, Challenging Two Entrenched Practices." Science **230**(4732): 1329-1337.

Sriram, K. and R. Mann (1977). "Dynamic gas disengagement: a new technique for assessing the behaviour of bubble columns." Chemical Engineering Science **32**(6): 571-580.

Steinemann, J. and R. Buchholz (1984). "Application of an electrical conductivity microprobe for the characterization of bubble behavior in gas-liquid bubble flow." Particle Characterization **1**(3): 102-107.

Stewart, P. S. B. (1968). Transactions of the Institution of Chemical Engineers **46**: T60.

Steynberg, A. and M. Dry (2004). Fischer-Tropsch Technology. Amsterdam ; Boston, Elsevier.

Striegel, A. C. (2005). Development of data acquisition software for X-ray radiography, computed tomography, and stereography of multiphase flow. Mechanical Engineering. Ames, Iowa, Iowa State University. **Master of Science:** 82.

Striegel, A. C. (2005). Development of data acquisition software for X-ray radiography, computed tomography, and stereography of multiphase flow. Department of Mechanical Engineering. Ames, IA, Iowa State University. **Masters of Science:** 111.

Tang, C. and T. J. Heindel (2006). "Estimating gas holdup via pressure difference measurements in a cocurrent bubble column." International Journal of Multiphase Flow **32**(7): 850-863.

Toomey, R. D. and H. F. Johnstone (1952). "Gaseous fluidization of solid particles." Chemical Engineering Progess(48): 220-236.

Toye, D., P. Marchot, M. Crine, A. M. Pelsser and G. L'Homme (1998). "Local measurements of void fraction and liquid holdup in packed columns using X-ray computed tomography." Chemical Engineering and Processing **37**(6): 511-520.

Wang, F., Z. Yu, Q. Marashdeh and L.-S. Fan (2010). "Horizontal gas and gas/solid jet penetration in a gas-solid fluidized bed." Chemical Engineering Science **65**(Compendex): 3394-3408.

Whitehead, A. B. and A. D. Young (1967). Fluidization Performace in Large Scale Equipment. Proceedings of the International Symposium on Fluidization, Netherlands, Amsterdam, Netherlands University Press, Amsterdam.

Winkler, F. (1922). **German Patent 437,970**.

Wu, B., G. Yu, C. Bellehumeur and A. Kantzas (2007). "Dynamic flow behavior measurements in gas-solid fluidized beds using different non-intrusive techniques and polyethylene powder." Flow Measurement and Instrumentation **18**(5-6): 197-203.

Wu, C. Z., H. Huang, S. P. Zheng and X. L. Yin (2002). "An economic analysis of biomass gasification and power generation in China." Bioresource Technology **83**(1): 65-70.

Yasui, G. and L. N. Johanson (1958). "Characteristics of gas pockets in fluidized beds." AIChE Journal **4**(4): 445-452.

Yates, J. G. and D. J. Cheesman (1992). Voidage variations in the regions surrounding a rising bubble in a fluidized bed. Annual Meeting of the American Institute of Chemical Engineers, November 17, 1991 - November 22, 1991, Los Angeles, CA, USA, Published by AIChE.

Yates, J. G. and S. J. R. Simons (1994). "Experimental methods in fluidization research." International Journal of Multiphase Flow **20**: 297-330.

Zhao, Y.-Z. and J.-Y. Zheng (2007). "Micro-scale simulation and analysis of gas-solid fluidized bed with wide size distribution of particles." Zhongguo Dianji Gongcheng Xuebao/Proceedings of the Chinese Society of Electrical Engineering **27**(Compendex): 55-61.

Zhou, Z. A. and N. O. Egiebor (1993). "Prediction of axial gas holdup profiles in flotation columns." Minerals Engineering **6**(3): 307-312.

Zhu, J. and Y. Cheng (2006). Fluidized-Bed Reactors and Applications. Multiphase Flow Handbook. C. T. Crowe. Boca Raton, FL, CRC Press**:** 5.55-55.83.

Zun, I. and F. Saje (1982). Statistical Characteristics of Bubble Flow. Proceedings of the 3rd Austrian - Italian - Yugoslav Chemical Engineering Conference. 276th Event of the European Federation of Chemical Engineering., Graz, Austria.